THE HONG KONG
POLYTECHNIC UNIVERSITY
香港理工大學
Pao Yue-kong Library
包玉剛圖書館

Copyright Undertaking

This thesis is protected by copyright, with all rights reserved.

By reading and using the thesis, the reader understands and agrees to the following terms:

1. The reader will abide by the rules and legal ordinances governing copyright regarding the use of the thesis.
2. The reader will use the thesis for the purpose of research or private study only and not for distribution or further reproduction or any other purpose.
3. The reader agrees to indemnify and hold the University harmless from and against any loss, damage, cost, liability or expenses arising from copyright infringement or unauthorized usage.

IMPORTANT

If you have reasons to believe that any materials in this thesis are deemed not suitable to be distributed in this form, or a copyright owner having difficulty with the material being included in our database, please contact lbsys@polyu.edu.hk providing details. The Library will look into your claim and consider taking remedial action upon receipt of the written requests.

Pao Yue-kong Library, The Hong Kong Polytechnic University, Hung Hom, Kowloon, Hong Kong

http://www.lib.polyu.edu.hk

UPCONVERSION LASING FROM METAL HALIDE PEROVSKITES WITH DIFFERENT DIMENSIONALITIES

GAO WEI

PhD

The Hong Kong Polytechnic University

2022

The Hong Kong Polytechnic University

Department of Applied Physics

Upconversion Lasing from Metal Halide Perovskites with Different Dimensionalities

GAO Wei

A thesis submitted in partial fulfillment of the requirements for the degree of Doctor of Philosophy

June 2022

CERTIFICATE OF ORIGINALITY

I hereby declare that this thesis is my own work and that, to the best of my knowledge and belief, it reproduces no material previously published or written, nor material that has been accepted for the award of any other degree or diploma, except where due acknowledgement has been made in the text.

_____ **(Signed)**

GAO Wei **(Name of student)**

Abstract

Metal halide perovskites (MHPs) as a large family of crystalline direct semiconductors possess excellent optoelectronic properties, such as tunable energy bandgap, high carrier mobility, low trap state density, high absorption coefficient, and low-cost fabrication. Since they were applicated in solar cells in 2009, they have attracted intensive attention due to their diverse optoelectrical properties with a variety of structures. They were first used as laser gain medium with a facile fabrication process in 1998, suggesting that they are potential candidates for developing flexible and low-cost laser to replace the traditional III-V semiconductors. In past years, they have been well studied in the field of solar cells, light-emitting diodes, photodetectors and lasers, and they are considered as a new generation of outstanding materials for optoelectronics.

The optical gain medium is one of the most important parts of a laser system, which is used for amplifying the stimulated emission to generate a strong coherent light. However, the traditional gain medium of a laser diode is limited by its rigid architecture and complicated fabrication process with high cost. To address this problem, an organic dye is appearing as new laser gain media with flexibility. But the liquid gain media is not able to integrate them with other external cavities. Compared with organic dye and traditional III-V semiconductors, MHPs with low-cost fabrication methods have

balanced charge carrier mobility, tunable emission wavelengths coving the whole visible region, higher carrier recombination rate, and so forth.

Herein, MHPs with different dimensionalities as laser gain media were systematically investigated. The solution-processed fabrication of MHPs distinguishes them from traditional III-V semiconductors, which enable MHPs to be easily coated or grow on a flexible substrate to realize flexible lasers. Our study started by using zero-dimensional MHPs quantum dots (QDs) to explore the performance of flexible MHPs lasers. The QDs with an average size of 8 nm were synthesized by using the modified methods published previously in 2015, and their photoluminescence quantum yield is as high as 97%. Then they were coated on flexible Ni foam by spin-coating as a thin film with a thickness of 200 nm. In the previous studies, flexible substrates were organic polymers or plastics. The advantage of using flexible metallic structures as the substrate of flexible lasers over plastic materials is their strong mechanical strength and high thermal conductivity. Another advantage is Ni foam has mesh structures, which can provide random feedback among these voids. Under 800 nm excitation at room temperature, we observed incoherent random lasing emission at ~537 nm. This incoherent random lasing can be tuned to amplified spontaneous emission by changing the voids size of the Ni porous foam. Their corresponding lasing threshold can also be controlled by the external deformation of Ni foam. More importantly, this flexible laser is stable enough that the laser is robust to intensive bending (>1000 bending cycles)

with minimum effect on the lasing intensity. Due to the stability and low spatial coherent characteristics of the flexible random lasers, it is shown to be an ideal light source to produce high-quality micro images. Hence, these results indicate that MHP QDs are a potential laser gain media to develop high-performance flexible lasers

Compared to QDs, the two-dimensional Ruddlesden–Popper perovskites (RPPs) have higher stability, higher binding energy, and stronger exciton confinement due to the quantum well (QW)-like structures. Lasing emission has been demonstrated from RPP films which can be fabricated by the spin-coating technique or solution-crystallization method. These quasi-2D perovskites compose of mixed dimensionalities containing various *n* values, and they are difficult to control the uniformity of *n* values, leading to the shift in absorption and emission energy. Lasing emissions from homologous RPP bulk or the mechanically exfoliated flakes are rarely reported because the single crystal of RPPs with pure phase is hard to obtain. We used the modified method to grow the RPPs with high quality of single *n* value. These were confirmed by the XRD, absorption spectra, and PL emission spectra. The PL spectra excited by 800 nm pulse laser showed their nonlinear property of two-photon absorption. Then their nonlinear properties were further studied by using the micro Z-scan technique. A giant two-photon absorption (TPA) coefficient was calculated by fitting the experimental data. Their TPA coefficient is as high as 3.6×10^3 cm GW^{-1}, which is at least 3 orders of magnitude higher than their 3D perovskites counterparts.

Then the upconversion lasing from RPPs with FP cavities by two-photon excitation was achieved at low temperature. Calculation results and microscopic transient absorption measurements reveal the reasons for lasing from the RPP flakes, which are 1) high-efficiency upconversion transitions under TPA, 2) high differential gain to overcome the biexciton Auger recombination losses inside the laser microcavities, and 3) small electron-phonon coupling strength reduces non-radiative recombination.

Although the MHPs nanoparticles have been widely used as laser gain medium, the unstable crystal structures in moisture environment limited their further applications, especially for the red emission lasers. The red emission can only be achieved from the metal iodide perovskites, which are unstable even at room temperature due to the lattice structure decomposing or transferred from cubic to orthorhombic phases. There are some methods to solve this issue, 1) doping Br^- to improve the stability of the lattice structure, 2) protecting nanocrystals by external matrix. Herein, we use the glass matrix to separate MHPs from the moisture environment and oxygen, which is expected to improve their stability. Then the stability of MHPs nanocrystals with different ratios of I^- and Br^- were investigated to confirm the optimized ratio (1:1). Before using them as laser gain media, their optical gain was investigated by variable-stripe-length measurements. Then the red emission lasing is realized from our samples at low temperature, and their stability in water is significantly enhanced. These findings distinguish RPPs as promising gain media for developing efficient upconversion lasers.

List of Publications

1. **Gao Wei**, Wei Qi, Wang Ting, Xu Jiangtao, Zhuang Lyuchao, Li Mingjie, Yao Kai, Yu Siu Fung. Two-Photon Lasing from Two-Dimensional Homologous Ruddlesden–Popper Perovskite with Giant Nonlinear Absorption and Natural Microcavities. *ACS Nano*. **2022**;16(8).

2. Shao Yan[#], **Gao Wei**[#], Yan Hejin, Li Runlai, Abdelwahab Ibrahim, Chi Xiao, Rogée Lukas, Zhuang Lyuchao, Fu Wei, Lau Shu Ping, Yu Siu Fung, Cai Yongqing, Loh Kian Ping, Leng Kai. Unlocking surface octahedral tilt in two-dimensional Ruddlesden–Popper perovskites. *Nature Communications*, **2022**;13(1).

3. Wang Ting, Chen Weiqing, Loi Hok-Leung, **Gao Wei**, Xu Xuhui, Zeng Longhui, Cheng Ping Kwong, Ahmed Safayet, Yu Xue, Zhao Feng, Qiu Jianbei, Yan Feng, Yu Siu Fung, Tsang Yuen Hong. Stable Single-Mode Lasing from a Hybrid Perovskite–Polymer Fiber. *Advanced Optical Materials*, **2022**;2200439.

4. **Gao Wei**, Yu Siu Fung. Reality or fantasy—Perovskite semiconductor laser diodes. *EcoMat*, **2021**;3(1).

5. Jin Mengfeifei[#], **Gao Wei**[#], Liang Xiaojuan, Fang Ying, Yu Siufung, Wang Ting, Xiang Weidong. The achievement of red upconversion lasing for highly stable perovskite nanocrystal glasses with the assistance of anion modulation. Nano Research. 2021;14(8):2861-6. *Nano Research*, **2021**;2861.

6. **Gao Wei**, Wang Ting, Xu Jiangtao, Zeng Ping, Zhang Wenfei, Yao Yunduo, Chen Changsheng, Li Mingjie, Yu Siu Fung. Robust and Flexible Random Lasers Using Perovskite Quantum Dots Coated Nickel Foam for Speckle-Free Laser Imaging. *Small*, **2021**;17(39):2103065.

7. Xu Xuhui, Lu Wei, Wang Ting, **Gao Wei**, Yu Xue, Qiu Jianbei, Yu Siu Fung. Deep UV random lasing from $NaGdF_4:Yb^{3+},Tm^{3+}$ upconversion nanocrystals in amorphous borosilicate glass. *Optics Letters*, **2020**;45(11):3095-8.

8. Wang Ting , Liu Bitao , Lin Yue , Yang Qihua , **Gao Wei** , Li MingJie , Qiu Jianbei , Yu Xue , Xu Xuhui , Yu Siu Fung. Ultraviolet C lasing at 263 nm from $Ba_2LaF_7:Yb^{3+},Tm^{3+}$ upconversion nanocrystal microcavities. *Optics Letters*, **2020**;45(21):5986-9.

Acknowledgments

First and foremost, I want to express my extreme gratitude to my supervisor Prof. Yu Siu Fung for his invaluable advice, continuous support, and patience during my Ph.D. study. His immense knowledge and plentiful experience have encouraged me all the time in my academic research and daily life. He used to help me solve problems in the setup of optical measurement and conduct experiments with me in the lab, which facilitate my data collection and analysis. This accelerates my research field broadening from the synthesis of nano materials to the analysis of their optical and physical properties. Therefore, my studying experiences and daily life are fruitful and enjoyable under his supervision.

I would like to thank Dr. Li Mingjie for his suggestions and comments, and he gave me an invaluable tutorial on the lasing and transient absorption measurement in ultrafast photonics. Without his help, I could hardly carry on with my experiments.

I am very grateful to Professor Yao Kai and Dr. Leng kai for their high-quality samples, which make my research more meaningful. I also would like to express my appreciation to my family, colleagues, and friends, including Dr. Wang Ting, Dr. Li Siqi, Dr. Xu Jiangtao, Dr. Zeng Ping, Yao Yunduo, Zhuang Lyuchao, Dr. Wei Qi, who help me in experiments and daily life, and providing me with a happy and enjoyable life.

Table of contents

Abstract I

List of Publications V

Acknowledgments VII

Table of contents VIII

List of Figures XI

List of Tables XV

List of Abbreviations XVI

Chapter 1 Introduction 1

1.1 Background 1

1.2 Objectives 5

1.3 Outline of Thesis 7

Chapter 2 Metal halide perovskites for next−generation optoelectronics 9

2.1 Introduction 9

2.2 Chemical structures of and synthesis strategies of metal halide perovskites. 11

2.2.1 Crystal structures 11

2.2.2 Tunable structure by ions and dimensionality 14

2.2.3 Synthesis strategies of metal halide perovskites 18

2.3 Photophysical properties 20

2.3.1 Energy band 20

2.3.2 Carrier dynamics 23

2.3.3 Carrier diffusion Lengths 26

2.3.4 Photoluminescence quantum yield 27

2.4 Metal halide perovskites applicated in lasers 27

2.4.1 Mechanism of Metal halide perovskites lasers 29

2.4.2 Thin film lasers 30

2.4.3 Nanocrystal lasers 31
2.4.4 Exciton-polariton lasers 32
2.5 Metal halide perovskites laser diodes in future 33
2.5.1 Reduction of lasing threshold 34
2.5.2 Critical problems in realizing MHP laser diodes 36
2.5.3 Proposed solutions in realizing MHP laser diodes 36
2.6 Conclusions 38
Chapter 3 Robust and flexible random lasing from 0D metal halide perovskites 40
3.1 Introduction 40
3.2 Experimental methods and instrument 43
3.2.1 Chemical materials 43
3.2.2 Synthesis methods of 0D $CsPbBr_3$ 43
3.2.3 Instrument for material characterizations 44
3.2.3 PL Measurement via Two-photon Excitation 45
3.3 Characteristics of 0D $CsPbBr_3$ with flexible substrate 45
3.3.1 Characteristics of $CsPbBr_3$ quantum dots 45
3.3.2 Characteristics of 0D $CsPbBr_3$ coated Ni foam 47
3.4 Investigation of lasing performance from zero-dimensional $CsPbBr_3$ 49
3.4.1 Incoherent random lasing 49
3.4.2 Incoherent optical feedback from the mesh structure of the flexible substrate 53
3.4.3 The reliability of flexible 0D $CsPbBr_3$ lasers 57
3.5 0D $CsPbBr_3$ lasers applicated in speckle-free laser imaging 58
3.6 Conclusions 60
Chapter 4 Upconversion lasing from two-dimensional homologous Ruddlesden–Popper perovskite 62
4.1 Introduction 62
4.2 Experimental methods and instrument 65

4.2.1 Fabrication Methods 65
4.2.2 Instrument for material characterization 66
4.2.3 Lasing measurement of the RPP flakes 66
4.2.4 Micro Z-scan technique 67
4.3 Characteristics of 2D perovskites 68
4.4 Nonlinear properties of 2D perovskites 73
4.5 Characteristics of 2D perovskite lasing 79
4.6 Mechanism of 2D perovskite lasing 85
4.7 Conclusions 92
Chapter 5 Red upconversion lasing from stable three-dimensional perovskite embedded glasses with the assistance of anion modulation 94
5.1 Introduction 94
5.2 Experimental methods and instrument 97
5.2.1 Chemical materials 97
5.2.1 Fabrication Methods 97
5.2.3 Instrument for material characterizations 98
5.2.4 Measurement of optical gain 99
5.2.5 Measurement of lasing performance 99
5.3 Characteristics of 3D perovskites 100
5.4 Optical gain 104
5.5 Low temperature lasing 106
5.6 Water stability 111
5.7 Conclusions 113
Chapter 6 Conclusions and Outlook 114
6.1 Conclusions 114
6.2 Outlook 117

List of Figures

Figure 2.1 The crystal structures of perovskites. (a) and (b) Schematic diagram of the unit cell of MHPs. (c) Schematic structures of 2D MHPs with different n values. n presents the number of inorganic layers. 12

Figure 2.2 Tolerance factor in $APbI_3$ perovskites. Cs and MA in A-site are widely used due to their size is comparable to the size of the 3D cage. 15

Figure 2.3 Schematic diagram of rotation and distortion of MHPs structures. (a) Orientational disorder of organic cations in the center of PbI_6 octahedral cage. (b) Geometry of methylammonium illustrating 3-fold and 4-fold jumping rotational modes. 16

Figure 2.4 Crystal structures of 2D MHPs with different orientations. 18

Figure 2.5 Band structure of MHPs. 22

Figure 2.6 Carrier dynamics of MHPs. 25

Figure 2.7 Summary of the development of MHPs lasers without or with variety of cavities. 28

Figure 2.8 Proposed architecture of electrically pumped perovskite semiconductor laser. 38

Figure 3.1 Physical characteristics of $CsPbBr_3$ PQDs. 46

Figure 3.2 (a) Fabrication process of the Ni foam coated with $CsPbBr_3$ PQDs. SEM images of the surface mesh structure of the Ni foam (b) without and (c) with a coating of $CsPbBr_3$ PQDs. 48

Figure 3.3 Optical images of Ni foams with different void diameters.....48

Figure 3.4 Characteristics of PQDs coated on the Ni foam. 49

Figure 3.5 Emission characteristics of NFO-PQDs under 400 nm fs laser excitation at room temperature. 51

Figure 3.6 Random lasing characteristics of as-prepared NFO-PQDs. 52

Figure 3.7 Schematic diagram of the deformation of Ni foam. 54

Figure 3.8 Emission characteristics of NFO-PQDs with vertically compressed Ni foam under 800 nm fs laser excitation at room temperature. 54

Figure 3.9 Emission characteristics of NFO-PQDs with a horizontally compressed Ni foam under 800 nm fs laser excitation at room temperature. 56

Figure 3.10 Experiment to measure the bending effect on the emission characteristics of as-prepared NFO-PQDs.....57

Figure 3.11 Optical imaging of micro-size patterns via a commercial laser and our as-prepared NFO-PQDs at room temperature. 60

Figure 4.1 Optical and SEM images of bulk $(PEA)_2(MA)_{n-1}Pb_nI_{3n+1}$ RPP.....69

Figure 4.2 Structure and optical characterizations of RPPs.....70

Figure 4.3 Optical images of the RPPs with different thicknesses (H).....72

Figure 4.4 Upconversion emission characteristics of single RPP flake on SiO_2/Si substrate under 800 nm fs pulse laser excitation at T = 293 K. 74

Figure 4.5 Single-photon emission characteristics of RPP flakes on SiO_2/Si substrate under 400 nm fs pulse laser excitation at T = 293 K. 75

Figure 4.6 Schematic diagram of the micro Z-scan experimental setup for measuring the nonlinear optical characteristics of a single RPP flake. 76

Figure 4.7 Nonlinear optical properties of the RPP flakes. 77

Figure 4.8 Low-temperature (78 K) lasing characteristics of RPP (n = 2) flakes with different cavity lengths, L. 81

Figure 4.9 Upconversion lasing characteristics of an RPP (n = 3) flake on SiO_2/Si substrate under 800 nm fs pulse laser excitation at T = 78 K. 84

Figure 4.10 TA spectra of the RPP flakes. 86

Figure 4.11 Multiple-color lasing characteristics of RPP flakes at various temperatures under 800 nm fs laser excitation. 89

Figure 4.12 Temperature-dependent PL spectra of RPP flakes. 92

Figure 5.1 Characteristics of perovskite glasses. 101

Figure 5.2 TEM images of perovskite glasses. 103

Figure 5.3 The high-resolution XPS spectra. 103

Figure 5.4 Full XPS scan spectra of BIA, BIB and BIC. 104

Figure 5.5 The measurement of the optical gain coefficients. 106

Figure 5.6 Low temperature lasing performance of BIA. 109

Figure 5.7 Random lasing threshold of BIA for different excitation areas (A_{th})..... 109

Figure 5.8 The integrated emission intensity versus temperature. 110

Figure 5.9 Pump intensity dependent PL spectra of BIB (a) and BIC (b). 110

Figure 5.10 Water stability analysis of BIA. 112

Figure 5.11 Relative PL intensities of BIC immersed in water. 112

List of Tables

Table 2.1. Recent progress of optically pumped perovskite semiconductor lasers. 35

Table 4.1. Linear and nonlinear parameters of the RPP flakes with n = 1, 2, and 3. ..79

Table 4.2. Exciton radiative and biexciton Auger recombination rates of RPP flakes with n = 1, 2, and 3. 87

Table 4.3 Parameters used for calculation of I_{th} by Equation (3) for PRR flakes with n = 2 and 3.....87

List of Abbreviations

0D	Zero-dimensional
1D	One-dimensional
2D	Two-dimensional
3D	Three-dimensional
ASE	Amplified spontaneous emission
BA	Butylammonium
CBM	Conduction band minimum
CVD	Chemical vapor deposition
CW	Continuous wave
DBR	Distributed Bragg reflector
DFB	Distributed feedback
EPL	Exciton-polariton laser
EQE	External quantum efficiency
FP	Fabry–Pérot
FWHM	Full width at half maximum
HOMO	Highest occupied molecular orbital
LED	Light-emitting diode
LUMO	Lowest unoccupied molecular orbital
MA	Methylammonium

MHP	Metal halide Perovskite
NIR	Near-infrared
PCE	Power conversion efficiency
PEA	Phenylethylammonium
PL	Photoluminescence
PLQY	Photoluminescence quantum yields
PQD	Perovskite quantum dot
QW	Quantum well
RPP	Ruddlesden–Popper provskite
SHG	Second harmonic generation
TPA	Two-photon absorption
UC	Upconversion
VBM	Valence band maximum
VCSEL	Vertical cavity surface-emitting laser
WGM	Whispering-gallery-mode

Chapter 1 Introduction

1.1 Background

A laser gain medium is one of the key parts of a laser system, which is used for amplifying the stimulated emission to generate a strong coherent light.[1, 2] The most important property of a gain medium is defined as the gain coefficient, which is used to describe how well a laser gain medium amplifies photons by stimulated emission. To date, there have been many commercial laser gain media, including gas (argon), liquid (dye), and solid-state (GaAs). However, most of them can only amplify the emission with a fixed wavelength or a very limited range of wavelength, which limits the development of multiple color lasers. The gain media with solid-state are easier to store, transfer, and integrated with other devices, than that with other states, such as gas and liquid. Most solid-state gain media are made of direct bandgap semiconductors due to the higher electron-photon conversion efficiency compared to the indirect bandgap materials. For example, GaAs, a direct bandgap semiconductor with higher saturated electron velocity and electron mobility, are applied as a gain medium embedded in the $Al_xGa_{1-x}As$ to form the double heterostructure laser. Unfortunately, the fabrication of semiconductor crystals with high quality is complicated with high cost, which hinders their wide application in this field. Therefore, the discovery of a new gain medium with

high absorption coefficients and carrier mobility, tunable amplified wavelength, and facile fabrication is necessary for exploring modern lasers.

Metal halide Perovskites (MHPs) possessing excellent optoelectronic properties have become a new generation of outstanding materials for optoelectronics, such as solar cells, light-emitting diodes (LEDs), photodetectors and lasers. MHPs are a large family of crystalline semiconductors with a general chemical structure of ABX_3 and $L_2A_{n-1}B_nX_{3n+1}$ for three-dimensional (3D) and two-dimensional (2D) structures, respectively. For 2D MHPs, they have a quantum well (QW)-like structures, in which the inorganic perovskites are separated by the organic spacing groups, and n is an integer, representing the number of inorganic well layers.[3] Generally, MHPs have high carrier mobility and low trap state density, which can promote carrier injection and transportation.[4] This is important for the gain materials applied in electronics to realize high electron-photon conversion efficiency devices. In contrast to conventional semiconductors, the crystal growth of MHP can be realized by a low-temperature solution-processed method, which is suitable for large-scale fabrication with low cost.

MHPs as direct-bandgap semiconductors have a higher optical gain coefficient, which is comparable to the commercial optical gain media, such as GaAs.[5] This is a key factor to realize ultra-low threshold lasers. In addition, MHPs also have a wide range of bandgap, which can be tailored by the composition ratio of metal and halide ions, so

that their emission is tunable from the visible to near-infrared region. The regular shape of MHPs due to their intrinsic crystal structures enables them to easily form different feedback cavities for light scattering, and these cavities can be integrated with various microstructures to form micro lasers. Collectively, MHPs with a wide range of tunable bandgap, balanced charge carrier mobility, and facile fabrication, are potential as solid-state laser gain media for application in multi-color lasing.

Indeed, a variety of lasers, including multi-color lasers, random lasers, exciton-polariton lasers, subwavelength lasers *et al*. have been realized from various MHPs, including perovskite quantum dots, nanowires, nanoparticles, films, bulk and flakes from 2D perovskites materials. These laser emissions can be originated from MHP itself or external cavities integrated with MHPs, such as Fabry–Pérot (FP), whispering gallery mode (WGM), distributed feedback (DFB), and distributed Bragg reflector (DBR), which show their potential to be wildly applied in different laser systems. MHPs were used as gain media for lasing as early as 1998, but this did not attract much attention due to the operating temperature being too low (40 K).[6] Since the first MHPs laser was achieved at room temperature in 2014, extensive studies on exploring lasing from MHPs have been conducted.[7] For example, Xiong *et al*. demonstrated a nanolaser from perovskite nanoplatelets with WGM cavity in the same year.[8] Friend and co-workers reported a single-mode lasing from solution-processed mixed MHPs by embedding into a dielectric mirror and a gold mirror.[9] Due to the simple fabrication

process and well-defined intrinsic structures of MHPs, they are favored to be integrated with external cavities to realize low threshold lasers. Recently, the MHPs single-mode laser with DFB was achieved by continuous-wave laser excitation, which is a great step toward an electrically pumped MHPs laser.[10]

MHPs also demonstrate outstanding nonlinear optical properties due to their tunable chemical components and multiple crystal structures, which support them to apply in nonlinear optical applications, such as second harmonic generation (SHG), sum frequency generation and multi-photon excited photoluminescence (PL).[11] The PL emission via multi-photon excitation is a process related to two steps, 1) some photons are simultaneously absorbed by an atom or molecule where no resonant intermediate states exist, resulting in the energy transition from the ground states to excited states, 2) energy release from high level to ground level with one photon emitting. During this process, the emitted photon energy is the sum of exciting photons energy, which realizes the photon upconversion (UC). Among these optically pumped MHP lasing, most of them are pumped via a single photon, and there is a lack of exploring in multi-photon excitation, which can achieve MHPs UC lasers.

1.2 Objectives

Due to the outstanding physical and optical properties of MHPs, they are the potential materials to work as good laser gain media to realize UC lasers. We will systematically explore UC lasers achieved from MHPs with low and high-dimensional structures. Firstly, Perovskite quantum dots (PQDs) with a strong quantum effect which has the same structure as their 3D counterpart, is considered as zero-dimensional MHPs due to their small size of several nanometers. It has superior optoelectronic properties, such as high absorption coefficient and PL quantum yield (PLQY), which is an excellent optical gain material for UC lasers. We will find an efficient method to synthesize the PQDs with high quality, such as size distribution, absorption band edge, and full width at half maximum (FWHM) of the PL peak. Then they were integrated as a laser gain medium with the flexible substrate, to form a flexible lase device. Due to the nonlinear optical properties of the PQDs, they have a high two-photon absorption (TPA) coefficient, which means they can achieve UC PL by two-photon excitation. We will achieve UC flexible laser via the emission light scattering between perovskite nanoparticles, or from the external cavities provided by the flexible substrates. Next, we will evaluate the lasing performance of this flexible UC laser and try to broaden its application in optical imaging.

Secondly, Ruddlesden–Popper perovskites (RPPs) have recently drawn significant interest as two-dimensional MHP due to their stable performance in both

photoabsorbers and emitters. Compared to the quasi-2D RPP films obtained by spin-coating or drop-cast method, homologous RPP single crystals have strong quantum confinement with pure phase (single n value). However, the lasing from homologous RPPs is rarely reported. The main challenge is that it is difficult to grow the pure crystal with a single-phase, especially for $n > 1$. We will develop a facile fabrication process for the growth of crystals with high quality. Then we will analyze their linear and nonlinear optical properties, especially for the measurement of TPA coefficient. We will build a new setup for the Z-scan measurement of micro-size samples, which is different from the conventional Z-scan setup used for large sizes of the sample, and we call our new setup micro Z-scan technique. We hope that their TPA coefficient can be as high as their 3D counterpart, to support UC PL. Furthermore, we also want to realize UC lasing from RPP and find the lasing mechanism in these QW-like structures.

Next, we will investigate the UC lasing performance from MHP nanoparticles, which have a 3D structure. Although their optical properties are as good as their low-dimensional counterparts, their poor stability in moisture environments hinders their further applications in optoelectronic. We will try to improve their stability by embedding them into the polymer or glass matrix, which can prevent MHP from water and oxygen. Then their optical and physical properties will be investigated, to evaluate whether they can be used as the gain medium to achieve stable UC lasers. Finally, we

will compare these three types of MHP and analyze the relationship between their structures and optical properties, to find a guideline for designing the MHP UC lasers.

1.3 Outline of Thesis

In chapter 2, the physical properties of perovskites, from zero- to three-dimensional, will be discussed from the aspect of synthesis method, crystal structures, optical spectra, and applications in optoelectronics, especially in lasing.

In chapter 3, halide PQDs were synthesized, and flexible random lasers using as-synthesized perovskite quantum dots were demonstrated, which can be used in speckle-free imaging.

In chapter 3, the physical and optical properties of two-dimensional RPPs were studied. Upconversion lasing from these 2D materials was realized and the lasing mechanism was also discussed.

In chapter 5, the optical properties of three-dimensional lead halide perovskite nanocrystals embedded in glass were investigated, and random lasing from perovskite glass was achieved due to their high nonlinear optical gain.

In chapter 6, the work done during my Ph.D. study is summarized, and the potential research work is proposed to be carried out in the future

Chapter 2 Metal halide perovskites for next–generation optoelectronics

2.1 Introduction

MHPs have become a new class of direct semiconductors for optoelectronics due to their outstanding electrical and optical properties. MHPs can be considered as derivates of a mineral, calcium titanate, that was discovered by a German mineralogist in Russia in 1839. Although MHPs have been successfully synthesized for about 130 years,[12] they started to receive attention just from the 1990s, when they began to show their prospective optoelectronic properties.[13-16] MHPs as direct bandgap semiconductors demonstrate excellent optoelectrical characteristics, including low trap-state densities, and large carrier mobility compared to that of the III-V traditional semiconductors,[4, 17, 18] resulting in their huge applications in solar cells,[19-21] LEDs and lasers.[10, 22, 23]

Solar cells as clean and renewable energy have attracted intense attention due to the increasing awareness of environmental protection. MHPs were first successfully applied in the solar cell in 2009 by Miyasaka *et al*., which showed their potential for application in the solar cell.[24] The intrinsic properties of MHPs enable them to be promising candidates as photon absorbing layers for solar cells, such as high absorption

coefficient, tunable bandgap, long diffusion length, and balanced mobility of charge carriers.[25, 26] Furthermore, the Although the power conversion efficiency (PCE) is as low as 3.81%, it rises dramatically up to larger than 24% in the past decade, which is comparable to the conventional silicon solar cell (with PCE of 22~25%), and hence they have been considered as the third-generation materials for solar cell.[27, 28] In addition, their facile fabrication process enables them to be a prominent candidate for generating efficient and cost-effective solar cells.

As a new generation of direct bandgap semiconductors, MHPs have been widely studied as excellent gain media used in lasers due to their outstanding optoelectrical properties along with low-cost fabrication processes. MHPs laser was first demonstrated in 1998 at low temperatures by Ito and co-workers.[6] Since the first room-temperature MHPs laser was reported in 2014, tremendous attention are drawn to this field. Optical pumped MHPs laser from various cavities have been reported in the past several years, the optical cavities including FP cavities,[29] DFB gratings, and WGM cavities.[30, 31] The first MHPs lasers with DFB pumped by continuous wave (CW) lasers were demonstrated in 2017, which can only achieve at 100 K.[32] Then Adachi and co-workers realized the room-temperature MHPs CW lasers in 2020, which is a great step toward electrically pumped MHPs lasers.[10] These results indicate that the MHPs as laser gain media are comparable to the conventional direct bandgap

inorganic semiconductors, and they are the potential materials to be the next generation of gain media for applications in MHPs laser diodes.

MHPs are also applied in many other fields, including memories, detectors, transistors, sensors, and batteries. For example, MHPs are considered a potential candidate for X-ray detectors, which have a reasonable absorption coefficient compared to that of conventional materials. Due to the high energy of X-ray emissions, the active layer used as a detector should be as thick as to stop the photon penetration and high attenuation coefficient, which is dependent on the atomic number. MHPs are composed of atoms with high atomic numbers, such as Pb, I, and Br, so they have a higher attenuation coefficient than that of the traditional materials.[33] Collectively, their advances in optical and electrical properties make them the promising next-generation semiconductors for applications in optoelectronics.

2.2 Chemical structures of and synthesis strategies of metal halide perovskites

2.2.1 Crystal structures

MHPs are a large family of crystalline direct semiconductors with a general chemical formula of MHPs is ABX_3, where A represents an organic (i.e., methylammonium, MA^+) or inorganic monovalent cation (i.e., Cs^+), B is a divalent metal cation (i.e., Pb^{2+}, Sn^{2+}),

and X represents halide anion (**Figure 2.1**). According to organic or inorganic cation in the A-site, the MHPs can be classified as organic-inorganic hybrid MHPs and all-inorganic MHPs. Based on the dimensions, they can be categorized into 3D, 2D, one-dimensional (1D), and zero-dimensional (0D). All their crystal structures have a 3D network formed by a corner-sharing $[BX_6]_4$ octahedra, and the center of the cuboctahedral void consisting of eight octahedra is occupied by a monovalent A cation.

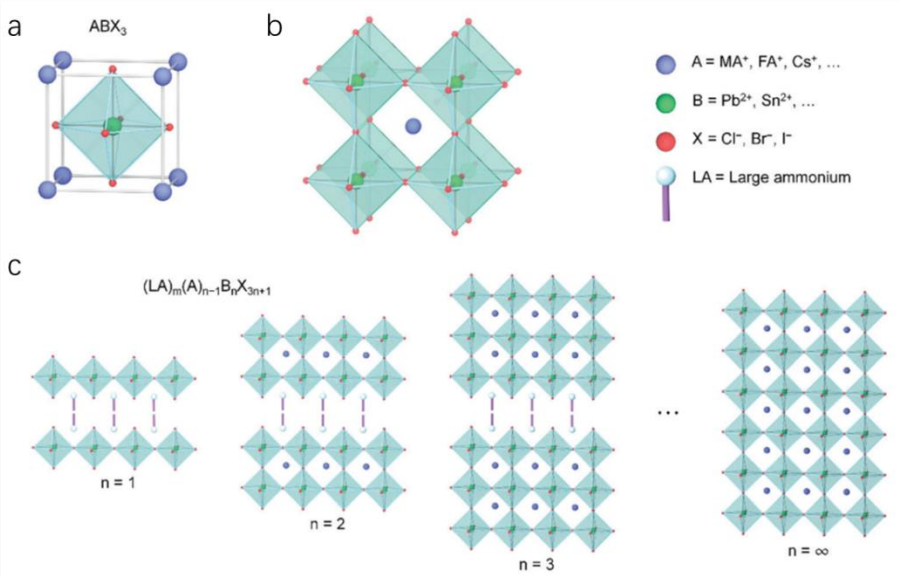

Figure 2.1 The crystal structures of perovskites. (a) and (b) Schematic diagram of the unit cell of MHPs. (c) Schematic structures of 2D MHPs with different n values. n presents the number of inorganic layers.[18]

2D MHPs are well known as RPPs which are formed by 3D structure embedded in organic group spacer, and the organic spacer and 3D perovskites stack with weak van der Waals forces to form a layered structure. 2D RPPs have a general chemical formula

of $L_2A_{n-1}B_nX_{3n+1}$, where L represents a large ammonium cation (i.e., phenyl ethyl ammonium, PEA^+ or butylammonium, BA^+), the other sites are similar to the 3D structure. This 2D layered material composites of layer organic and inorganic groups with different dielectric constants to form multiple QW-like structures with strong spatial confinement of excitons, and the integer *n* represents the number of inorganic perovskites layers in a unit QW structure.

Low-dimensional MHPs are always related to the nanostructures, such as 1D and 0D. 1D MHPs contain nanowires and nanorods.[34, 35] $CsPbBr_3$ and $CsPbI_3$ single-crystalline nanowires have been obtained with uniform growth directions, and the diameter of $MAPbI_3$ nanowires can reach as small as 100 nm and their size distribution is uniform. The smaller size of nanoparticles, such as quantum dots, can be considered 0D MHPs. For example, $CH_3NH_3PbBr_3$ quantum dots with a diameter of 6 nm were prepared by Schmidt in 2014, which have enhanced stability than that of their 3D MHPs counterparts.[36] The properties of 0D MHPs can be tuned by the size of quantum dots. Rogach reported the size-tunable $MAPbBr_3$ PQDs from 1.8 to 3.6 nm, of which the emission peak is changed from 475 to 520 nm.[37]

2.2.2 Tunable structure by ions and dimensionality

The lattice bone of MHPs is composed of three lattice sites referred to as the A-site, B-site and X-site. The perfect symmetry structure of MHPs should be Pm3m space group, where the atoms are tightly packed with each other and the radii of atoms follow the equation of $r_A + r_X = \sqrt{2}(r_B + r_X)$, where r_A, r_B, and r_X are radii of atoms at three positions. To evaluate the stability of MHPs, Goldschmidt introduced two parameters, tolerance factor t and the octahedral factor u.[38] The tolerance factor is used to describe the extent of the distortion by $t = (r_A + r_X) / (r_B + r_X)$, while the octahedral factor is obtained from the ratio of atomic radii, r_B / r_A. The perovskite usually shows a high symmetry cubic or tetragonal crystal structure at toom temperature, while it may change into a low symmetry tetragonal or orthorhombic phase by the distortion of the $[BX_6]_4$ octahedra at low temperature.[39] MHPs with different phases and components will have different t and u, and their ranges are 0.81~1.11 and 0.44~0.9 for t and u, respectively (**Figure 2.2**). For example, the t value for the perovskites with cubic and orthorhombic structures is about 0.9 ~ 1.11 and 0.71 ~ 0.9, respectively. Different ions have different atomic radii, which can affect the t and u. Therefore, the cation and anion substitution will cause the change of crystal structures, making them tunable physical properties.

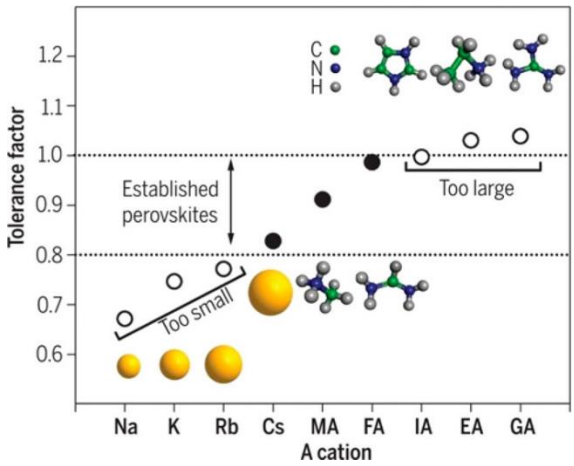

Figure 2.2 Tolerance factor in APbI3 perovskites. Cs and MA in A-site are widely used due to their size is comparable to the size of the 3D cage.[40]

The symmetry of MHPs can be affected by the dynamic motion of organic A-site and X-site and disordered organic A-site cations. The specific alignment of the A-site polar organic cation is induced by hydrogen bonding (i.e., between nitrogen and hydrogen atoms) in the perovskite lattice, resulting in an order–disorder phase transition into a polar structure below 360 K.[41] This electronic ordering is determined by the dipole moments of the A-site and the strength of the hydrogen bonding (**Figure 2.3**).[42] For example, Organic cations (i.e., MA^+) with an electrical dipole of 2.3D contribute to the high dielectric constants in MHPs.[43] The incorporation of MA^+ can form the mixed cation leading to tunable wide-bandgap mixed MHPs, which can heal deep trap defects to generate a group of defect-tolerant materials.[44] In addition, the motions of cantons in A-sit within the inorganic lattice of MHPs can be measured by quasielastic neutron scattering measurements.

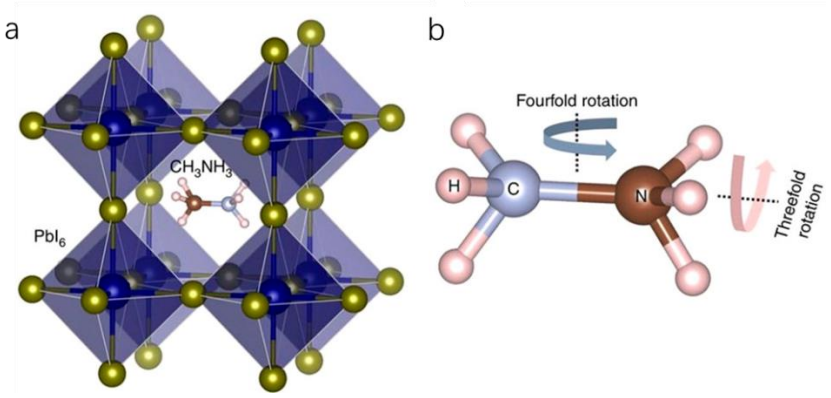

Figure 2.3 Schematic diagram of rotation and distortion of MHPs structures. (a) Orientational disorder of organic cations in the center of PbI_6 octahedral cage. (b) The geometry of methylammonium illustrates 3-fold and 4-fold jumping rotational modes.[42]

In a perfect cubic MHPs, the B-site divalent metals are located at the body-centered position of the cube, and the X anions occupy the six face-centered locations, forming an octahedral surrounding the divalent metal, with the monovalent A cations situated at the cube vertices. The bandgap and the dispersion of the energy level structures are determined by the chemical bonds between the metal and the halogen. Larger electronegativity differences between metal B and X anions cause a more ionic bond character, leading to the electronic cloud closer to the X nuclei.

X ions (i.e., I^- and Br^-) make the main contribution to the energy bandgap of MHPs, which can be tuned by the use of different single or mixed halogens. The absorption spectra of the $MAPbI_{3-x}Br_x$ will red-shift compared to that of $MAPbBr_3$ due to the

bromide concentration decrease, indicating the lower electronegativity of the larger halogen atoms. Therefore, the optical absorption can be readily tuned via halide ratio engineering in MHPs, covering the entire visible region.

The structures of MHPs can also be determined by dimensionality. The 3D structure has a rigid framework due to the corner-shared BX_6 octahedral crystal structure. In contrast to ABX_3, the structural flexibility increases in the low dimensional MHPs, which is affected by the length of the organic spacing group. Due to the 2D MHPs originating from the ABX_3 sliced into multiple layers, the size and the *t* can be easily and widely engineered (**Figure 2.4**). However, in the 0D MHP, their size restrictions are not applicable, because the separated BX_6 octahedra can shift readily in the lattice structure.

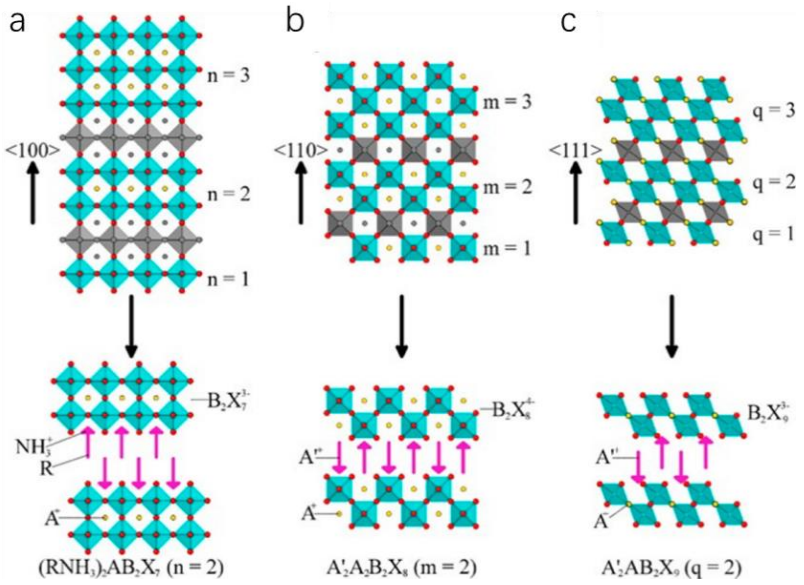

Figure 2.4 Crystal structures of 2D MHPs with different orientations. (a) The ⟨100⟩-oriented layered perovskites $(RNH_3)_2A_{n-1}B_nX_{3n+1}$. (b) The ⟨110⟩-oriented layered perovskites $A'_2A_mB_mX_{3m+2}$. (c) The ⟨111⟩-oriented perovskites $A'_2A_{q-1}B_qX_{3q+3}$.[45]

2.2.3 Synthesis strategies of metal halide perovskites

The facile fabrication process of MHPs is one of the most important reasons why they can attract intensive attention as a new class of direct bandgap semiconductors for applications in optoelectronics. The general chemical reaction can be written as: AX + BX_2 = ABX_3, which can be reacted in a gas or liquid environment. Among so many methods for the synthesis of MHPs, the low-temperature solution-processed method is the most attractive fabrication method due to its great potential in scalable with low cost, and this method has been adopted in all research fields, including solar cells, LEDs, and lasers. For the final products of synthesis, they can be classified as two major types

based on the morphologies of MHPs, films, and single crystals. MHP films can be obtained by spin-coating, chemical vapor deposition, atomic layer deposition, and so forth.[46]

Spin-coating is the most widely used method for the fabrication of MHP films, and the formation of crystalline films needs an antisolvent dripping and thermal annealing process. The dripping process can facilitate nucleation because this process can induce the supersaturation in the precursor solution.[47] The increased nucleation density can help to generate flat and uniform films with high crystal quality, while the thermal annealing process can remove residual solvent, resulting in quick nucleation and crystal growth.

The microcrystals of MHPs can be grown in gas and liquid environments, and the liquid method is still dominant due to the simple synthesis process, and the microcrystals can be self-assembly formed.[48] The driven force is also from the supersaturation of the precursor solution due to the solvent evaporation or introduced antisolvent. The reaction in the gas environment is well known as the chemical vapor deposition (CVD) process without very high temperature, which is different from the traditional CVD because the melting points of MHPs are relatively lower than III–V semiconductors. Although this method can obtain the crystals with better quality than the solution-processed method, organic MHPs decomposition cannot be avoided due to the thermal

effect on the unstable hybrid structures in the direct vapor-phase process. So that the two-step vapor-phase process was used to synthesize MHPs nanowires applicated in lasers by Xiong and co-workers.[49]

Due to the unique properties of MHPs, the halide ions can migrate between the X-site position, which enables the ratio change of halide composition by ion-exchange reactions. For example, the halide anions can be partially or completely substituted by reaction with other halide ions through halide vapor halide anion, and halide ions also showed high mobility in the stable lattice structures.[50] This is also simple for tuning the energy bandgap and emission wavelengths of MHPs. There are other methods used to integrate MHPs crystals with other external cavities for applications in laser, such as nanoimprint, electron beam lithography, and direct laser ablation.[51]

2.3 Photophysical properties

2.3.1 Energy band

The fundamental physical and optical properties of MHPs is the energy bandgap (E_g), which determines mangy optical performance, including absorption energy, carrier recombination rate and lifetime, emission wavelength, and PLQY. Therefore, a better understanding of the electric band structure of MHPs can help to well guide the optoelectronic device design. Due to all types of MHPs containing the part of BX_6, the

electronic characters of octahedrons have a large influence on the properties of MHPs, so the properties of octahedrons should be first studied. For example, the property of PbI_6 is determined by the chemical bond between Pb and I, where the Pb 6s–I 5p σ-antibonding orbital forms the highest occupied molecular orbital (HOMO), while Pb 6p–I 5p π-antibonding and Pb 6p–I 5s σ-antibonding orbitals form the lowest unoccupied molecular orbital (LUMO), shown in Figure 2.5a.[52] The energy band structure of cubic-phase $MAPbI_3$ demonstrated that I 5p and Pb 6s orbits account for 70% and 25% of the valence band maximum (VBM), respectively, while nearly all conduction band minimum (CBM) consists of only Pb 6p orbit (Figure 2.5b).[53] This also suggests that the MHPs are direct bandgap semiconductors, although there is a little shift with the *R* point due to the spin-orbit coupling. It is well known that direct bandgap materials are more suitable for optical applications, such as efficient PL and laser gain medium. For example, the optical gain of $MAPbI_3$ is 3200, which is comparable to the commercial gain material. The high optical gain can lead to the development of the low-threshold laser, and this property will broaden its applications in MHP lasing. Furthermore, the contribution of different chemical groups to each electric band can be determined by the measurement of the density of states shown in Figure 2.5c, where we can observe that the major contribution of the electric band is from the $[PbI_6]^4$ octahedron.[54]

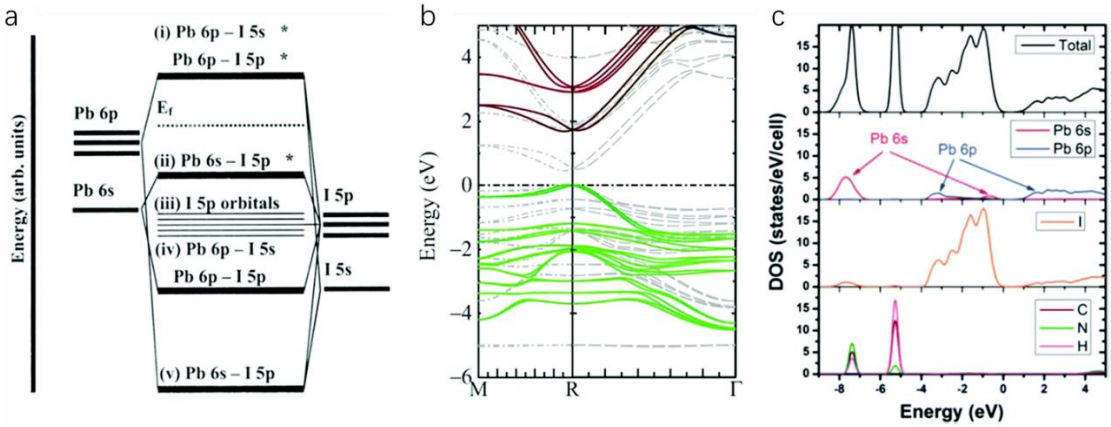

Figure 2.5 Band structure of MHPs. (a) Energy levels of the chemical bonds in $[BX_6]^4$ clusters. (b) Energy band structure of $MAPbI_3$. Orbital contributions are indicated by I 5p (green), Pb 6p (red), and Pb 6s (blue). (c) The density of states (DOS) of tetragonal $MAPbI_3$ was calculated with semilocal density functional theory (DFT).[52-54]

Due to the energy band level of MHPs determined by BX_6, the properties can be easily tuned by the changed composition of the metal-halogen group. For example, if the halogen atom is changed from Cl to I, the VBM will be higher than the original level due to the up shift of the p orbits of halogen, and the CBM is nearly no change. Therefore, the electric bandgap of MHPs with different halogens has a trend of Cl > Br >I, resulting in the emission spectra can be tuned across the entire visible region. For the lead-free MHPs, where the lead is replaced by the Tin, the CBM will shift downward due to the p orbits of the metal decrease. So that the Tin MHPs have a narrower E_g than lead MHPs, leading to the emission wavelength red shift to red-NIR.[55]

In contrast to the major contribution of BX_6 octahedron, the chemical group in the A site has little effect on the energy band level, because their energy level is lower than the VBM. That is why MHPs with different A cations have similar emission wavelengths.[56] However, the size of A cations can affect the crystal lattice structure and the stability of MHPs. For example, as the size of the A cations increases, the lattice structure expands, resulting in the decrease of E_g. 2D MHPs have the same B- and X-sites as their 3D counterpart, and the E_g will increase due to the quantum well-like structures. For example, the bandgap of $CH_3NH_3SnI_3$ (3D) is smaller than $(C_4H_9NH_3)SnI_4$ (2D, n = 1), but unfortunately, the 2D sample is unstable in air.[57] In these quantum well-like structures, the exciton binding energy is higher than their 3D counterparts as the strong electron−hole interactions due to the big difference in dielectric constant between organic spacer (barrier) and inorganic perovskites (well). This structure can also increase the PL intensity and enhance the PLQY, which is favorable to develop low dimensional LEDs.

2.3.2 Carrier dynamics

An understanding of the carrier dynamics in the excited state, such as carrier generation and recombination, scattering, and interaction with each other, is important for explaining most of the optical phenomena on MHPs.[58] Among these physical properties, the exciton binding energy (E_b) is the most distinguished character for MHPs,

of which the energy values range from 2 to 120 meV for 3D structures, and from 80 to 370 meV for 2D structures.[58, 59] **Figure 2.6a** shows the percentage of the free carrier in MHPs with different exciton binding energies versus the total excitation density (n_0). Under the same excitation power, the free carrier density of MPHs with larger E_b is lower. At room temperature, exciton dissociated to free carrier due to the thermal energy is higher than E_b. The PL of MHPs originates from the exciton recombination so that their E_b can be calculated from the temperature-dependent PL intensity. Robin and co-workers reported another approach to determine the E_b by direct measurement in 2015, which can precisely study the multiple excitonic transitions.[60]

At low excitation power, nearly all excited states are free carriers, and the first-order recombination coefficient k_1 is as low as 10 μs^{-1}, which is suitable for application as a solar cell due to the efficient carrier extraction ($n_0 \leq 10^{15}$ cm^3).[61] With the excitation power increase, the free carrier density decrease, while the percentage of exciton increase associated with multiparticle interactions. The rate equation can be written as: $d_n/d_t = G - k_1 n - k_2 n^2 - k_3 n^3 = G - nR_T(n)$, where G is excitation power density, k_1, k_2 and k_3 are exciton recombination coefficient, electron−hole recombination coefficient and Auger recombination coefficient, respectively.

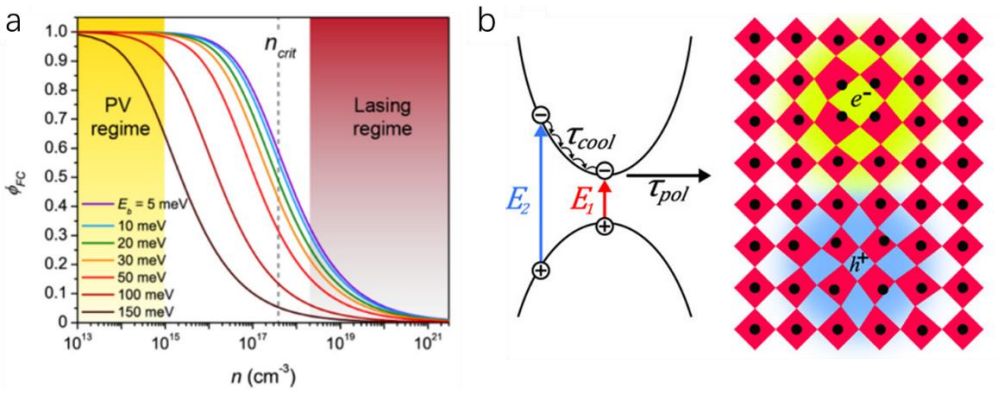

Figure 2.6 Carrier dynamics of MHPs. (a) The percentage of the free carrier at the excited state of MHPs with different exciton binding energies at room temperature. (b) Schematic of polaron formation by the electron-hole interaction in the lattice structure of MHPs.[61, 62]

Polaron is a charge carrier that exists in MHPs, which is a quasiparticle consisting of an electron or hole dressed by its self-induced lattice polarization in polar semiconductors (**Figure 2.6b**).[62] Polarons can be categorized into two types, small and large polarons, which are formed through long-range Coulomb potential and short-range deformation potential, respectively.[63] The large polarons affect the screening of the Coulomb potential, which exists commonly in MHPs. These can suppress the behaviors of charge carrier scattering, trap-assisted nonradiative recombination from the trap state, and Auger recombination in MHPs. This protection of charge carriers from large polarons enables MHPs to achieve high PLQY.

The free carrier and monomolecular recombination coexist in MHPs at room temperature, their density relates to the trap state density determined by the crystalline

quality. The bimolecular recombination process is an intrinsic property of a direct bandgap semiconductor, of which the coefficient ranges from about 0.6×10^{-10} to 14×10^{-10} cm^3 s^{-1} at room temperature.[61, 64, 65] The major limitation for MHPs used as a light source is the optical loss from non-radiative recombination, such as Auger recombination. Although it is suppressed by large polarons, the average Auger recombination coefficient is about $k_3 = (0.2\sim1.6) \times 10^{-28}$ cm^6 s^{-1}, which is far higher than that in a conventional gain medium.[66]

2.3.3 Carrier diffusion Lengths

The carriers with long-distance transportation are essential for application in solar cells. The electron-hole diffusion length (L_D) can be calculated from the equation: $L_D = (k_B T \mu \tau_r / e)^{1/2}$, where k_B,T, e, μ and τ_r represent the Boltzmann constant, absolute temperature, elementary charge, carrier mobility, and lifetime, respectively. In general, the L_D of $MAPbI_3$ is about 100 nm, and in the mixed MHPs $CH_3NH_3PbI_{3-x}Cl_x$, it can increase to 1 μm.[67] The L_D is generally influenced by defect or trap state density in MHPs, which substantially exist in the grain boundaries or surfaces of MHPs polycrystalline films. L_D of $MAPbI_3$ single crystal is longer than that of polycrystalline films. For example, in 2015 Huang demonstrated that under low light illumination, the electron and hole diffusion lengths of $MAPbI_3$ single crystals are larger than 3 mm, and under full sunlight illumination, they can reach as long as 175 μm.[68]

2.3.4 Photoluminescence quantum yield

Photoluminescence Quantum Yield (PLQY) is an important factor to evaluate the optical materials, which can be expressed as:

$$\varepsilon = \frac{\text{number of photons emitted}}{\text{number of photons absorbed}}$$

The power-dependent PLQY from MHP thin film was reported by Deschler and co-workers in 2014, in which the PLQY increase to as high as 70% with the increase in excitation power to 100 mW cm^{-2}.[69] Many strategies have been used to enhance the PLQY, such as applying the materials with higher E_g and strong oscillator strengths. Reducing the gain size of MHP thin films can enhance the charge confinement, leading to the radiative rate increase, which can also help to increase the PLQY up to 36%.[70] However, it is as low as only 1% in the 2D MHPs at room temperature due to the thermal quenching of excitons.[71] To address this issue, Mixed-phase low-dimensional perovskites were introduced, which showed much higher PLQY and can be applied in LED at room temperature.[72] The low PLQY can also be caused by the surface trap so many studies using passivated halide-ion pair ligands can enhance the PLQY. [73]

2.4 Metal halide perovskites applicated in lasers

MHPs with combined the advantages of inorganic and organic semiconductors are considered excellent candidates for laser gain medium, and MHPs lasers have shown

many desirable characteristics, such as low-cost, low threshold, strong coherence, and tunable wavelengths. Due to solution-processed fabrication, they are easily integrated with external cavities to form micro-cavity lasers, such as vertical-cavity surface-emitting lasers (VCSELs) and DFB lasers, and so forth (Figure 2.7).[69, 74, 75] Moreover, the threshold of optically pumped MHPs laser can be as low as about 0.1 μJ cm^{-2}, and the emission wavelength can cover the entire visible region, from ultraviolet to NIR. Yufei and co-workers reported the MHPs laser excited by CW laser at 160 K in 2017, which makes a big step toward MHPs laser diode and verify that the MHPs are promising gain media.[32]

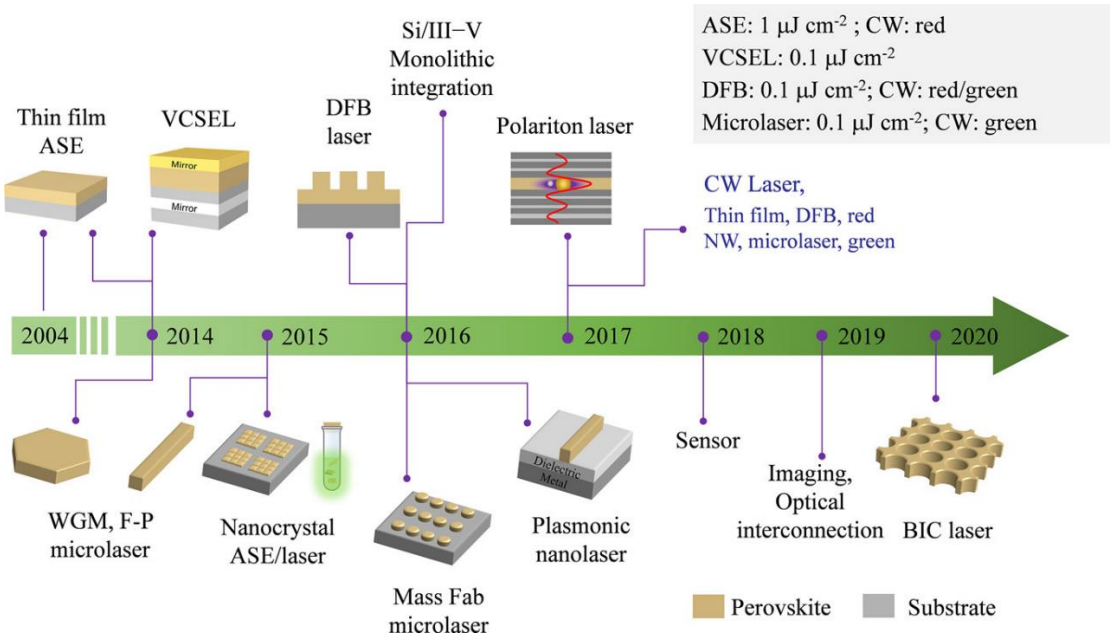

Figure 2.7 Summary of the development of MHPs lasers without or with a variety of cavities, including ASE, VCSEL, DFB, CW; WGM, F–P, nanowire, polariton laser, BIC (bound state in the continuum).[75]

2.4.1 Mechanism of Metal halide perovskites lasers

Before lasing is achieved, the carriers in the gain media should undergo a population inversion process, in which an incident photon can induce an excited carrier to relax to the ground state, and the relaxed carrier emits a photon simultaneously with the same energy and same phase. The total intensity is larger than the pumped intensity after this induced radiative relaxation process, which can amplify the incident light intensity. In contrast, If the total emission intensity is smaller than the incident light, the optical loss channels are dominant, such as nonradiative processes, scattering, and reabsorption process. MHPs are suitable for laser gain medium because they have a strong absorption coefficient ($\sim 10^4$-10^5 cm^{-1}), high PLQY (90%), low trap state, and a slow Auger recombination rate under high excitation power.[7, 76]

The optical properties of MHPs are determined by excitons, whose E_b govern their stability influenced by the temperature. So that the large E_b can increase the optical gains and reduce the nonradiative loss, which is suitable for emission sources. The E_b of MHPs is higher than that of commercial II−VI/III−V traditional materials, it is ~19-84 meV for 3D MHP and as high as 200 meV for 2D structures.[77, 78] therefore, the MHP nanocrystals and 2D MHPs with larger E_b due to the strong quantum confinement are favorable for applications in miniaturized laser devices.[77, 78]

2.4.2 Thin film lasers

MHP thin-film lasers have been widely reported due to their low-cost fabrication process and simple integrated platforms with varieties of cavities. The amplified spontaneous emission (ASE) achieved from MHPs films ($CsPbCl_3$) at low temperatures has been demonstrated by Kondo and co-workers as early as 2004.[79] Then the first room-temperature ASE was reported by Xing and co-workers through low-temperature fabricated MHPs films ($MAPbX_3$), and the emission wavelength covers the nearly whole visible spectra from 390 to 790 nm.[7] Among these MHP thin-film lasers have shown advantages in terms of low threshold(∼12 μJ cm^{-2} $pulse^{-1}$, fs pulse), high stability (9×10^7 laser shots), high crystalline quality, low defect state density, and low Auger recombination rate. Based on these advantages, MHP films laser have been widely studied by using a variety of A-site cations, such as MA, Cs, and long-chain organic chemical groups.[80-83]

One advantage of MHP thin films is they are easier to integrate with external cavities. For example, the room temperature MHPs VCSEL with a low threshold of tens of μJ cm^{-2} (ps pulse excitation) was achieved through $MAPbI_{3-x}Cl_x$ films combined with DBR and gold reflecting film, firstly reported by Deschler in 2014.[69] are promising lasing devices which can be applied in laser display and remote communications, because their large area beam surface can easily couple the emitting beam with a variety of shapes to optical fibers and very small divergence angles. A single-mode laser from

$MAPbI_3$ VCSELs was demonstrated by Chen and co-workers in 2017, showing a narrow FWHM of 0.24 nm and a low threshold of 7.6 μJ cm^{-2}. Furthermore, this VCSEL also exhibited a divergence angle is less than 3° and linear polarization as high as 81%, which confirms they are a good candidate for developing high collimated microlasers.[84]

2.4.3 Nanocrystal lasers

MHPs nanocrystal lasers are always related to emission from 0D MHP crystals with high quality and PLQYs, and the low-threshold lasing with flexible structures showed potential for application in miniaturizing lasers. The first MHP nanocrystal laser from $CsPbX_3$ nanocrystals was demonstrated by Yakunin and co-workers in 2015, which showed PLQY as high as 90% with a wide range of emission spectra from 440 to 700 nm.[85] This nanocrystal laser has a low threshold of 5.3 μJ cm^{-2} (100 fs pulse excitation) and a large net optical gain of about 450 cm^{-1}. From then on, numerous MHP nanocrystal lasers with different A-site cations or ratios of compositions have been reported.

Due to the high non-linear absorption coefficient of MHP nanocrystals, they are demonstrated upconversion lasers by multiphoton excitation, which can be potentially used in healthcare and bio-imaging. Wang and co-workers showed the multiple-photon

pumped lasing from $CsPbBr_3$ nanocrystals in 2016, and their two-photon absorption cross-section (~1.2×10^5 GM) at 800 nm was 2 orders of magnitude higher than traditional II−VI semiconductors.[86] However, the thresholds (@800nm, 2.5 mJ cm^{-2}) were 3 orders of magnitude higher than the single-photon laser, and emission intensity decrease fast in the ambient conditions. Therefore, the chemists cover the surface of MHPs nanocrystals with organic polymers or ligands to improve their stability. Core-shell structure was introduced to form moisture-resistance $CsPbBr_3/SiO_2$ nanocrystals, which have a lower threshold (230.8 μJ cm^{-2}) of two-photon lasing.[87] MHP nanocrystals VCSELs laser was first reported by Wang and co-workers in 2017, and CW laser pumped MHP nanocrystals coupled DFB cavity is also achieved in 2019.[88, 89]

2.4.4 Exciton-polariton lasers

As a new device concept, exciton-polariton laser (EPL) was reported in 1996, which can provide better lasing performance, such as enhanced coherent light and lower lasing threshold than traditional lasers.[90] The exciton-polariton laser is the laser beam from coherent polariton condensates, which is triggered by stimulated scattering of exciton−polaritons in the condensation regime, and amplified through strong coupling between cavity photons and excitons in microcavities. The exciton−polariton exists as a boson with the property of light-matter, so that they have a low effective mass the

same as the photon, and they also have strong nonlinearity like the exciton. These properties enable them an ideal candidate for achieving Bose−Einstein condensation, leading to coherent polariton condensates, which can escape as photons from the facet of microcavity to form the coherent emission, named polariton lasing. Therefore, these kinds of lasers are very different from the phonic lasers that need high excitation power to make population inversion, so the polariton lasers showed the lasing threshold is 1-2 orders of magnitude lower than the standard lasers.[91] The first MHPs polariton laser from $CsPbCl_3$ with planar microcavity at room temperature have been achieved in 2017.[92] Recently, polariton lasing was achieved from MHPs microcavity with periodic potentials, which helps investigate the Bloch dispersion in MHPs polariton lattice and allows fabricating of Hamiltonian systems.

2.5 Metal halide perovskites laser diodes in future

Numerous successful MHPs lasers have proven that they are promising laser gain medium; however, it is still a challenge to realize electrically pumped perovskite lasers due to the insufficient optical gain, a low electrical-to-optical conversion efficiency, and thermal effect. Here, the current progress on the lasing performance of optically pumped perovskite lasers is reviewed. Studying the advancement in the control of carrier transport and recombination properties of MHPs LEDs architectures, we analyze the obstacles preventing the fabrication of perovskite laser diodes. More importantly, a

strategy toward electrically driven perovskite lasers is proposed based on the successful development of organic semiconductor laser diodes.

2.5.1 Reduction of lasing threshold

The first step toward the realization of electrically pumped perovskite lasers is to minimize the corresponding excitation threshold through the appropriate design of gain material compositions and resonators.[93] This is because of the high crystal quality of the gain medium and the defect-free resonator can cause extremely low cavity losses.[94] For example, $MAPbBr_3$ thin-film laser with DFB structure is realized to sustain lasing emission at temperatures up to 100°C with a low threshold of 3.4 μJ cm^{-2} under optical pulses excitation (@532 nm, 0.3 ns).[95] The single-crystalline$CsPbBr_3$ nanowires (NWs) secure room-temperature lasing operation with a low threshold of 3 μJ cm^{-2} (@355 nm, 150 fs).[94] The lowest threshold of single-crystalline $MAPbX_3$ (X=I, Br, and Cl) NWs is recorded to be μJ cm^{-2} (@805 nm, 100 fs) at room temperature.[96] The current fabrication of VCSEL using a 1 mm thick $MAPbBr_3$ perovskite as the active layer has demonstrated an ultralow threshold of 34 mW cm^{-2} at room temperature under CW operation.[97] Although it is higher than the pulse laser pumped lasing threshold, it is a milestone toward electrically pumped MHPs lasers. The summary of optically pumped MHP lasers in past years is shown in **Table 1**. Now, the

question is whether these lasers can be electrically excited by using the MHPs LED architectures as the carrier injection media.

Table 2.1. Recent progress of optically pumped perovskite semiconductor lasers.

Materials	Feedback	Excitation method	Temp.	Threshold	Active layer thickness	Year
$MAPbI_3$ [7]	ASE	150 fs, 600 nm,	RT	12 μJ cm^{-2}	65 nm	2014
$CsPbBr_3$ [98]	WGM	5 ns, 400 nm	10 K	11.5 mJ cm^{-2}	in solution	2015
$MAPbI_3$ [96]	FP	150 fs, 402 nm	RT	0.22 μJ cm^{-2}	~200 nm	2015
$CsPbBr_3$ [99]	FP	150 fs, 402 nm	RT	2.8 μJ cm^{-2}	700 nm	2016
$CsPbBr_3$ [94]	FP	150 fs, 355 nm	RT	3 μJ cm^{-2}	300 nm	2016
$MAPbI_3$ [29]	VCSEL	0.34 ns, 532 nm	RT	7.6 μJ cm^{-2}	~305 nm	2017
$MAPbBr_3$ [95]	DFB	0.3 ns, 532 nm	RT	3.4 μJ cm^{-2}	~200 nm	2018
$MAPbI_3$ [32]	DFB	CW, 445 nm	102 K	17 kW cm^{-2}	120 nm	2017
$MAPbI_3$ [100]	DFB	CW, 355 nm	RT	0.1 W cm^{-2}	160+70 nm[a]	2018
$CsPbBr_3$ [101]	FP	CW, 405 nm	4 K	1.45 nW cm^{-2}	~280 nm	2018
$CsPbBr_3$ [102]	Polariton	CW, 450 nm	77 K	6 kW cm^{-2}	~300 nm	2018
$MAPbI_3$ [103]	DFB	CW, 355 nm	RT	13 W cm^{-2}	145+30 nm[a]	2018
$MAPbBr_3$ [104]	DFB	CW, 405 nm	RT	15 W cm^{-2}	300+700 nm[a]	2019
$MAPbBr_3$ [97]	VCSEL	CW, 405 nm	RT	34 mW cm^{-2}	1 μm	2019
$FAPbBr_3$ [83]	DFB	CW, 488 nm	RT	45 W cm^{-2}	~100 nm	2020

[a] $h_1 + h_2$ (h_1 – grating height, h_2 – perovskite residue thickness)

2.5.2 Critical problems in realizing MHP laser diodes

The thermal effect is the main problem with using the available LED architectures as an excitation source. It should be noted that the threshold carrier concentration or the threshold current density is dependent on the design of laser cavities as well as the transparency carrier concentration of the perovskite semiconductors. The injection current below the threshold current density contributes to the non-radiative recombination of carriers and generates heat–pump-induced heating.[105] It must be noted that transparency carrier concentration is an intrinsic property of perovskite semiconductors and cannot be changed by improving its crystal quality so that this inherent heating effect of perovskite lasers cannot be avoided. Hence, the main challenges to achieving electrically pumped perovskite lasers can now be focused on two issues: 1) How to minimize the 'heating effect' from the LED architectures under CW operation at high current density? 2) How to further reduce the excitation threshold to suppress pump-induced heating?

2.5.3 Proposed solutions in realizing MHP laser diodes

Perovskite semiconductors are suitable materials to realize polariton lasing because of their high excitonic binding energy and large exciton oscillator strength. So far, room-temperature optically pumped polariton lasing has been demonstrated from VCSELs,[103, 104] microcuboids,[105] and nanowires[99] using perovskite

semiconductor as the photon-exciton coupling region. The advantage of achieving polariton lasing is the immediate decay of polariton condensation to generate coherent monochromatic light so that no population inversion is required. Hence, only a small amount of excitation power is enough to turn on the polariton lasers so that pump-induced heating can be significantly suppressed.

Here, we propose to realize electrically pumped perovskite polariton lasers by adopting the design from the room-temperature GaN-based electrically pumped polariton lasers.[106, 107] This GaN polariton laser has a VCSEL structure where a thin GaN semiconductor layer is sandwiched between two Bragg reflectors. However, electrodes are not established between the two Bragg reflectors as in the conventional design of VCSELs, instead, the electrical current is injected into the emitting layer in the direction orthogonal to the path of optical feedback. This laser configuration avoids the injection of carriers through the Bragg reflectors so that Joule heating is mainly dependent on the design of the LED architecture. To realize perovskite polariton lasers, we can replace the GaN layer with a perovskite semiconductor film such as $MAPbBr_3$. A standard LED architecture such as NiO_x/$MAPbBr_3$/TPBI can also be used to side-inject electrons and holes to the perovskite semiconductor, in the direction perpendicular to the optical feedback of the resonator, shown in **Figure 2.8**. The Joule heating of the LED architecture can be further reduced if doping can be introduced to the carrier transport layers to reduce equivalent resistance. Furthermore, the diamond substrate can be used

to reduce the thermal resistance of the LED architecture. Hence, the reduction of thermal and equivalent resistance allows the room-temperature CW operation of LED architecture to deliver a high current. Hopefully, this suggestion can overcome the 'two issues' affecting the development of electrically pumped MHPs lasers.

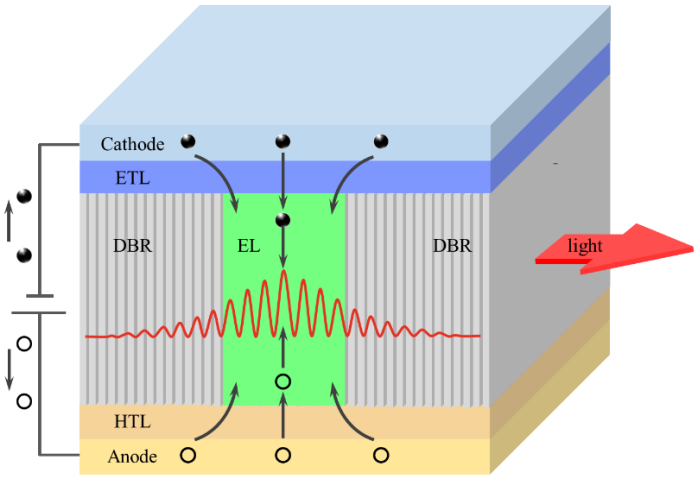

Figure 2.8 Proposed architecture of electrically pumped perovskite semiconductor laser. In this case, NiOx is the hole-transport layer, TPBI is the electron-transport layer and $MAPbBr_3$ is the emitting layer (EL). As we can see, the external injection of carriers is achieved via side injection to the EL. Lasing light is observed from the two end surfaces of the DBRs.

2.6 Conclusions

In conclusion, Numerous successful practices on MHPs lasers with a variety of compositions and dimensionalities, have verified that the MHPs with excellent optoelectrical properties are promising next-generation laser gain media. The lasing

performance of MHP lasers has been improved in the past several years, such as low lasing threshold, pure emission wavelength, wide range PL spectra, strong coherence, and so forth. However, electrically pumped MHPs laser is still difficult to realize, which would be the next frontier and have more practical applications. To achieve this goal, the lasing threshold should be reduced through high-quality MHPs with suitable cavities. Furthermore, the Joule heating should be well managed by reasonable structures of carrier transportation with a good thermal conductivity substrate. It is a must to simultaneously obtain strong confinement of carriers and photons within the emitting layer of the lasers to achieve stimulated emission, for which low dimensional MHPs with large E_b are favorable due to the quantum effect. Therefore, it is believed that we are not far from achieving electrically pumped perovskite lasers.

Chapter 3 Robust and flexible random lasing from 0D metal halide perovskites*

3.1 Introduction

Recently, extensive investigations have been concentrated on the realization of lasers on the plastic substrate due to their mechanical flexible characteristics suitable for the development of flexible optoelectronic systems.[108-112] For example, the deposition of ZnO nanoparticle embedded ZnO thin film on polycarbonate plastic substrate is proposed to realize flexible inorganic random lasers.[113] Organic lasers using solvent-free fluidic organic semiconductors as the gain medium, highly flexible corrugated polymeric patterns, and flexible polyurethane acrylate films as the resonator have also achieved mechanically single-mode tunable lasers.[114] Furthermore, organic dye spin-coated on a polyethylene terephthalate substrate embedded with silver nanoprisms has fabricated flexible random lasers with a high degree of wavelength tunability over 15 nm through the influence of localized surface plasmon and random scattering under mechanical bending.[109] On the other hand, using organic polymers has shown the possibility to obtain mechanical flexibility and lightweight substrate-less organic lasers

* Presented in the publication entitled "Robust and Flexible Random Lasers Using Perovskite Quantum Dots Coated Nickel Foam for Speckle-Free Laser Imaging. small, 2021. 221, e2103065. https://doi.org/10.1002/smll.202103065"

that can be deposited on any surface.[115] Spin coating of strong adhesive perovskite thin films on flexible polyimide substrates have also obtained flexible random lasers with the control of excitation threshold through mechanical bending.[116] Alternatively, a flexible gain medium - ZnO-enriched cellulose acetate fiber matrix doped with silver nanoparticles is fabricated as the flexible random cavities to realize flexible lasers.[117] These results verify the possibility to fabricate high-performance and functional flexible lasers which are the necessary components for the future development of flexible optoelectronic systems. Nevertheless, plastic substrates are usually more brittle than their flexible metal-grade counterparts such as metal porous foam to support plastic deformation.

Metal halides perovskites quantum dots (PQDs) have been recognized as optical gain materials over their bulk counterparts due to their insensitive to oxidization and moisture environment with lower thresholds.[118-121] Besides, the influence of quantum size effects and the use of colloidal structure can easily tune the energy bandgap as well as can enhance the emission intensity of the PQDs.[122, 123] The corresponding surface chemistry can also be modified to enable them to disperse into a variety of solvents and matrices, and even be integrated into various devices through their strong adhesive performance.[124-126] Recently, all-inorganic $CsPbX_3$ (X=Cl, Br, I) PQDs[127] with highly efficient luminescence were found that they are suitable to be utilized as laser gain materials.[98] More importantly, the combination of

optimized solvent engineering processes with PQDs facilitates the synthesis of high-quality solution-processed perovskite thin films on flexible substrates at a low cost.[128, 129] Therefore, metal halides PQDs are a potential laser gain medium for the fabrication of flexible lasers.

In this study, we propose the use of 1) Ni porous foam, which has a 3D structure of voids that tends to be stronger, flexible, and can sustain plastic deformation, as the laser substrate and 2) $CsPbBr_3$ PQDs as the gain medium to realize highly reliable and flexible lasers. Due to the strong light scattering capability of the voids of the Ni foam and the excellent optical gain properties of $CsPbBr_3$ PQDs, we demonstrated incoherent random lasing from the $CsPbBr_3$ PQDs coated Ni porous foam under optical excitation at room temperature. Furthermore, the emission characteristics of the flexible lasers can be tuned by controlling the surface morphologies of the Ni foam through deformation. It is also shown that the corresponding emission intensity is robust to extensive bending. On the other hand, due to the low spatial coherent characteristics of the flexible lasers, it is shown to be an ideal light source to produce high-quality micro-images. Hence, our proposed flexible and durable lasers are a potential speckle-free light source for the future application of flexible optoelectronic systems.

3.2 Experimental methods and instrument

3.2.1 Chemical materials

Cesium carbonate (99%) (Cs_2CO_3), Oleic acid (AR) (OA), octadecene (ODE), oleylamine (80%-90%) (OAm), lead bromide (99%) ($PbBr_2$) and methyl acetate (98%) were purchased from Shanghai Aladdin Biochemical Technology Co., Ltd. Toluene was purchased from Sigma-Aldrich, Inc. All chemicals were used without further purification. The Ni porous foam was purchased from Kunshan Xingzhenghong Electronic Materials Co., Ltd., with a size of about 0.3 × 200 × 500 mm^3.

3.2.2 Synthesis methods of 0D $CsPbBr_3$

$CsPbBr_3$ PQDs were synthesized via the method proposed by Protesescu *et al* with a slight modification.[127] A mixture of Cs_2CO_3 (0.4 g), OA (1.25 mL), and ODE (15 mL) was stirred under argon flow in a four-neck flask at 130 °C for about 10 min, and then raised the temperature to 150 °C until Cs_2CO_3 was completely reacted with OA and dissolved in the mixture. The mixture cooled down to room temperature, and this prepared Cs-precursor was stored in the glove box for further use. Another mixture of ODE (15 mL), OA (1.5 mL), OAm (1.5 mL), and $PbBr_2$ (0.2 g) was stirred under nitrogen at 130 °C for about 1 h. Then the temperature was raised to 180 °C after the $PbBr_2$ was completely dissolved and stirred for more than 10 min. Next, the Cs-precursor (1.5 mL) was injected into the above hot mixture as fast as possible, and the

reaction stopped 5 s later with an ice bath. The reaction solution was centrifuged, and the precipitate was removed. The $CsPbBr_3$ QDs were precipitated from the supernatant after adding the methyl acetate, and the mixture was centrifuged at 13,000 rpm for 6 min to obtain the $CsPbBr_3$ QDs. The $CsPbBr_3$ QDs were washed with toluene and methyl acetate several times, and they were dispersed in toluene as a stable solution to deposit on the Ni foam.

3.2.3 Instrument for material characterizations

Transmission electron microscopy (TEM) was carried out on a JEM-2100 electron microscope, operating at an acceleration voltage of 100 kV. Scanning transmission electron microscopy (STEM) was carried out on a JEM-2100F field-emission electron microscope, operating at an acceleration voltage of 200 kV. Scanning electron microscopy (SEM) images are captured by a JEOL Field Emission scanning electron microscopy. X-ray diffraction patterns (XRD) were acquired with a Bruker AXS D2 phaser X-ray diffractometer equipped with a Cu Kα radiation source (λ = 1.54 Å) at 40 kV and 30 mA. Absorption spectra and reflectance spectra were obtained on a PerkinElmer UV-vis-NIR spectrometer.

3.2.3 PL Measurement via Two-photon Excitation

A Ti:sapphire femtosecond laser (Coherent Libra), which generates femtosecond pulses (50 fs, 1 kHz) at 800 nm, was used as the excitation source. The laser beam, which has a diameter of ~8 mm, was focused onto the surface of the samples by a convex lens of 10 cm focal length. The light emitted from the surface of the samples was collected by an objective lens (20 × 0.8 NA objective lens) and coupled to a conventional charge-coupled device (CCD) camera for the recording of the near-field image or attached to a monochromator (Princeton SpectraPro 2750 integrated with a ProEM EMCCD camera with a spectral resolution less than 0.1 nm) for spectrum analysis.

3.3 Characteristics of 0D $CsPbBr_3$ with flexible substrate

3.3.1 Characteristics of $CsPbBr_3$ quantum dots

Figure 3.1a presents the X-ray diffraction (XRD) pattern of the $CsPbBr_3$ PQDs. The pattern matches the standard cubic crystal structure of $CsPbBr_3$ (PDF #54-0752). High-resolution transmission electron microscopy (HR-TEM) image of a $CsPbBr_3$ PQD given in the insert of **Figure 3.1** has shown that the corresponding nanocrystal length and lattice spacing (110) are equal to ~8 and 0.42 nm respectively. Hence, it is verified that the $CsPbBr_3$ PQDs are in the cubic phase. Scanning transmission electron microscopy (STEM) image of the monodisperse PQDs is also shown in **Figure 3.1b**. It is demonstrated that the $CsPbBr_3$ PQDs fabricated by the solution-phase synthesis have

a uniform size distribution. Moreover, energy-dispersive X-ray (EDX) elemental mapping images of a $CsPbBr_3$ PQD are given in **Figure 3.1c**. Cs, Pb, and Br elements are found to be homogeneously distributed over the entire volume which further confirms that the high-crystal-quality cubic phase PQDs were successfully synthesized. **Figure 3.1d** shows the optical characteristics of the $CsPbBr_3$ PQDs at room temperature.

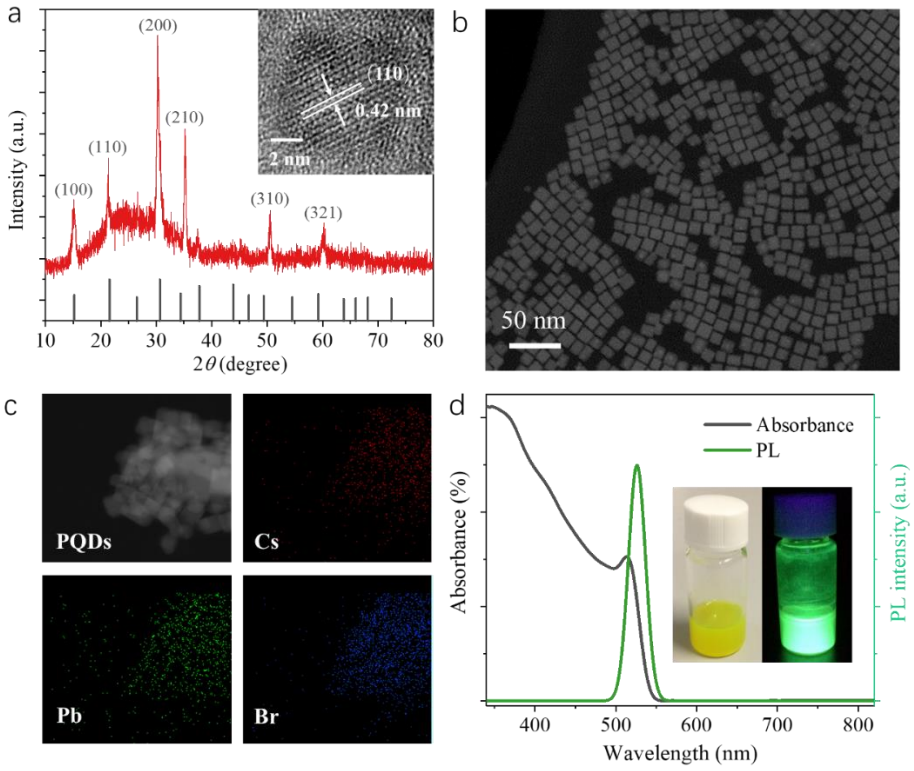

Figure 3.1 Physical characteristics of CsPbBr3 PQDs. (a) XRD pattern of PQDs film on the glass slide and standard card (PDF #54-0752). The inserted image shows the HR-TEM image of a PQD. (b) STEM micrograph of PQDs. (c) EDX elemental mapping images of PQDs. (d) Absorption and photoluminescence (PL) emission spectra of the $CsPbBr_3$ PQDs and the insert show the photos of the PQDs with and without UV light excitation.

3.3.2 Characteristics of 0D $CsPbBr_3$ coated Ni foam

Figure 3.2a describes the fabrication process of Ni porous foam coated with $CsPbBr_3$ PQDs (NFO-PQDs) by using the spin-coating method – a few drops of $CsPbBr_3$ PQDs dispersed in toluene are spin-coated onto the surface of Ni foam at a rotational speed of 600 rpm for 10 seconds and then 3000 rpm for 30 seconds, and this procedure is repeated for 3 times. The Ni foam, which can be purchased commercially, has a three-dimensional mesh structure with voids of diameter varying from 200 to 300 μm and a thickness of 300 μm (see **Figure 3.3**). **Figure 3.2b** and **Figure 3.2c** show the scanning electron microscope (SEM) images of the Ni foam before and after coating of $CsPbBr_3$ PQDs respectively. It is observed that the entire surface of the mesh structure is covered with $CsPbBr_3$ PQDs with an average thickness of about 200 nm (see **Figure 3.4a**). **Figure 3.4b** shows that the XRD pattern of NFO-PQDs is consistent with the standard card of $CsPbBr_3$ (#54-0752) and Ni (#87-0712), indicating that the $CsPbBr_3$ PQDs were successfully coated on the Ni foam. The $CsPbBr_3$ PQDs coating, which has an average RMS value of about 50 nm, has a rough surface after coating on the Ni foam. This is due to the surface roughness of the Ni foam. However, this surface roughness has less influence on the emission characteristics of the NFO-PQDs due to the domination of the mesh structure of the Ni foam.

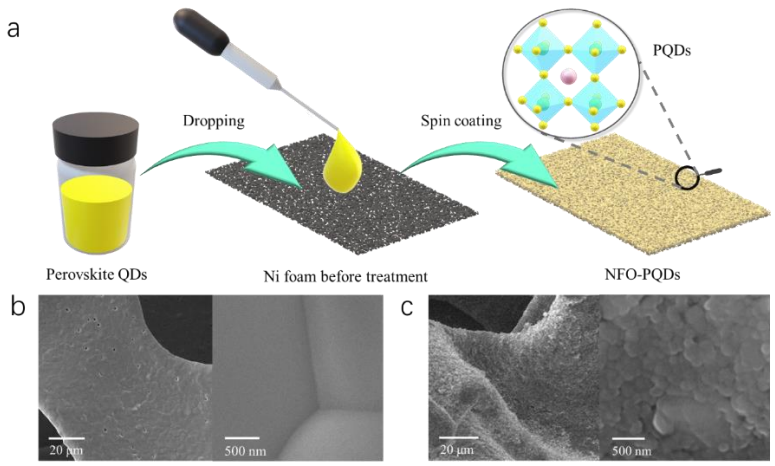

Figure 3.2 (a) Fabrication process of the Ni foam coated with $CsPbBr_3$ PQDs. SEM images of the surface mesh structure of the Ni foam (b) without and (c) with a coating of $CsPbBr_3$ PQDs.

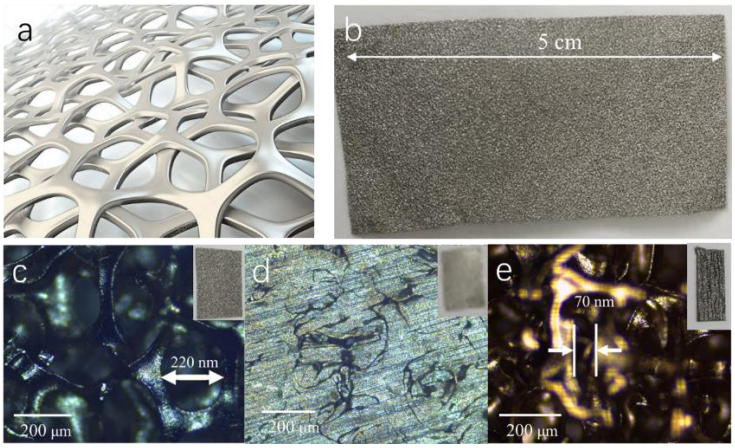

Figure 3.3 Optical images of Ni foams with different void diameters. (a) Schematic diagram of the mesh structure of the Ni foam. (b) Photo of the Ni foam. The microscope images of (c) original Ni foam with the void diameter of 200-300 μm, (d) flat Ni foam is obtained due to vertical compression applied to the surface of the Ni foam, and (e) horizontal compression applied to the surface of the Ni foam so that the diameter of the

voids reduce to 60-90 μm, as a result, the number of scatterers per unit length is increased. The inserts are photos of the samples.

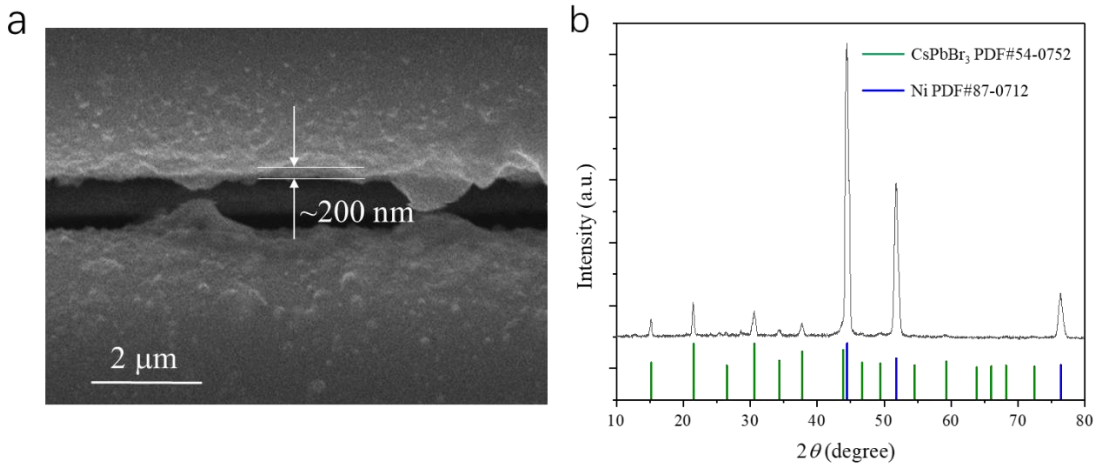

Figure 3.4 Characteristics of PQDs coated on the Ni foam. (a) Cross-section SEM image of the NFO-PQDs. The PQDs coating on the Ni foam has an average thickness of ~200 nm. (b) XRD pattern of PQDs coated Ni porous foam. The XRD pattern well matches that of the $CsPbBr_3$ (green color) and Ni (blue color).

3.4 Investigation of lasing performance from zero-dimensional $CsPbBr_3$

3.4.1 Incoherent random lasing

An 800 nm femtosecond laser was used to examine the PL emission characteristics of the as-prepared NFO-PQDs under two-photon excitation at room temperature. The reason for using 800 nm excitation wavelength is its less surface absorption at the surface of Ni so that the PQDs layer can sustain multi-reflection to improve the

excitation efficiency of NFO-PQDs (see **Figure 3.5**).[130] **Figure 3.6a** shows the PL spectra of the as-prepared NFO-PQDs versus the increase of excitation power. A broad emission peak with a peak wavelength at ~525 nm appears in the emission spectra for the excitation power less than 190 μJ cm^{-2}. However, a narrow peak with a peak wavelength at ~537 nm emerges from the emission spectra for the excitation power equal to or larger than 190 μJ cm^{-2}. **Figure 3.6b** plots the corresponding light-light curve and full width at half maximum (FWHM) linewidth of the emission spectra. A kink at power ~190 μJ cm^{-2} appears in the light-light curve and the corresponding FWHM linewidth of the emission spectra reduced significantly from 16 to 1 nm for the increase of excitation power from the kink. Hence, the kink is considered as the excitation threshold, P_{th}, of the sample and the as-prepared NFO-PQDs support lasing emission at room temperature. **Figure 3.6c** shows the angle-resolved PL spectra of the sample at different observation angles, θ, under high power excitation (i.e. >> P_{th}). It is noted the profile of the PL spectra is different at different elevation angles and the corresponding linewidth is less than 1.5 nm. The insert of **Figure 3.6c** presents the near-field emission beam profile of the PL spectra which shows strong light scattering at different angles from the surface of the NFO-PQDs. **Figure 3.6d** plots the polarization characteristics of the as-prepared samples below and above the excitation threshold. For the sample biased below the threshold, the emission light is unpolarized. For the sample excited above the threshold, the emission light is partially polarized. Hence, it is verified that the as-prepared samples support incoherent random lasing at room

temperature due to the following reasons: 1) the observation of kink and narrowing of linewidth suggests laser behavior, 2) as the sample has no defined laser cavity, the variation of spectral and spatial profile at different elevation angles suggests the presence of random light scattering inside the NFO-PQDs, and 3) the observation of partial polarization and the absence of sharp peaks (i.e. linewidth < 0.2 nm) suggest the feedback mechanism is incoherent optical feedback.[131]

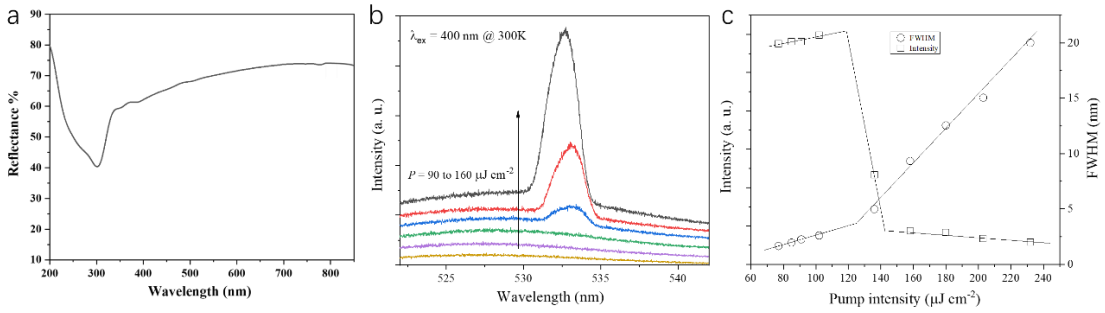

Figure 3.5 Emission characteristics of NFO-PQDs under 400 nm fs laser excitation at room temperature. (a) The reflectance spectra of original Ni foam without pressure (Normal). (b) Emission PL spectra were measured at different excitation power. (c) Output intensity and linewidth at various excitation power.

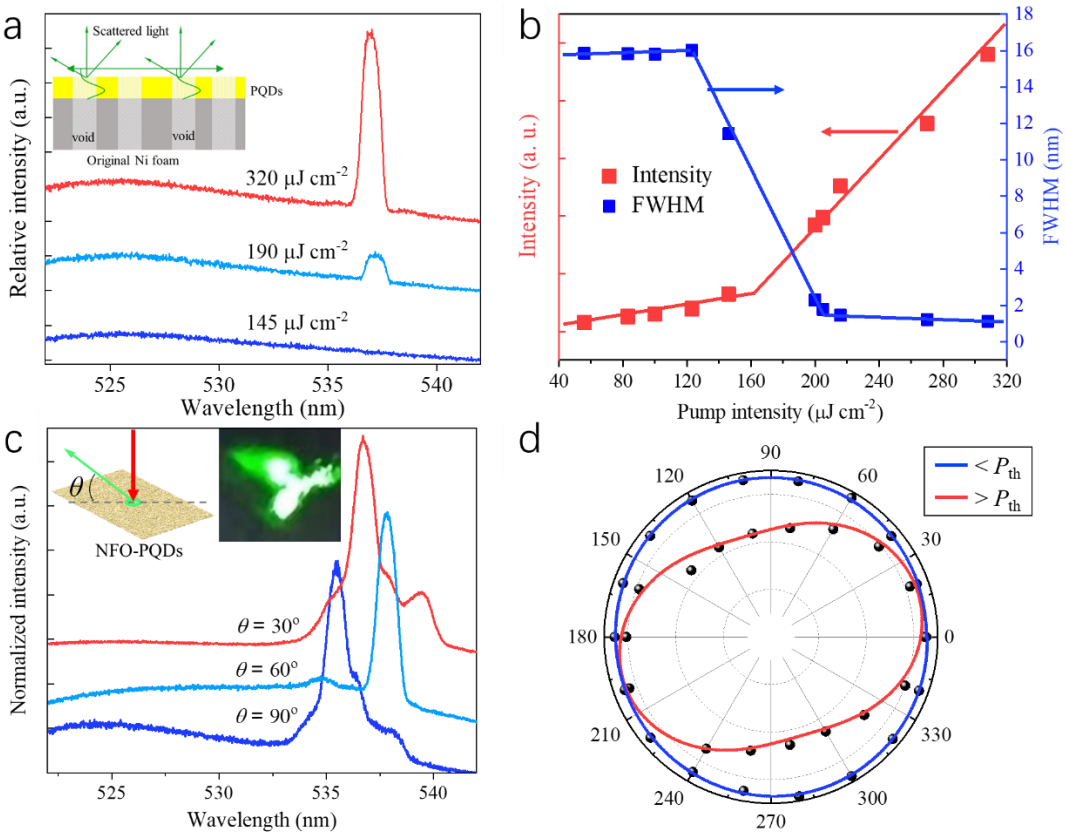

Figure 3.6 Random lasing characteristics of as-prepared NFO-PQDs. (a) Power-dependent PL spectra. Insert schematically explains how guided modes interact with the NFO-PQDs. (b) Output intensity and linewidth at various excitation power. (c) Observation-angle-dependent PL spectra. Insert shows the corresponding near-field profile observed at 30°. (d) Output intensities at different polarization angles for the excitation power below (blue line) and above (red line) P_{th}. The sample is excited by an 800 nm fs laser at room temperature.

3.4.2 Incoherent optical feedback from the mesh structure of the flexible substrate

Here, we study the influence of surface morphologies of the Ni foam on the lasing characteristics of NFO-PQDs. We consider the cases for Ni foam under deformation by external compression from horizontal and vertical directions (**Figure 3.7**). After the deformation of the Ni foam, $CsPbBr_3$ PQDs will be spin-coated onto the samples by the same method above. The PL emission characteristics of $CsPbBr_3$ PQDs with the Ni foam that underwent vertical compression are demonstrated in **Figure 3.8**. Due to the high vertical pressure, the voids of the Ni foam fill up with the material underneath them so that a flatted Ni surface is obtained. Hence, the spin-coated PQDs layer forms a waveguiding layer on the flat Ni surface with strong optical confinement, see the insert of **Figure 3.8a**. From the studies shown in **Figure 3.8b**, the narrowing of emission peak from 15 to 3 nm occurs when the excitation power exceeds a threshold P_{th} ~225 μJ cm^{-2}. However, the profile of the emission spectra is independent of the elevation angle of observation. These phenomena imply that the sample only supports amplified spontaneous emission (ASE) as voids are absent from the surface of the Ni foam to support light scattering. It should be noted that ASE has a slightly higher P_{th} than that of the incoherent random lasing due to the absence of optical scatterers.

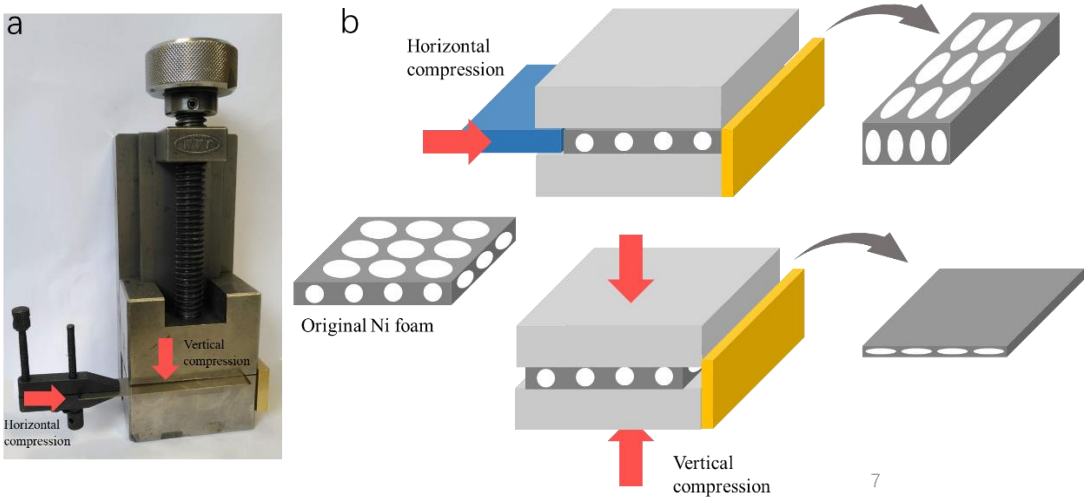

Figure 3.7 Schematic diagram of the deformation of Ni foam. (a) The device is used to apply vertical and horizontal compression to deform the Ni foam. (b) Schematic diagram to explain how the vertical and horizontal compressions are applied to deform the mesh structure of the Ni foam.

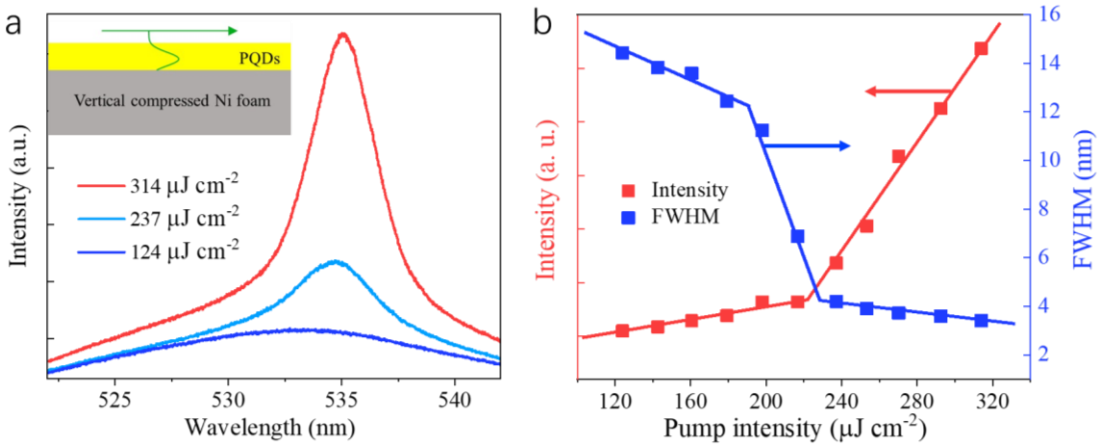

Figure 3.8 Emission characteristics of NFO-PQDs with vertically compressed Ni foam under 800 nm fs laser excitation at room temperature. (a) Emission PL spectra were measured at different excitation power. Insert schematic explains how guided modes interact with the compressed NFO-PQDs. (b) Output intensity and linewidth at various excitation power.

Figure 3.9 plots the PL emission characteristics of the sample with the Ni foam that underwent horizontal compression after deposition of $CsPbBr_3$ PQDs. In this case, the diameter of the voids is reduced to between 60 and 90 μm. Therefore, the number of voids per unit area is increased when compared to that of the original sample. (see the insert of **Figure 3.9a**). As shown in **Figure 3.9a** and **3.9b**, the narrowing of FWHM linewidth (i.e., from 25 to 1 nm) is observed when the excitation power exceeds a threshold P_{th} ~100 μJ cm^{-2}. On the other hand, **Figure 3.9c** shows that the angle-resolved PL spectra of the sample at different observation angles, θ, under high power excitation (i.e., >> P_{th}) are different. The corresponding emission light is also partially polarized at the excitation above the threshold, see **Figure 3.9d**. Therefore, the sample support incoherent random lasing but the corresponding P_{th} is reduced by half when compared to that given in Figure 3. The reduction of excitation threshold can be understood by the increase in the number of voids (i.e., number of optical scatterers) per unit area experienced by the optical modes. Previous analysis of random lasers has shown that lasing threshold intensity P_{th} decreased with the light transport length, l_t through the relationship of $P_{th} \propto l_t^{1/2}$.[132] In our NFO-PQDs, the transport length of the scattered light should be roughly equal to the diameter of the voids. As the diameter of voids of the original Ni foam and that after horizontal compression are ~220 and ~70 μm respectively, the value of P_{th} for the horizontal compressed NFO-PQDs should be reduced by ~2 folds. This is roughly consistent with our measurement of P_{th} shown in previous results.

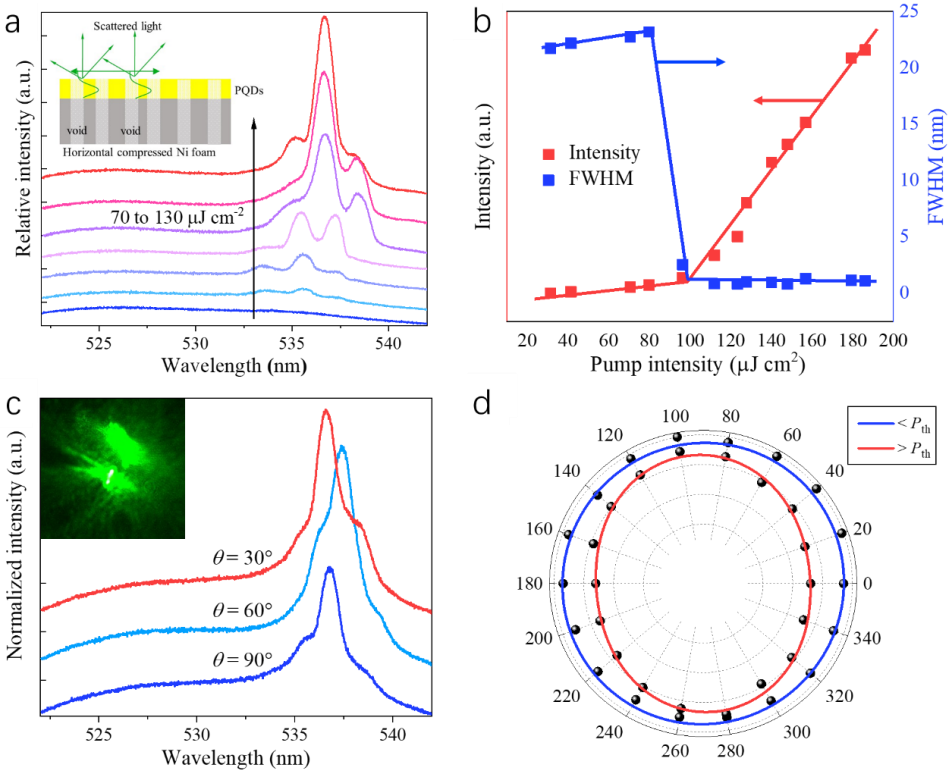

Figure 3.9 Emission characteristics of NFO-PQDs with a horizontally compressed Ni foam under 800 nm fs laser excitation at room temperature. (a) Emission PL spectra were measured at different excitation power. Insert schematic explains how guided modes interact with the compressed NFO-PQDs. (b) Output intensity and linewidth at various excitation power. (c) Emission spectra were detected at different angles for lasing mode. Insert shows the corresponding near-field profile observed at 30°. (d) Output intensities at different polarization angles for the excitation power below (blue line) and above (red line) P_{th}.

3.4.3 The reliability of flexible 0D $CsPbBr_3$ lasers

One of the main advantages of using Ni foam as the substrate is its mechanical flexibility. **Figure 3.10** studies the influence of bending on the emission characteristics of the as-prepared NFO-PQDs. The schematic diagram of the experimental setup is shown in **Figure 3.10a**. In the experiment, the NFO-PQDs are bent by sticking the coated Ni foam on a rod of a different radius, *r*, which varies from 20 to 4 mm. It is found that the measured emission characteristics with different curvatures (i.e., 1/*r*) are similar to that of Figure 3 so they are not repeated here. **Figure 3.10b** plots the corresponding P_{th} versus curvature of the bent NFO-PQDs. It is noted that P_{th} increases with the increase of curvature (i.e., reduction of *r*).[116] The increase in the threshold can be attributed to the increase in the diameter of the voids due to the bending of the Ni foam.

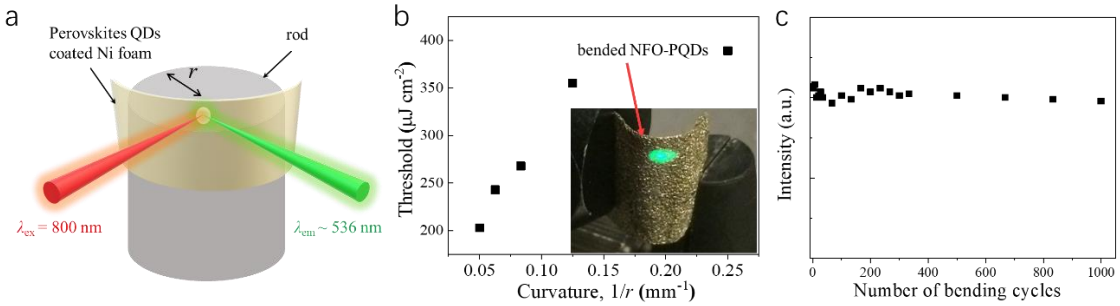

Figure 3.10 Experiment to measure the bending effect on the emission characteristics of as-prepared NFO-PQDs. (a) Schematic diagram of the experimental setup. (b) A plot of lasing threshold (P_{th}) versus curvature (1/*r*) of the NFO-PQDs. Insert shows the

photo of the experimental setup. (c) A plot of output intensity of lasing versus the number of bending cycles.

The reliability of using NFO-PQDs as flexible lasers under the influence of long-term bending and scratching is an important advantage for practical application. Here, the stability of the lasing characteristics of the NFO-PQDs is studied by measuring the corresponding lasing intensity versus the number of bending cycles. **Figure 3.10c** shows the lasing intensity versus the number of bending cycles of an as-prepared NFO-QDs. In the experiment, one bending cycle represents the NFO-QDs bends by 45^{o} with a bending curvature of 0.05 mm^{-1} and returns to its original location. As we can see, the NFO-PQDs after 1000 bending cycles demonstrate a slight change of emission intensity so that the lasing performance remained unchanged and the flexible NFO-PQDs are stable over many bending cycles. The main reason for the stability of using Ni foam as a substrate over the other organic substrate is metal in general is stronger than organic materials as well as the well-controlled structure.

3.5 0D $CsPbBr_3$ lasers applicated in speckle-free laser imaging

The high luminescence efficiency of lasers can be used as ideal light sources in optical imaging systems. However, the strong coherence of lasing light causes a ‘speckle’

problem (i.e., interference patterns of high spatial coherence light), which limits the corresponding quality of images. Fortunately, the emission characteristics of random lasers, which have a low spatial coherence of lasing light, can produce a speckle-free optical image.[133] **Figure 3.11a** shows an experimental setup for the use of NFO-PQDs as a laser source to produce a speckle-free optical image. **Figure 3.11b** and **3.11c** compare the illuminated images obtained from using a commercial green laser and our NFO-PQDs respectively as the light sources. As shown in **Figure 3.11b**, laser speckles appear from the resolution test pattern under green laser illumination. On the other hand, sharp images are observed from the CCD under the as-prepared NFO-PQDs illumination, see **Figure 3.11c**. These results indicate that our as-prepared NFO-PQDs can provide low spatial coherence light which finds applications in the modern imaging systems as a flexible light source.

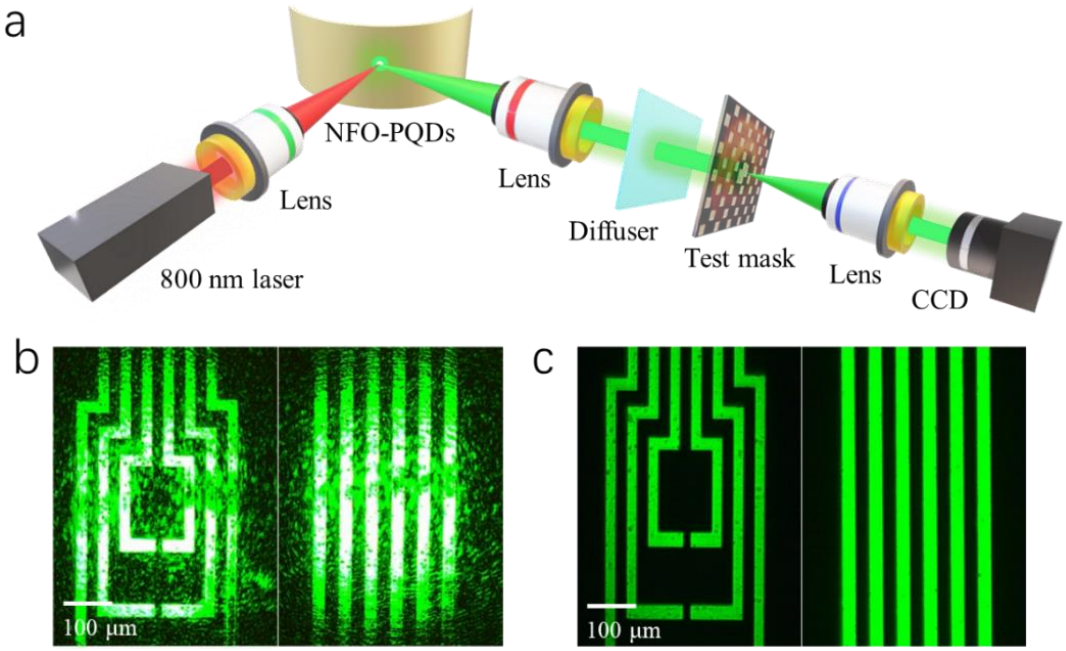

Figure 3.11 Optical imaging of micro-size patterns via a commercial laser and our as-prepared NFO-PQDs at room temperature. (a) Schematic diagram of the experimental setup for speckle-free imaging using the as-prepared NFO-PQDs as the illumination source. (b) The speckle image was generated from a commercial laser with a wavelength of 530 nm. (c) The speckle-free image was obtained by the as-prepared NFO-PQDs.

3.6 Conclusions

In conclusion, we verified the possibility to realize random lasers by deposition of PQDs via spin coating onto the flexible Ni foam. Incoherent random lasing is observed from the NFO-PQDs under two-photon excitation at room temperature. We also noted that the surface morphologies of the Ni foam determine the lasing characteristics of the

NFO-PQDs and can be tuned by deforming the Ni foam. Flatted surface of Ni foam can only support ASE from the NFO-PQDs. On the other hand, the presence of the voids of the Ni foam supports incoherent random lasing and the corresponding lasing threshold is dependent on the size of the voids. More importantly, due to the flexibility and bending durability of the Ni foam, random lasing characteristics of the NFO-PQDs can be sustained over a long bending cycle without a significant reduction in emission intensity. The advantage of incoherent random lasing is also demonstrated by using NFO-PQDs as the illumination light source to achieve ‘speckle’ free optical imaging. Hence, it is believed that the proposed flexible random lasers can find potential applications in flexible and wearable optoelectronics.

Chapter 4 Upconversion lasing from two-dimensional homologous Ruddlesden–Popper perovskite*

4.1 Introduction

Halide perovskites have been demonstrated with outstanding optical properties for light-harvesting and emission applications, such as solar cells, light-emitting diodes, photodetectors, lasers, etc.[7, 134-136] Among different dimensional halide perovskites, two-dimensional (2D) Ruddlesden–Popper Perovskites (RPPs) with high stability have attracted much attention in the community.[137, 138] 2D RPPs have a general chemical formula of $L_2A_{n-1}M_nX_{3n+1}$, where L represents a large cation (i.e., PEA^+ or BA^+), A can be an organic (i.e., MA^+) or inorganic cation (i.e., Cs^+), M is a metal cation (i.e., $Pb2^+$), and X is a halide. This 2D layered material composites of inorganic perovskites separated by the organic spacing group to form a multiple quantum well (QW)-like structure with strong spatial confinement of excitons, and the integer *n* represents the number of inorganic perovskites layers in a unit QW structure.[139-141]

* Presented in the publication entitled "Two-Photon Lasing from Two-Dimensional Homologous Ruddlesden–Popper Perovskite with Giant Nonlinear Absorption and Natural Microcavities" ACS Nano. 2022;16(8). https://doi.org/10.1021/acsnano.2c05726"

The enhanced exciton confinement in the multiple QW-like structures enables 2D RPPs to exhibit strong nonlinear optical characteristics including third-harmonic generation,[142, 143] multiple excitons interaction,[144, 145] and third-order optical nonlinearities with large nonlinear refraction.[146] Furthermore, nonlinear absorption plays a significant role in nonlinear photonics applications, such as frequency upconversion lasing and high-resolution bioimaging.[121, 147, 148] Recently, the two-photon absorption (TPA) coefficient of 2D RPPs with n = 1 is at least one order of magnitude larger than that of the typical semiconductor nanostructures. This observation indicates that the QW-like 2D RPPs are potential materials for next-generation nonlinear nano-photonics.[149] However, TPA characteristics of 2D RPPs with n > 1 have yet to be clarified. Hence, it is necessary to systematically investigate the nonlinear absorption characteristics of RPPs for more potential applications.

Lasing emission has been demonstrated from RPP films which can be fabricated by the spin-coating technique or solution-crystallization method (i.e. drop-casted microplate).[150-154] These quasi-2D perovskites compose of mixed dimensionalities containing various n values, and the optical gain mechanism is realized via efficient exciton localization from low- to high-dimensional active layers. However, lasing emission was mainly demonstrated from RPP films with a large value of n close to infinity.[10] Another limitation of these RPP films is the difficulty to control the uniformity of n values, leading to the shift in absorption and emission energy. On the

other hand, 2D RPP flakes can be fabricated by mechanically exfoliating the layered homologous RPP single crystals.[155, 156] Currently, lasing emission is observed from homologous RPP bulk or the mechanically exfoliated flakes with a large value of n (≥ 3).[155, 156] The main advantage of using mechanically exfoliated homologous RPP flakes are the formation of a single-n QW-like structure, based on which QW laser diodes can operate at high temperature due to the strong excitonic confinement of external injection of energetic carriers.[157] A recent report on the strong light-matter coupling in 2D RPP flakes (with n = 1) Fabry–Pérot (FP) microcavity has verified the enhancement of excitonic confinement and binding energy at room temperature [138, 158, 159]. These findings indicate that the QW-like structure may favor the capture of external carrier injection so that 2D RPP flakes with $n < 3$ are more likely to achieve electrical pumped lasing. Unfortunately, neither quasi-2D RPP films nor 2D RPP flakes with $n < 3$ support lasing emission even under low-temperature operation.

In this paper, upconversion lasing is realized from the mechanically exfoliated homologous 2D $(PEA)_2(MA)_{n-1}Pb_nI_{3n+1}$ RPP flakes under two-photon excitation at low temperature. An open aperture micro Z-scan technique is applied to explore the nonlinear optical absorption response of a single RPP flake. Importantly, the gain mechanism is revealed through the investigation of the modal and threshold characteristics of the RPP flakes with an FP microcavity. The transient absorption spectroscopy is also applied to study the loss mechanism of the RPP flakes. We find

that the flakes exhibit a non-saturated giant TPA coefficient of 3.6×10^3 cm GW^{-1} under 800 nm 50 femtosecond (fs) pulses excitation. Furthermore, RPP flakes with $n \geq 2$ demonstrate lasing emission at wavelength varies from 598 to 637 nm under two-photon excitation at low temperature (≤ 153 K). The reasons for supporting upconversion lasing emission can be attributed to the non-saturated giant TPA coefficient, high differential gain coefficient, and low non-radiative biexciton Auger recombination rate of the RPP flakes. However, the significant increase of non-radiative Auger recombination arising from the strong quantum confinement overwhelms the differential gain so that lasing is suppressed for the RPP flakes with $n = 1$ even operating at 78 K. Hence, our investigations provide fresh insight into the design of electrically pumped 2D RPP lasers.

4.2 Experimental methods and instrument

4.2.1 Fabrication Methods

RPP crystals were prepared by cooling-induced crystallization following the procedures previously reported.[160-162] For $n = 1$ RPP, 1 mmol of PbO (99.9%) was dissolved in 1 mL of HI (55%) and stirred until a clarified solution was observed to obtain PbI_2 solution. Then a mixture of hypophosphorous acid and 1 mmol of PEA was added to the above PbI_2 precursor solution to form an orange precipitate of $n = 1$ RPP from a bright yellow solution. For RPP with $n = 2$ and $n = 3$, a separate mixture of MA

dissolved in HI was added to the above mixture of PbI_2 and PEA solution and heated to 130 °C with stirring until the solution is clear. Next, the solution was cooled down to room temperature until the RPP crystal was formed.

4.2.2 Instrument for material characterization

The RPP flakes XRD measurement was performed using a Riguku Smartlab X-ray diffractometer operated at room temperature. The UV-vis absorption spectrum of a single RPP flake was analyzed by our homemade micro-spectrum analysis. White light is collimated on the entire surface of a single RPP flake and the transmitted signal was recorded through a microscope (Olympus BX51) via an objective lens (×10/0.3 NA Olympus MPlanFL N). The transmission spectra with and without the presence of the RPP flake were studied through a spectrum analyzer (Ocean Optics USB 2000+VIS-NIR with resolution <1.5 nm).

4.2.3 Lasing measurement of the RPP flakes

For femtosecond laser pulses excitation measurements, a Ti:sapphire laser (Coherent Libra) was used as the excitation source to generate femtosecond pulses (50 fs, 1 kHz) at the emission wavelength of 800 nm. The laser beam was focused on the surface of the RPP flakes, which were located inside a low temperature (i.e., varies from 77 to 300 K) chamber (Linkam DSC 600 temperature-controlled stage) purged with N_2 gas, by

an objective lens (×10/0.3 NA and ×50/0.65 NA Olympus MPlanFL N). Light emitted from the surface of the sample was recorded through the same objective lens which was coupled to a monochromator (Princeton SpectraPro 2750 integrated with a ProEM EMCCD camera with a spectral resolution less than 0.1 nm) through an optical fiber for spectrum analysis.

4.2.4 Micro Z-scan technique

A schematic diagram of the micro Z-scan experimental setup is shown in **Figure 4.6**. The Ti:sapphire laser (Coherent Libra) femtosecond laser (800 nm, 50 fs, 1 kHz) was used as the light source. The laser light was split into two beams through a 50:50 beam splitter. The reflected beam is focused on detector 1 (Thorlabs amplified Si photodetector) by convex lens 1. The transmitted beam is aligned to a microscope (Olympus BX51) and the laser beam is focused onto the surface of a single RPP flake through a long working distance objective lens (Mitutoyo M Plan Apo 10x/0.28 NA) and the transmitted light is focused on another photodetector 2 (Thorlabs amplified Si photodetector). Dividing the value of the pulse peak received from detector 1 with that obtained from detector 2 through the use of the oscilloscope, the influence of laser power fluctuation can be reduced. The sample, which sits on a motorized stage (Sigma Koki SGSP60-10ZF), is allowed to move between the objective lens and convex lens 3

by a small distance (± 3 mm) along the z-direction. The size of the flakes was selected to be larger than the maximum beam size.

4.3 Characteristics of 2D perovskites

In the experiment, we synthesized the RPP bulk crystals with n = 1, 2, and 3 with layered structures (**Figure 4.1**) by using a modified off-stoichiometry method reported previously.[139, 141, 161, 163] **Figure 4.2a** shows the schematic diagram of a single unit homologous $(PEA)_2(MA)_{n-1}Pb_nI_{3n+1}$ RPP crystal (take n = 2 as an example), consisting of an inorganic well layer sandwiched between two organic barrier layers. The barrier layers are made of PEA while the inorganic well layer is formed by the corner-sharing octahedral $[PbI_6]^{4-}$ embedded with MA, and the value of n represents the number of octahedral layers. Hence, the RPP crystal possesses a naturally formed QW-like structure. The RPP flakes are obtained by mechanical exfoliation from the as-grown RPP bulk crystals using scotch tape and then transferred onto quartz or SiO_2/Si substrates for optical analysis. The crystal structure and purity of the RPP flakes are confirmed by the X-ray diffraction (XRD) patterns shown in **Figure 4.2b**. For n = 1, the diffraction peak originates at 5.42° corresponding to (002) reflection. The periodic peaks confirm the single crystalline nature with [110] preferred crystal growth direction. For n > 1, 2, θ of the peaks reduce with the increase of unit cell thickness (i.e. addition of perovskite layers). This change is evidenced by the shift of the XRD pattern – the

(020) reflection peak shifts from 4.08° to 3.19° for $n = 2$ to $n = 3$ respectively. In contrast to $n = 1$, the repetition of (0k0) peaks suggests a preferential orientation along [101] direction for $n > 1$.[164] The XRD patterns indicate that all RPP flakes are single crystalline and have a nearly pure phase.

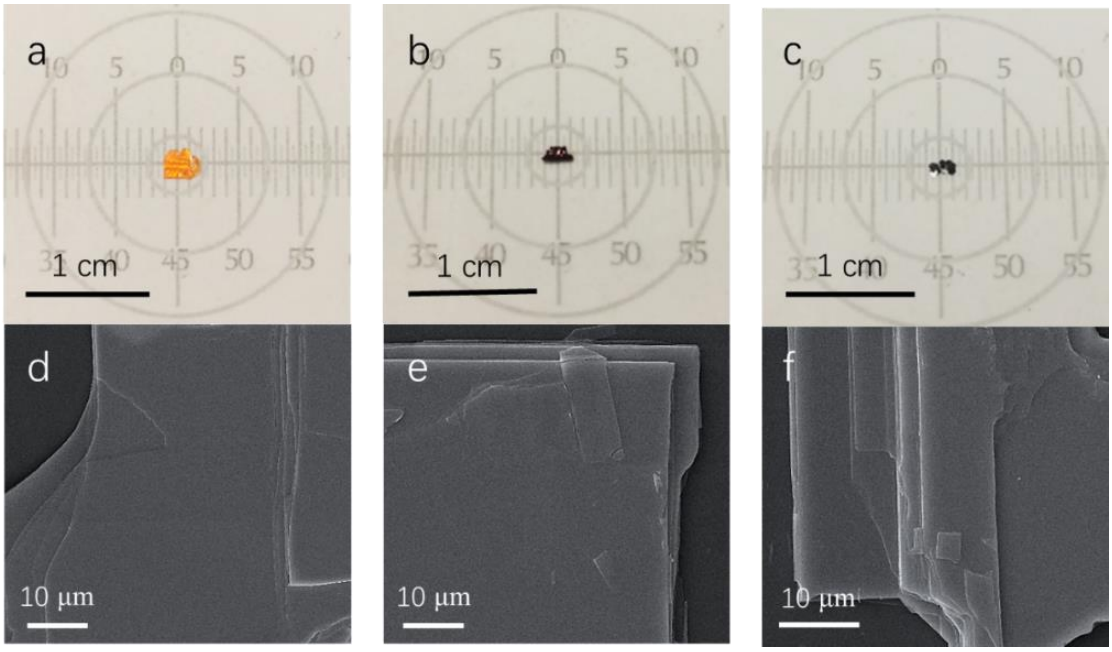

Figure 4.1 Optical and SEM images of bulk $(PEA)_2(MA)_{n-1}Pb_nI_{3n+1}$ RPP with the n = 1 (a) and (d), 2 (b) and (e), and 3 (c) and (f), respectively. Layered structures can be seen from the SEM images. With the increase of n, the color of RPPs changes from orange to dark red and black.

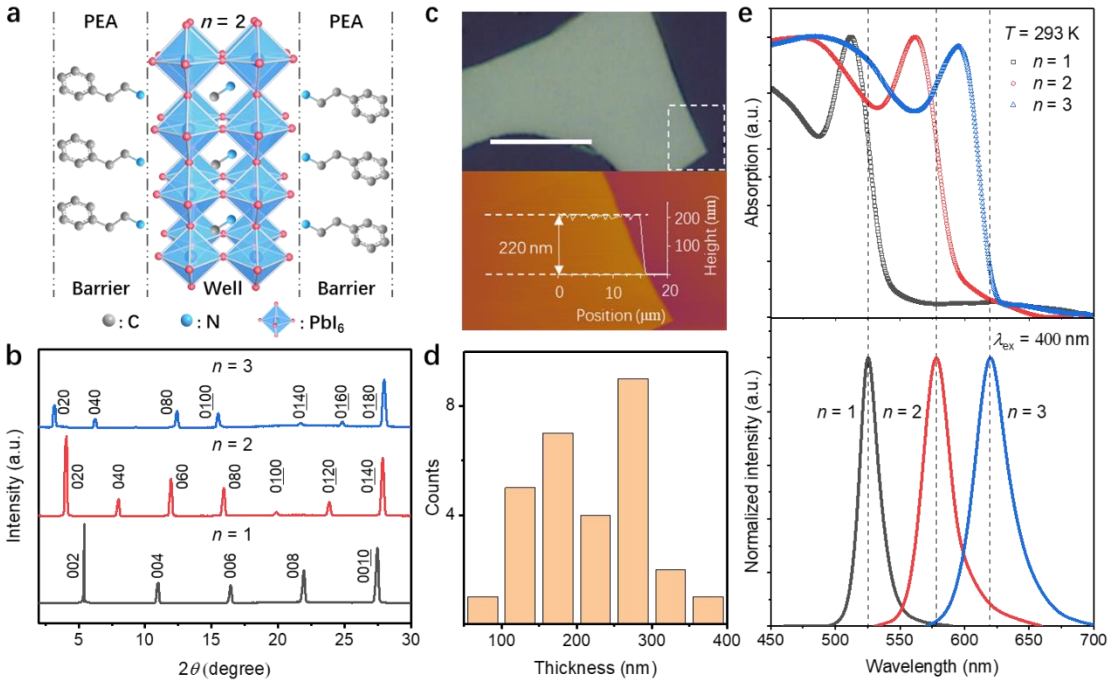

Figure 4.2 Structure and optical characterizations of RPPs. (a) Schematic diagram of a homologous RPP structure (n = 2 as an example). (b) XRD patterns of RPP flakes with n = 1, 2, and 3 from bottom to top panels, respectively. (c) Optical image (top) of an RPP (n = 2) flake (scale bar: 50 μm), and the AFM microphotography (bottom) of the square area labeled in the top image, inset: the corresponding height profiles. (d) Typical thickness distribution of mechanical exfoliated RPP (n = 2) flakes used for optical analysis. (e) Room-temperature absorption (top panel) and PL emission spectra of the RPP flakes with n = 1, 2, and 3 (bottom panel). The PL emission was excited by a 400 nm fs pulse laser.

Figure 4.2c shows an optical microscopy image (top panel) and atomic force microscopy (AFM) image (bottom) of a flake with *n* = 2 and a thickness of ~220 nm. The uniform color throughout its top surface exhibits the atomically flat surface with

good optical quality. Other flakes with different n values have similar optical characteristics (see **Figures 4.3**). The thickness of the mechanically exfoliated RPP (n = 2) flakes for the next optical analysis was selected between 70 and 400 nm due to the low radiation loss and good confinement in this range,[155] and their typical distribution profile is plotted in **Figure 4.2d**. **Figure 4.2e** compares the room-temperature optical absorption (top panel) and photoluminescence (PL) spectra (bottom panel) of the RPP flakes with n = 1, 2, and 3, respectively. For the absorption spectra, all samples exhibit a single sharp excitonic absorption resonance, and the bandgap energy (E_g) decreases with the increase of n. This is because the increase in n represents the increase in well thickness (i.e. inorganic octahedral layer) so that the energy of quantum confinement is reduced. The measured values of E_g are 2.42 eV (512 nm), 2.20 eV (564 nm) and 2.10 eV (590 nm) for samples of n = 1, 2, and 3 respectively. Compared to their 3D counterpart,[148] the large shift between the excitonic peaks and the absorption band edges suggests a large exciton binding energy in these 2D materials, due to a strong electron-hole Coulomb interaction in the QW-like structure.[158] For the PL spectra, all three samples exhibit a single emission peak under λ_{ex} = 400 nm fs laser excitation, and the PL peak wavelength is found to be 525, 580, and 623 nm for n equal to 1, 2, and 3 respectively, which also confirm that each sample contains the pure phase.

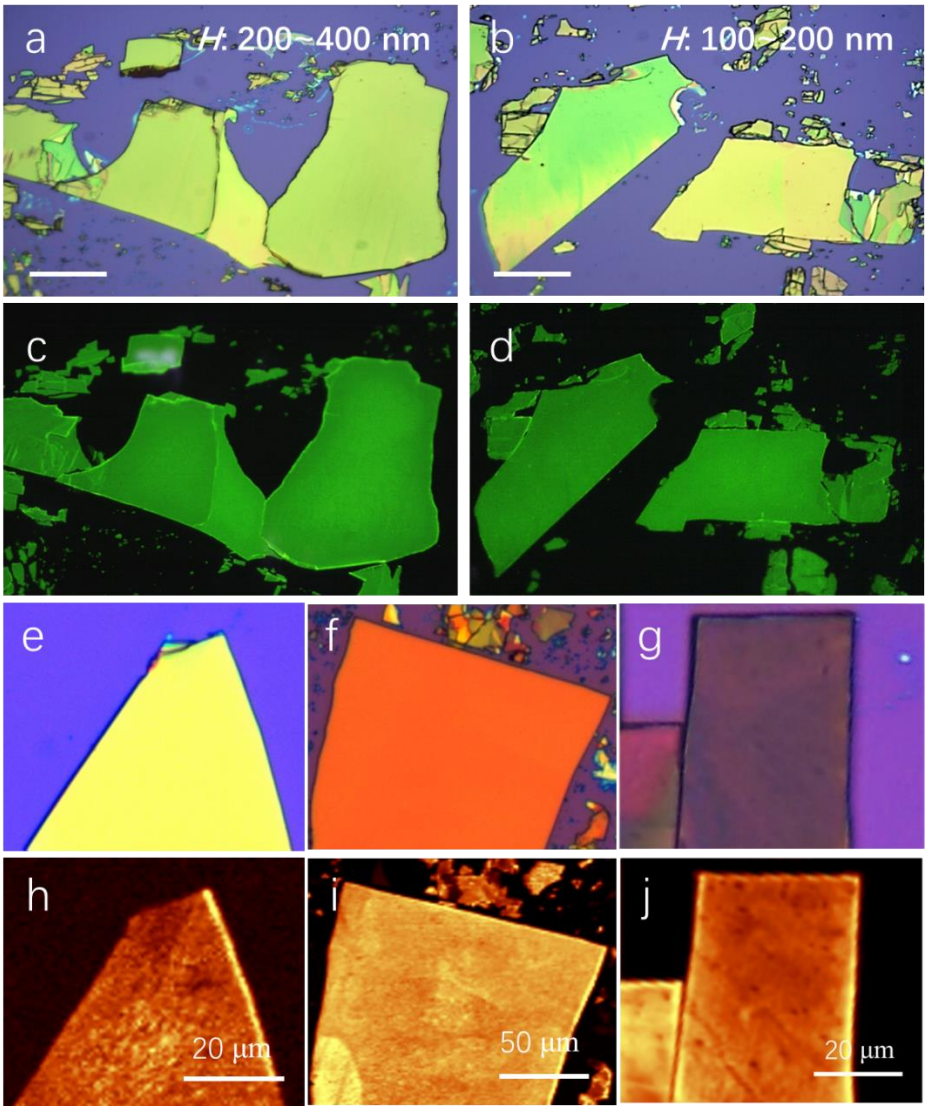

Figure 4.3 Optical images of the RPPs with different thicknesses (*H*). (a) and (b) are bright-field as well as (c) and (d) are PL images of the RPP flakes. Scale bar: 50 μm. The PL images are excited by UV light. Flakes with high quality are observed from the uniform optical quality. Bright-field and PL mapping images of RPPs with n = 1 (e) and (h), n = 2 (f) and (i), as well as n = 3 (g) and (j), respectively. A smooth surface with high-quality RPP flakes can be observed. The PL mapping was excited by a 450 nm continuous wave laser.

4.4 Nonlinear properties of 2D perovskites

Figure 4.4 investigates the PL characteristics of the RPP flake under 800 nm fs pulses excitation at room temperature. **Figure 4.4a** shows the PL peak wavelength of n = 1 RPP flake is ~525 nm (2.36 eV), which energy is larger than one 800 nm photon (1.55 eV), but less than two 800 nm photons (3.1 eV). The insert shows the log-log plot of output intensity versus excitation power density, in which the slope of integrated PL intensity versus excitation power density is ~1.95, indicating that the PL emission of the RPP flake originates from nonlinear TPA. In contrast to TPA, the slope for single-photon emission is close to 1, and corresponding spectra are shown in **Figure 4.5**. Similar results can be observed from the PL spectra of n = 2 (**Figure 4.4b**) and n = 3 (**Figure 4.4c**) RPP flakes, in which the energy of central wavelength is 2.14 eV (580 nm) and 1.99 eV (623 nm), and slope of the fitted line is ~1.92 and ~2.09, respectively. **Figure 4.4d** explains the mechanism of upconversion emission under a TPA process (λ_{ex} = 800 nm) for the RPP flakes. It is expected that the presence of a vacuum level inside the bandgap of the well layer supports upconversion transition. Hence, we confirm that the RPP flakes support upconversion PL emission under two-photon excitation at room temperature.

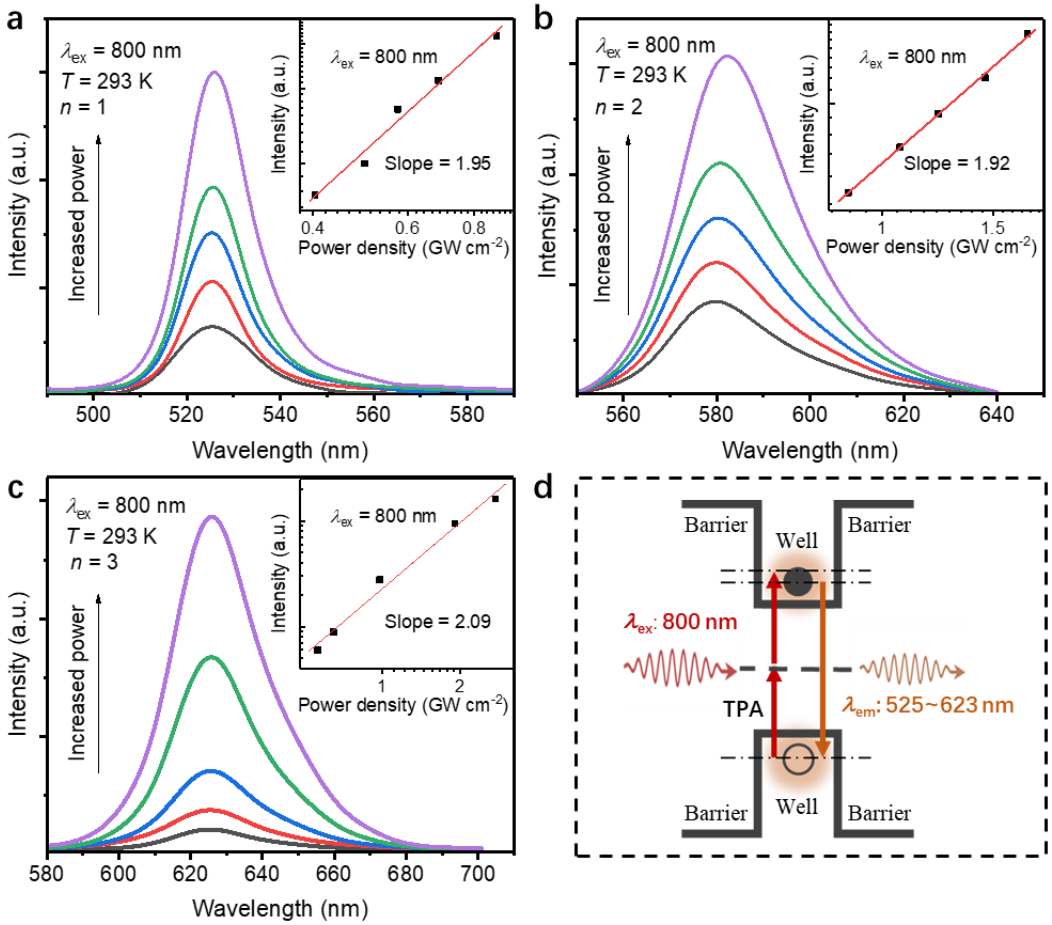

Figure 4.4 Upconversion emission characteristics of single RPP flake on SiO_2/Si substrate under 800 nm fs pulse laser excitation at T = 293 K. PL spectra of the RPP flakes for (a) n = 1, (b) n = 2, and (c) n = 3 under low power density excitation. Inset: Corresponding log−log plot of the integrated PL intensity versus the excitation power density. d) Schematic diagram of the upconversion emission process of RPP flakes under two-photon excitation.

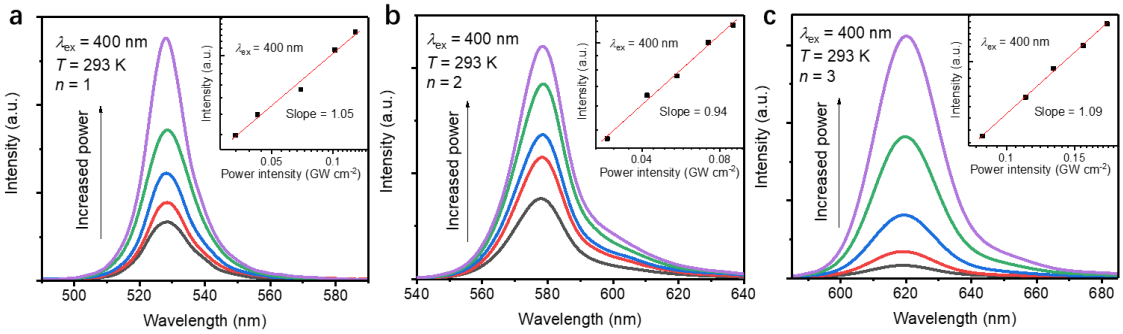

Figure 4.5 Single-photon emission characteristics of RPP flakes on SiO_2/Si substrate under 400 nm fs pulse laser excitation at T = 293 K. PL spectra of the RPP flakes for (a) n = 1, (b) n = 2, and (c) n = 3, respectively under low power density excitation. Inset: log-log plot of the integrated PL intensity versus the excitation power density.

The nonlinear optical properties of the RPP flakes are studied by the open aperture (OA) micro Z-scan technique.[165] The measurement was performed using the same fs pulse laser as the excitation source of the micro Z-scan system. The configuration of the micro Z-scan setup is shown in **Figure 4.6**, and the partially enlarged view with related parameters for the experiment is demonstrated in **Figure 4.7a**. It should be noted that the sizes of the RPP flakes were selected to be larger than 20 μm to cover the diameter of the laser beam over the entire scanning range. The thickness of the RPP flakes was selected to be between 70 and 120 nm. This is to avoid light self-absorption, scattering, and reflection, which generally occur in the bulk perovskite materials, on the influence of the *Z*-scan measurement. In the experiment, only a single flake was used during each measurement. The excitation power density of the fs pulse laser was limited to below the damage threshold of the flake, that is ~34 GW cm^{-2}. **Figure 4.7b** shows the typical

room-temperature OA micro Z-scan results of the RPP flakes with n = 1, 2, and 3 mechanically exfoliated onto a quartz substrate. The influence of quartz substrate (blue hollow circles) on the measurement is negligible because there is nearly no change in its transmission with the variation of z position, and the transmittance from the quartz substrate without RPP flake is given near the top in the **Figure 4.7b**. For the RPP flakes, the transmission (the hollow squares) decreases to a minimum with the sample approaching the location of the beam waist (z = 0).

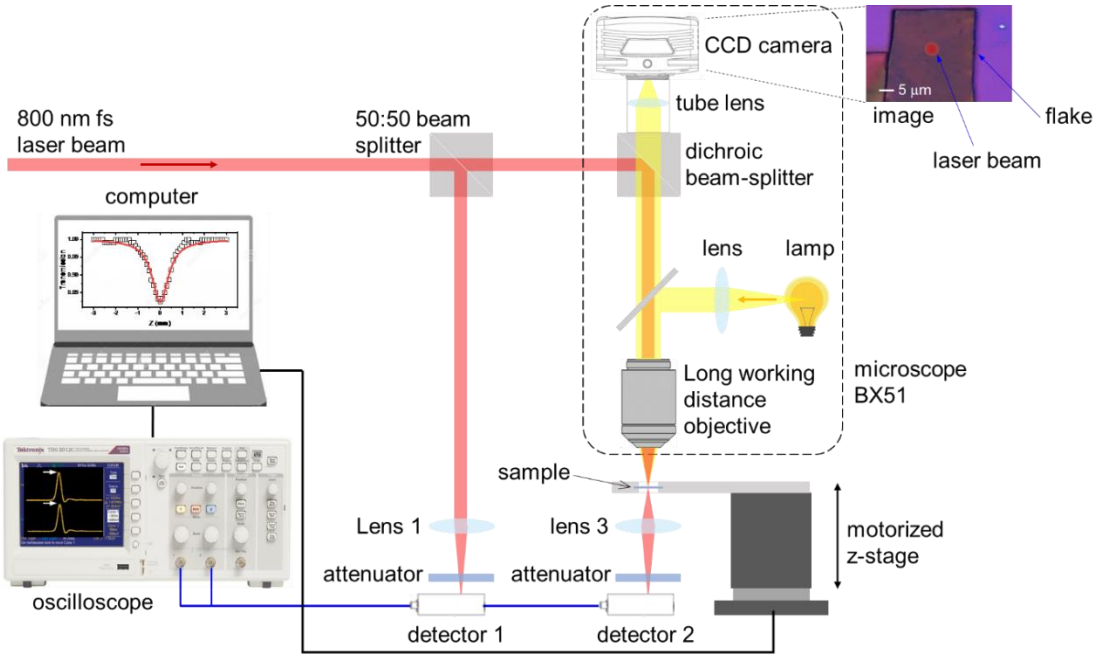

Figure 4.6 Schematic diagram of the micro Z-scan experimental setup for measuring the nonlinear optical characteristics of a single RPP flake with a size larger than 20 × 20 mm^2.

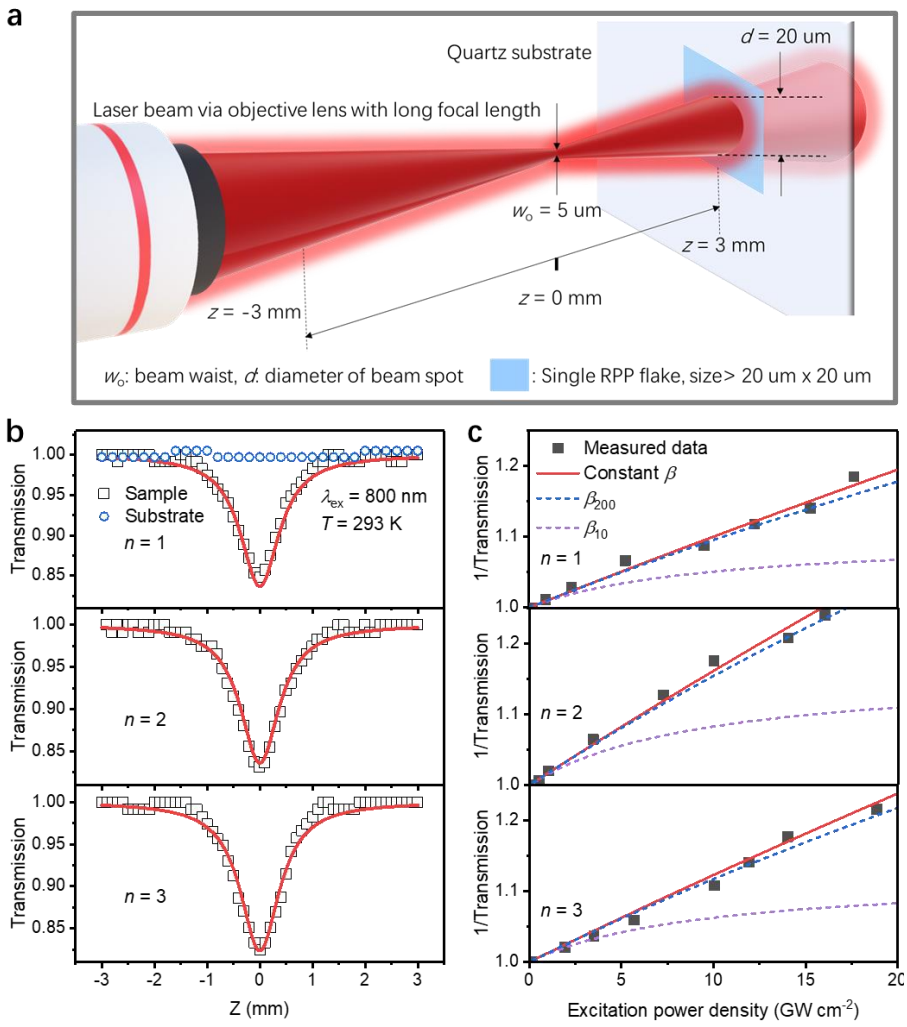

Figure 4.7 Nonlinear optical properties of the RPP flakes. (a) Schematic diagram of partially enlarged micro Z-scan experimental setup for RPP flakes on the quartz substrate. (b) Transmission measurement of the RPP flakes (hollow squares) by using the OA Z-scan method, from top to bottom for n = 1, 2, and 3, respectively at an excitation power density of 15 GW cm^{-2}. The blue hollow circles are the transmission of the quartz excited under the same condition. The red curves are fitting results of the measured data using **Equation (1)** to obtain β. (c) Reciprocal transmission of the RPPs versus excitation power density. Blue (β_{200}) and purple (β_{10}) dashed line: theoretical

variation of reciprocal transmission for a power-dependent β with a saturated excitation power intensity of 200 and 10 GW cm^{-2}, respectively.

To quantitatively determine the TPA coefficient, β, the typical OA Z-scan data were fitted by the normalized power transmission, $T(z)$, as shown below:[165, 166]

$$T(z) = ln(1 + q_o(z))\,/q_o(z) \quad (1)$$

where $q_o(z) = (\beta L_{\text{eff}})I_{\text{o}}/(1 + z^2/{z_{\text{o}}}^2)$, $L_{\text{eff}} = [1 - \exp(-\alpha L)]/\alpha$, α is the linear absorption coefficient, L is the thickness of the sample, I_{o} is the excitation power density, z_{o} represents the Rayleigh range. The red fitted curve with a dip at z = 0 is obtained based on the nonlinear absorption model, which agrees well with our experimental data (hollow squares) plotted in **Figure 4.7b**, and the deduced values of β and other parameters are summarized in **Table 3.1**. It is found that the sample for n = 2 possesses the largest β value of ~3.65×10^3 cm GW^{-1}, while the smallest β value of ~2.15×10^3 cm GW^{-1} is for the n = 1 RPP flake. It is noted that the fitted value of β of the RPP flakes at 800 nm is at least 3 orders of magnitude larger than that of their counterpart 3D perovskites.[86, 167] This can be attributed to the 2D confinement in the QW-like structure leading to a giant exciton effect and the resonance of TPA near the band edge.[146, 168] **Figure 4.7c** plots the inverse of $T(0)$ of the RPP flakes versus excitation power density. The solid squares are the measured data and the red lines are the fitting result using **Equation (1)** with a constant β. The blue and purple dashed lines are obtained by using an I_{o} dependent $\beta(I_{\text{o}}) = \beta/\,(1 + I_{\text{o}}/I_{\text{sat}})$, assuming that the saturation

power density, I_{sat}, is equal to 200 and 10 GW cm^{-2} in the calculation. It is noted that our measured data can be considered power-dependent $\beta(I_o)$ until $I_{sat} \geq 200$ GW cm^{-2}, which is far over the damage threshold of 34 GW cm^{-2}. This indicates that the β of the RPP flakes is non-saturated and is different from the other 2D materials where β is saturated at the operation power.[168] Therefore, the large value of β at the operation power (i.e., non-saturation) contributes to the increase of upconversion transition efficiency so that two-photon excitation-emission is observed from the RPP flakes at room temperature.

Table 4.1. Linear and nonlinear parameters of the RPP flakes with n = 1, 2, and 3.

	α (cm^{-1})	Thickness (nm)	z_o (mm)	β (cm GW^{-1})
$n = 1$	7.87×10^3	~80	0.4	2.15×10^3
$n = 2$	1.47×10^4	~70	0.4	3.65×10^3
$n = 3$	3.30×10^4	~120	0.4	3.00×10^3

4.5 Characteristics of 2D perovskite lasing

Next, we analyze the lasing characteristics of the RPP flakes under two-photon (λ_{ex} = 800 nm) excitation. In the experiment, the shape of the RPP flakes was selected to have at least two parallel facets and the thickness of the flakes was around 100 to 400 nm. We found that the RPP flakes with n = 1 do not support lasing emission, but the RPP

flakes with n = 2 and 3 demonstrate lasing emission under two-photon excitation at low temperatures. **Figure 4.8a** plots the emission characteristics of the RPP flake with n = 2 at 78 K under 800 nm fs laser excitation. It is noted that for excitation power density above 1.2 GW cm^{-2}, sharp peaks with FWHM of ~0.9 nm generate at wavelengths near 598 nm from the broad PL spectrum. It is also observed that lasing light is scattered mainly from the two parallel facets with a wider separation of the RPP flake, and their mode spacing is ~2.1 nm, see insert photos of **Figure 4.8a**. **Figure 4.8b** plots the corresponding light-light curve and the FWHM of the emission peak. It is clearly shown that there is a transition from spontaneous emission to lasing emission at ~1.2 GW cm^{-2}. This is because there are 1) a sudden increase of emission intensity and 2) a sudden narrowing of emission peak linewidth from ~25 to ~0.9 nm at the threshold I_{th} = 1.2 GW cm^{-2}. These verify that the flake with n = 2 supports lasing emission via two-photon excitation at low temperature.

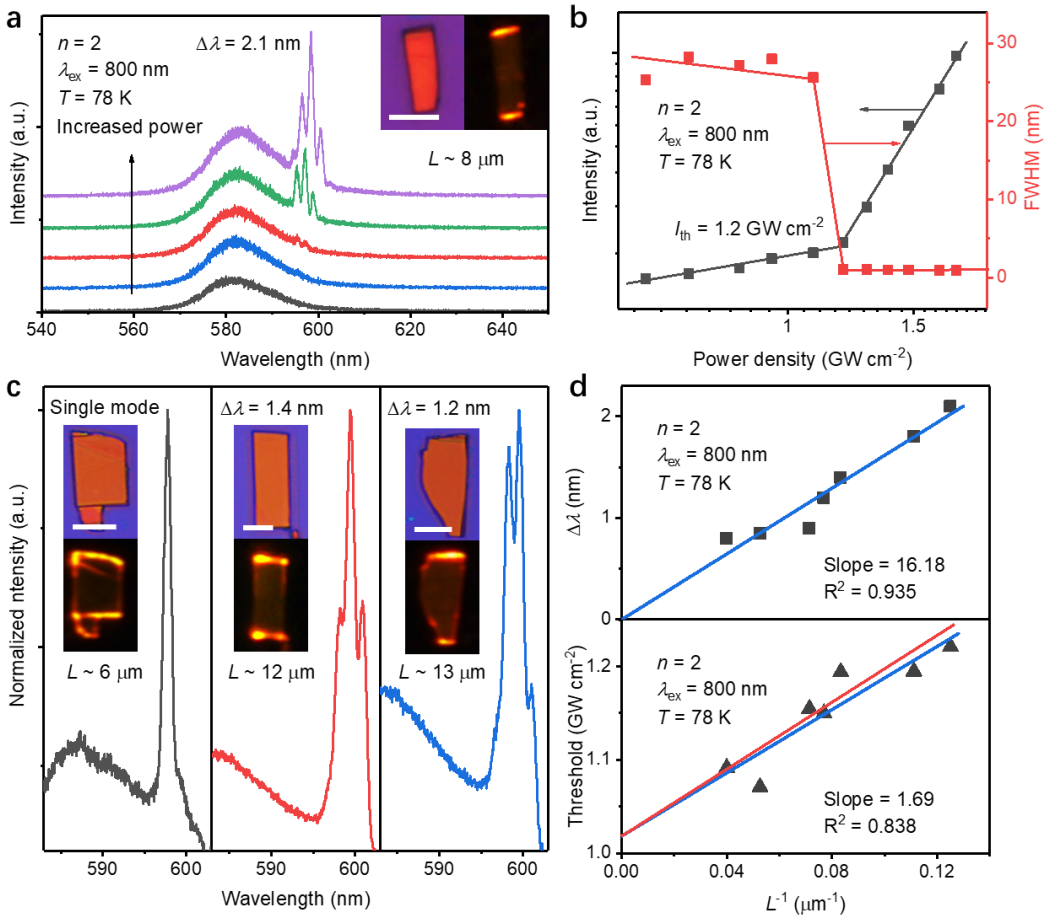

Figure 4.8 Low-temperature (78 K) lasing characteristics of RPP (n = 2) flakes with different cavity lengths, L. (a) Lasing characteristics under various power density excitation. Inset: optical image of an RPP flake (top) without and (bottom) with optical excitation above the threshold. Scale bar: 5 μm. (b) A plot of emission intensity and FWHM of the emission peak versus excitation power density. (c) Lasing spectra of the flakes with different L. Inset: the optical images (top) and corresponding lasing emission images (bottom). Scale bar: 5 μm. (d) A plot of mode spacing (top panel) and excitation threshold (bottom panel) as a function of L^{-1}. The solid and triangle squares are the measured data, which are fitted by the blue lines. The red line in the bottom

panel is the plot of Equation (3) with L^{-2} term using the deduced values of k_1, k_2, I_1, and S_1 (see supplementary information).

Lasing mechanism of the RPP flakes with n = 2 operating at 78 K can be clarified by studying their dependence on the cavity length L (i.e., the distance between two parallel facets with a wider separation). Here, we repeated the above measurement using RPP flakes with different L. **Figure 4.8c** shows the lasing spectra of the RPP flakes for L varies from 6 to 13 μm under 800 nm fs pulse laser excitation at 78 K, and the insets show the corresponding photos of the flakes without (top) and with (bottom) optical excitation above the threshold. It is noted that lasing light is scattered from the two parallel facets with a wider separation and a similar characteristic is also observed in **Figure 4.8a**. This is expected as longer L can provide less cavity loss. Therefore, it is believed that the flakes naturally form an FP microcavity and optical feedback is achieved between the two parallel facets. We can use the mode spacing $\Delta\lambda$ of the lasing modes and cavity length L to revive the effective refractive index of the RPP flakes using the following equation for FP lasers:

$$\Delta\lambda = \lambda_o^2/2n_{\text{eff}}L \quad (2)$$

where λ_o (~ 598 nm for n = 2) is the emission peak wavelength, $n_{\text{eff}} = n_{\text{bulk}} - \lambda_o \partial n_{\text{bulk}}/\partial\lambda_o$,[169] n_{bulk} is the bulk refractive index, and $\partial n_{\text{bulk}}/\partial\lambda_o$ is the material dispersion. The measured $\Delta\lambda$ versus the corresponding L^{-1} from **Figures 4.8a and 4.8c** was plotted with solid squares in the top panel of **Figure 4.8d**, and the blue line is

obtained by linear fitting of these data. The blue fitted curve well predicts that $\Delta\lambda = 0$ at $L^{-1} = 0$, and this result is aligned with **Equation (2)**. This is because if L is very large, it is not able to distinguish the spectral separation between two adjacent longitudinal modes. Hence, it is verified that all the RPP flakes with two parallel facets support FP modes. Furthermore, it is noted that the slope of the fitted curve is 16.18 (nm μm^{-1}), and this implies that the value of n_{eff} is 10.87. This value is higher than its bulk value (n_{bulk} ~ 2.2 - 3.7) because of the strong optical confinement inside the transverse direction of the flakes, which indicates strong material dispersion similar to that observed in nanowire lasers.[170]

As the flakes support lasing emission of FP modes, the excitation threshold I_{th} can also be proportional to:[171]

$$I_{th} \propto k_2 I_1 \left(\frac{k_1}{k_2} + I_1\right) + k_2 S_1 \left(\frac{k_1}{k_2} + 2I_1\right)\frac{1}{L} + k_2 S_1^2 \frac{1}{L^2} \quad (3)$$

where $I_1 = N_o + \alpha_o/\Gamma a_N$, $S_1 = (2\Gamma a_N)^{-1}\ln(1/R_1R_2)$, a_N is the differential gain coefficient of the flakes, Γ is the optical confinement factor, N_o is the carrier concentration at transparency, α_o is the material loss, R_1 and R_2 are the reflectivities of the two parallel facets of the RPP flakes. In **Equation (3)**, k_1 and k_2 are radiative and biexciton Auger recombination rates respectively.[172] As noticed from Equation (3), if the differential gain overcomes the influence of biexciton Auger recombination of the RPP flakes to support lasing, I_{th} should be proportional to L^{-1} and the third term on the right-hand side of Equation (3) can be ignored in the consideration. Hence, we plot the measured

excitation threshold I_{th} of the RPP flakes versus L^{-1}, see the solid triangles in the bottom panel of **Figure 4.8d**. We also fit the measured data with a blue straight line which is well fitted to the data points. Furthermore, we investigated the lasing characteristics of the RPP flakes with n = 3 under 800 fs pulse laser excitation at 78 K (see **Figure 4.9**). It is verified the flakes also support FP lasing emission at 78 K under two-photon excitation. The corresponding n_{eff} is found to be 11.35 slightly higher than that of case n = 2. For the fitting results of I_{th} versus L^{-1}, it is noted that the RPP flakes with n = 2 and 3 have a large coefficient of determination, R^2, equal to ~0.838 and ~0.912, respectively. This implies that the measured data have a strong correlation between the I_{th} and L^{-1}.

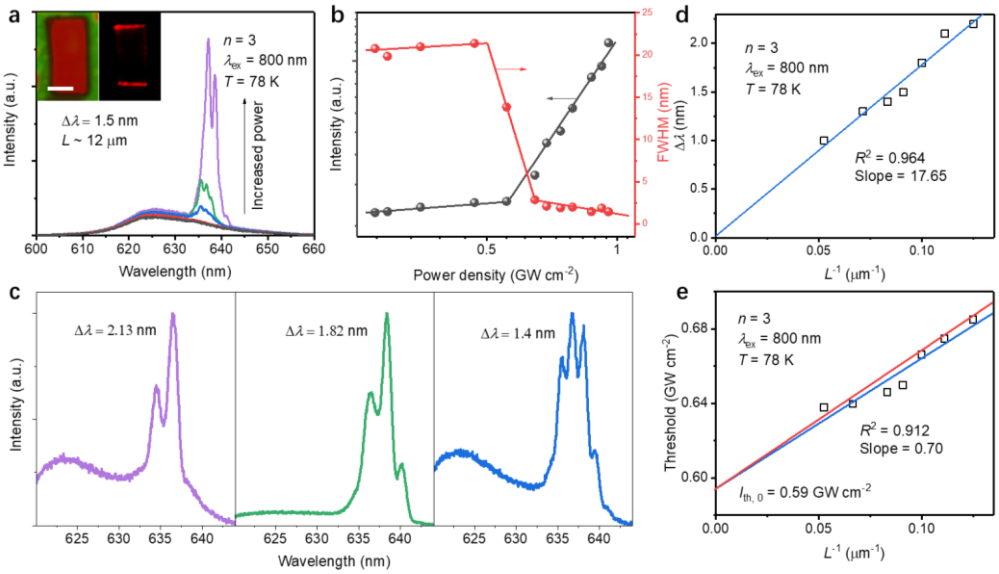

Figure 4.9 Upconversion lasing characteristics of an RPP (n = 3) flake on SiO_2/Si substrate under 800 nm fs pulse laser excitation at T = 78 K. (a) Lasing characteristics under various power densities. Inset: optical image of an n = 3 RPP flake (left) without

and (right) with optical excitation above the threshold. Scale bar: 5 μm. (b) A plot of emission intensity and FWHM of the emission peak versus excitation power density. (c) Lasing characteristics of the RPP flakes with different cavity lengths, L. Plot of (d) mode spacing, and (e) excitation threshold as a function of L^{-1}. The black hollow squares are the measured data which is fitted by a blue line. The red line is the plot of Equation (S8) with L^{-2} term using the deduced values of k_1, k_2, I_1, and S_1.

4.6 Mechanism of 2D perovskite lasing

To verify that the influence of biexciton Auger recombination is suppressed by the differential gain of the RPP flakes with n = 2 and 3, we need to estimate the values of k_1 and k_2 in **Equation (3)**. Here, we perform transient absorption spectrum measurement of the RPP flakes with n = 1, 2, and 3 using λ_{ex} = 400 nm as the pump pulses (see **Figures 4.10**), and the values of k_1 and k_2 for the RPP flakes with n = 1, 2, and 3 are given in **Table 4.2**. Due to the limitation of our equipment, the experiment was performed at room temperature. Nevertheless, k_2 decreases with the decrease of temperature so that the deduced value of k_2 will not underestimate the influence of biexciton Auger recombination on the laser threshold.[173, 174] Hence, using the above information, we can calculate the values of I_1 and S_1 for the cases n = 2 and 3, and the results are given in **Table 4.3**.

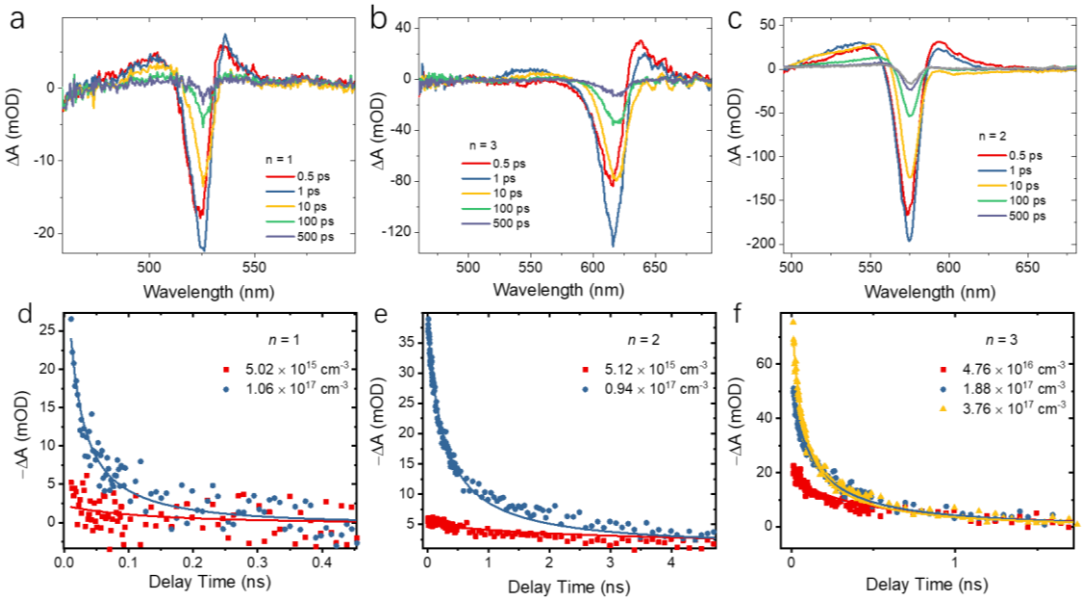

Figure 4.10 TA spectra of the RPP flakes with n = 1 (a), 2 (b), and 3 (c). The flakes under room temperature excitation by pump- (400 nm 50 fs 1 kHz) and probe- (continuum white-light 50 fs 1 kHz) pulses with different time-delay (0.5 to 500 ps). Pump and probe excitation intensities are maintained the same in the experiment for the cases of n = 1, 2, and 3. A single PB peak, which locates at 526, 574, and 616 nm for n = 1, 2, and 3 respectively, is observed from the RPPs. The kinetics at PB peak of the RPP flakes with n = 1 (d), 2 (e), and 3 (f) under different pump power at room temperature. The solid lines are the fitted curves with the measured data. In the experiment, two or three values of pump power with a wavelength of 400 nm are used to measure the change of decay response of the excitons. The power of the continuum white-light probe is kept unchanged in the experiment.

Table 4.2. Exciton radiative and biexciton Auger recombination rates of RPP flakes with n = 1, 2, and 3.

	k_1 (s^{-1})	k_2 ($cm^3\ s^{-1}$)	k_1/k_2 (cm^{-3})
n = 1	5.16×10^9	6.31×10^{-7}	0.82×10^{16}
n = 2	4.52×10^8	4.64×10^{-8}	0.97×10^{16}
n = 3	6.28×10^8	9.42×10^{-9}	6.67×10^{16}

Table 4.3 Parameters used for calculation of I_{th} by Equation (3) for PRR flakes with n = 2 and 3.

	y-intercept ($W\ cm^{-2}$)	Slope ($W\ cm^{-1}$)	I_1 (cm^{-3})	S_1 (cm^{-2})	$\kappa k_2 S_1^2$ (W)	Γa_N (cm^2)	a_N (cm^2)
n = 2	1.02×10^9	1.69×10^5	0.88×10^{18}	7.32×10^{13}	7.0	0.16×10^{-13}	0.18×10^{-13}
n = 3	0.59×10^9	0.7×10^5	1.46×10^{18}	8.84×10^{13}	2.1	0.13×10^{-13}	0.14×10^{-13}

We plot **Equation (3)** for the RPP flakes with n = 2 and n = 3 in **Figure 4.8d** and **Figure 4.9e** respectively, with the influence of L^{-2} term taken into the calculation (i.e., the red fitting curves). It is noted that the red fitting curve only slightly deviates from the blue straight line for L^{-1} is large. At low temperatures, the value of k_2 will be further reduced from its room temperature value so that the fitting results will remain unchanged. This indicates that the influence of biexciton Auger recombination (i.e., coefficient of L^{-2} term is small) is insignificant for these cases especially for n = 3 as it has a higher R^2 value, and our assumption to ignore L^{-2} term is acceptable. Therefore, we can conclude

the influence of biexciton Auger recombination for the RPP flakes with n = 2 and 3 is overwhelmed by its differential gain. On the other hand, it is noted from **Table 4.3** that the estimated value of a_N for the case n = 2 is slightly higher than that of n = 3. This is not surprised as the differential gain of QW structure of RPP flakes with narrow QW thickness can be strongly enhanced by the excitonic effects.[175] However, although RPP with n = 2 flakes have higher differential gain, its non-radiative Auger recombination rate is also high (i.e. k_2 of n = 2 case is 10 times higher than that of n = 3 case) due to the confinement effect so that the resultant performance is not better than that of the RPP with n = 3 flakes. Nevertheless, RPP with n = 2 flakes still have an optical gain higher enough to overcome its non-radiative recombination loss so that lasing is supported from the sample. For RPP with n = 3 flakes, lasing emission is supported because the influence of non-radiative Auger recombination is significantly suppressed due to their relatively wider QW structure compared to the n = 2 case.

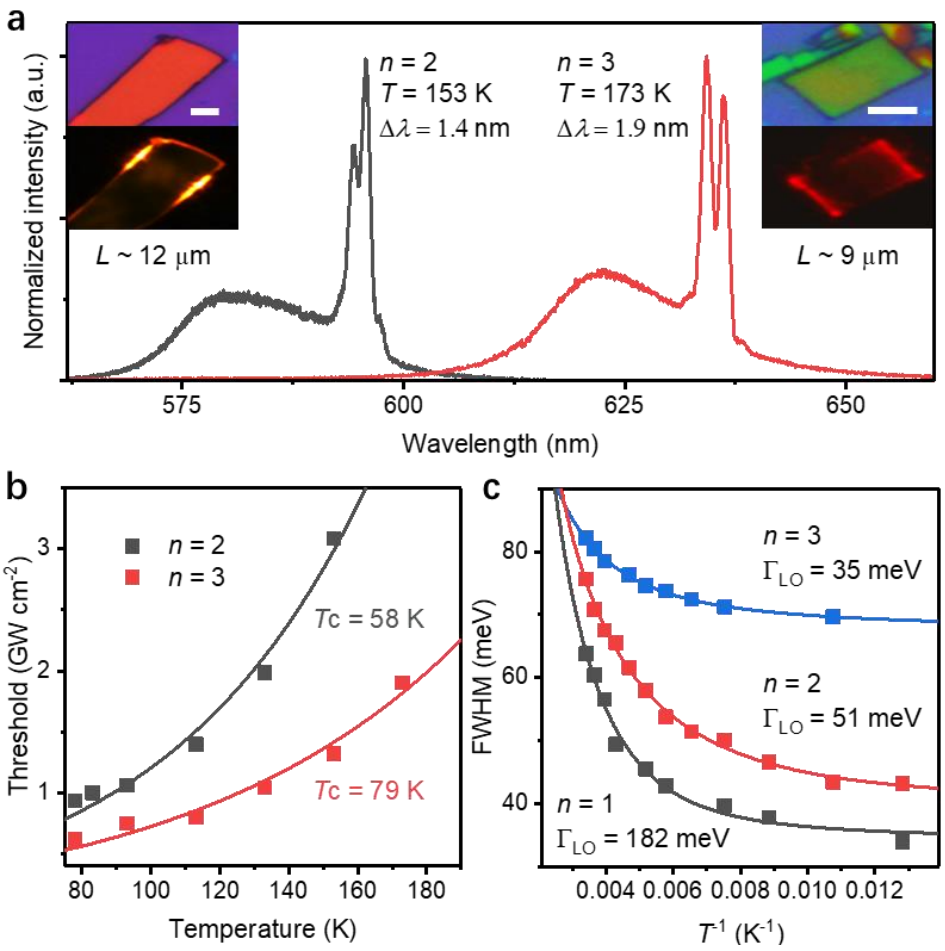

Figure 4.11 Multiple-color lasing characteristics of RPP flakes at various temperatures under 800 nm fs laser excitation. (a) lasing spectra of RPP flakes for n = 2 (left) and n = 3 (right) at 153 and 173 K, respectively. Inset: the corresponding optical and lasing images. Scale bar: 5 μm. (b) Lasing threshold as a function of temperature for n = 2 (black) and n = 3 (red) RPP flakes, in which the cavity length is about 11 and 10 μm, respectively. The measured data (solid squares) are well fitted by Equation (3), and the characteristic temperatures (Tc) are 58 and 79 K, for n = 2 and n = 3 RPP flakes, respectively. (c) The FWHM of spontaneous emission versus the inverse of temperature, T^{-1}, for the RPPs flakes with n = 1, 2, and 3. The coupling strength of exciton-LO

phonons, Γ_{LO}, is found to be 182, 51, and 35 meV for n = 1, 2, and 3 RPP flakes, respectively.

Figure 4.11a shows the upconversion lasing characteristics of RPP flakes with n = 2 and n = 3 operating at T = 153 and 173 K respectively**.** The corresponding temperature-dependent threshold, $I_{th}(T)$, of the RPP flakes is also plotted in **Figure 4.11b**, and it is found that the lasing threshold increases with the increased temperatures, due to the strong optical loss from enhanced electron-phonon interaction.[176] The characteristics temperature, T_c, of the RPP flakes can be deduced by fitting the measured data of $I_{th}(T)$ with $I_{th}(T) = I_{th,0}\exp(T/T_c - 1)$, where $I_{th,0}$ represents the lasing threshold at T_c. It is found that T_c of RPP flakes with n =2 and 3 are equal to 58 and 79 K respectively. This indicates that the presence of multiple QW-like structures in RPP flakes can capture and stabilize the external injection of carriers that favor the realization of laser diodes [177].

Excess optical loss can be induced by the non-radiative biexciton Auger recombination process, which generates hot carriers that thermally relax through the coupling of longitudinal optical (LO) phonons in the polar semiconductors.[178] The influence of biexciton Auger recombination on the laser threshold can also be studied indirectly through the understanding of the corresponding electron-longitudinal optical phonon coupling strength, Γ_{LO}, which is a temperature-independent linewidth parameter of the RPP flakes, hence, the large value of Γ_{LO} implies an increase of k_2. The linewidth of the

emission peak can be affected by the exciton-phonon coupling, so the values of Γ_{LO} for the RPP flakes can be estimated by plotting the temperature-dependent PL spectra (**Figure 4.12,** Supporting Information) . With the temperature increase, the linewidth becomes broader due to the increasing phonon scattering. In **Figure 4.11c**, the experimental FWHM (Γ_{el}) was used to determine Γ_{LO} by the following equation:[178]

$$\Gamma_{\mathrm{el}} = \Gamma_{\mathrm{inh}} + \gamma_{\mathrm{LA}} T + \frac{\Gamma_{\mathrm{LO}}}{exp(E_{\mathrm{LO}}/k_B T) - 1} \quad (4)$$

where Γ_{inh} is the inhomogeneous broadening factor, γ_{LA} is the exciton-longitudinal acoustic phonon coupling strength, and E_{LO}, which is assumed to be independent of T, is the phonon energy. The results show that Γ_{LO} is 182, 51, and 35 meV for the case n = 1, 2, and 3 respectively. It is noted that Γ_{LO} of the case n = 1 is noticeably larger than that of those for the cases n = 2 and 3 by more than 3 times but the change of Γ_{LO} from n = 2 to 3 is just ~30%. This indicates that the influence of biexciton Auger recombination is significant for the case n = 1, hindering it to realize lasing. These results are consistent with our above findings in the deduction of k_2. Hence, it is expected that upconversion lasing should also be observed from RPP flakes with $n \geq 2$ as the influence of biexciton Auger recombination is significantly suppressed due to the reduction of quantum confinement.

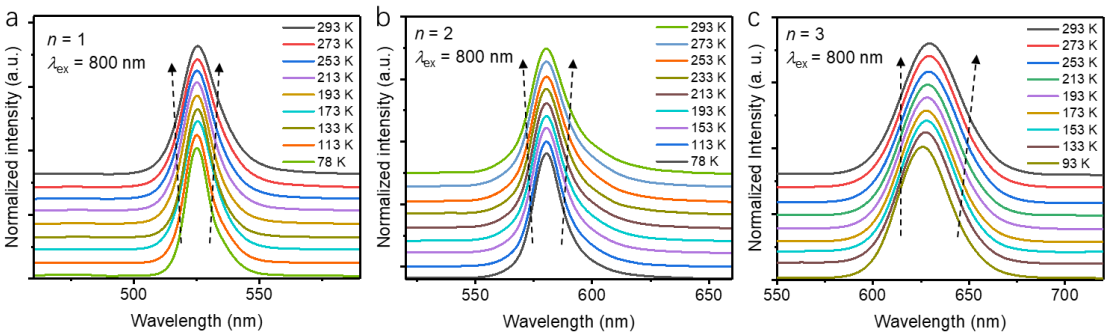

Figure 4.12 Temperature-dependent PL spectra of RPP flakes for (a) n = 1, (b) n = 2 and (c) n = 3 respectively. The results show that the FWHM increases with the increased temperature.

4.7 Conclusions

In conclusion, upconversion lasing emission is observed from the RPP flakes mechanically exfoliated from their high-quality bulk crystals. It is noted that the RPP flakes with $n \geq 2$ support lasing under two-photon excitation (λ_{ex} = 800 nm) at low temperature ($T \leq 153$ K). The mechanism of upconversion lasing from the RPP flakes can be attributed to 1) high-efficiency upconversion transitions under TPA, 2) high differential gain to overcome the biexciton Auger recombination losses inside the laser microcavities, and 3) small electron-phonon coupling strength reduces non-radiative recombination. The RPP flakes exhibit giant optical nonlinearities with a non-saturated two-photon absorption coefficient, β, from 2.15 to 3.65 × 10^3 cm GW^{-1} which is at least 3 orders of magnitude higher than their bulk perovskite counterpart. The threshold model of FP microcavity lasers has also verified that the high differential gain and low

non-radiative biexciton Auger recombination (i.e., $\kappa k_2 S_1^2/L^2 \ll I_{th}$) are the reasons for the support of FP lasing from the RPP flakes with $n \geq 2$. Furthermore, RPP flakes with $n \geq 2$ demonstrate small electron-phonon coupling strength that can reduce the non-radiative recombination. On the other hand, the RPP flakes with $n = 1$ do not support lasing, due to the increase in biexcitonic Auger recombination loss arising from the strong quantum confinement. In addition, the high exciton-phonon coupling inside the RPP flakes with $n = 1$ is indirect evidence of the increase of biexciton Auger recombination arising from the quantum confinement effect. Nevertheless, we do observe that the QW-like structured 2D RPP with $n = 2$ (i.e., with strong quantum confinement of excitons) has a higher differential gain coefficient than that with thicker well width ($n \geq 3$). These studies have revealed that the QW-like structure may favor the capture of external carrier injection as that of the semiconductor QWs used to achieve room-temperature laser diodes. Hence, our investigations may inspire the use of 2D RPP flakes to realize electrically pumped lasers.

Chapter 5 Red upconversion lasing from stable three-dimensional perovskite embedded glasses with the assistance of anion modulation*

5.1 Introduction

Perovskite materials have been developing prosperously in various fields in recent years because of their remarkable properties and are especially attracting increasing attention for use in a variety of optical devices. Compared with traditional optical nanocrystals (NCs), perovskite NCs have the advantages of a simpler preparation process, wider wavelength coverage, higher absorption coefficient, and lower lasing threshold.[7] It is important to note that the exploration of red-emitting perovskite materials is eagerly awaited given the urgent demand for red light in high-definition (HD) displays, infrared detection, and biological imaging. However, it is hard for perovskite materials to overcome the "red gap" to achieve lasing at long wavelengths, owing to inherent structural instability.[179] For example, it was reported that cubic $CsPbI_3$ only could maintain stability above ~ 300 °C, otherwise an undesirable phase transition can occur from the cubic phase to the orthorhombic phase at room temperature. The red-emitting

* Presented in the publication entitled "The achievement of red upconversion lasing for highly stable perovskite nanocrystal glasses with the assistance of anion modulation. Nano Research, 2021. 221, 2861-2866. https://doi.org/10.1007/s12274-021-3364-5"

organic perovskite also faces the same dilemma; Zhong et al. unveiled the puzzle underlying the tendency for $MAPbI_3$ to decompose, pointing to the interplay of the precursor solution and solvent in the process of crystallization. Moreover, it is worth noting that the previously reported hygroscopicity of MA^+ and FA^+ makes $MAPbI_3$ and $FAPbI_3$ highly susceptible to water effects.[180] On the other hand, even if perovskite NCs with stable red emission in the atmospheric environment are obtained, it is tricky to avoid phase separation under intense laser irradiation.[181]

Focusing on the above issues, the main current solutions are described as follows. The first common method involves the partial substitution of I^- with Br^- to obtain a stable red-emitting perovskite phase.[182] The optical performance of mixed halogen perovskite NCs are much better than APbI3 ($A = MA^+, FA^+, Cs^+$) [20]. Another effective method is based on the design of an inert matrix encapsulation to isolate the influence of the external environment on NCs.[183] The coating matrices can be generalized as oleylammonium carboxylate, silica/modified silica microspheres, and thin films. The above strategies can improve the stability of red-emitting perovskite NCs at room temperature to some extent. However, as for lasing applications, the phase separation of mixed halogen perovskite is prone to generate bromine-rich and iodide-rich regions under intense laser irradiation. Although coating can significantly enhance the laser stability, the accompanying defects can decrease the optical properties, such as the optical gain value, which can then seriously affect the laser performance.[184] Thus, it

is important to propose an effective method that combines the stability and optical properties of perovskites, which can broaden perovskite applications in photonic devices.

It has been reported that perovskite NCs glass (PNG) is an attractive optical gain material, which meets strict requirements for the oxygen stability, thermal stability, and water stability of materials.[185] In addition, unlike other materials, perovskite NCs show an irreversible phase in a glass network; the glass network can inhibit the phase separation. At present, there are no reports for the achievement of lasing in the red region for PNG. Hence, in this work, a stable $CsPbI_3$ NCs glass was prepared by in situ crystallization, and a series of $CsPb(Br/I)_3$ NCs glasses with better optical performance were obtained via the design of the Br/I ratio. The introduction of bromine ions to $CsPbI_3$ can alleviate structural instability and improve the quantum yield to a certain extent.[186] The lasing action for these glasses was investigated by using 800 nm pulse laser excitation at low temperature. Pulse excitation is a very advantageous excitation mechanism compared with CW pumped because carrier densities required for lasing threshold can be readily injected, preventing the damage to samples caused by a large amount of heat during operation.[187] And the building up of nonequilibrium carrier distributions shows no competition with radiative recombination processes within the first nanoseconds.[172] The optical gain coefficients and the lasing thresholds for PNG were explored, as well as the relationship between the quantum efficiency (QE).

Moreover, PNG can still achieve random lasing after being immersed in water for a week, indicating robust stability in water. These results imply that PNG holds great potential for application in HD displays and photonic devices.

5.2 Experimental methods and instrument

5.2.1 Chemical materials

B_2O_3 (99.9%), NaX (X = Br, I) (99.9%), SiO_2 (99.9%); ZnO (99%), PbX_2 (X = Br, I) (99%), Cs_2CO_3 (99%), Al_2O_3 (99.99%) and MgO (99.99%) were purchased from Aladdin and directly used without further purification.

5.2.1 Fabrication Methods

The $CsPb(Br/I)_3$ NCs glasses were synthesized through the conventional melt-quenching technique and glass crystallization method. In addition, perovskite-related chemicals (Cs_2CO_3– PbX_2–NaX, (X = Br, I)) were proportionately added with the ratio of 1:2:2, which were embedded into the glassy matrix with a molar ratio of 34SiO2–$4Al_2O_3$–5MgO–11ZnO–$46B_2O_3$. In detail, the weighed chemicals were carefully ground and poured into a corundum crucible, and then the obtained mixed powder was melted in a muffle furnace at 1,200 °C for 10 min. Next, the melted mixture was quickly poured into a preheated iron plate and quickly transferred to the preheated muffle

furnace for an extended period for heat preservation and stress relief to form the as-prepared glasses. The as-prepared glasses were then cut into pieces with a thickness of 0.8 mm. For the heat treatment, considering that the diffusion of heavy ions in the glass matrix requires great activation energy, we chose the highest temperature that the sample could withstand, with all samples heated at 530 °C for 10 h. Finally, $CsPbBr_{1.5}I_{1.5}$ (BIA), $CsPbBr_1I_2$ (BIB), and $CsPbI_3$ (BIC) NCs glasses were prepared by changing the molar ratio of Br and I.

5.2.3 Instrument for material characterizations

The structure was characterized using X-ray diffraction (XRD, Germany D8 Advance) with Cu Kα radiation operating at 40 kV and 40 mA, and transmission electron microscopy (TEM, JEM-2100F) carried out using an FEI Tecnai G2 F20 S-TWIN with an acceleration voltage of 200 kV. The distribution of elements was analyzed by TEM with an energy dispersive spectrometer system (EDS) and X-ray photoelectron spectroscopy (XPS). Downconversion fluorescence was explored by using a spectrophotometer (Horiba Jobin Yvon Fluromax-4P) and UV–Vis spectrometer (Perkin Elmer Lambda 750). The quantum efficiency was measured by a spectrophotometer with an integrating sphere (Otsuka QE-2100, Japan).

5.2.4 Measurement of optical gain

The optical gain coefficients were measured by the variable stripe length (VSL) method. The 800 nm fs pulsed laser was focused by a cylindrical lens to a line on the sample surface, which was measured at room temperature. An adjustable slit was placed between the cylindrical lens and the sample surface to accurately modulate the length of the stripe. By changing the length of the strips on the sample surface, the corresponding emission from the edge of the sample was collected by an optical fiber (diameter of 600 μm). The optical fiber was coupled to a spectrometer (Ocean Optics USB 2000 + VIS-NIR).

5.2.5 Measurement of lasing performance

Random lasing properties were studied by using an 800 nm 1 kHz femtosecond (fs) pulsed laser (Ti: sapphire laser (coherent Libra) equipped with an optical parametric amplifier (Coherent OperA Solo)). A laser beam with an 8 mm diameter was focused onto the surface of the sample by a convex lens with a focal length of 10 cm, which was located inside a low-temperature chamber (Linkam DSC 600 temperature-controlled stage) purged with N2 gas. In this experiment, an 800 nm fs laser was used as the light source and the test temperature was 78 K. The emission from the sample surface was recorded by an optical fiber (diameter of 600 μm). The optical fiber was

coupled to a monochromator (Princeton Spectra Pro 2750 integrated with a Pro EM EMCCD camera with a spectral resolution of less than 0.1 nm) for spectral analysis.

5.3 Characteristics of 3D perovskites

Photographs of BIA, BIB, and BIC under daylight and ultraviolet (UV) light are shown in **Figure 5.1a**, proving that the emission wavelength can be regulated by adjusting the halogen ratio. The structural characterization and linear optical properties of the NCs glasses were investigated in depth. As shown in **Figure 5.1b**, the XRD patterns confirm the amorphous structure of PNG, and the diffraction peaks for BIC can be well matched to the standard diffraction card of Cubic $CsPbI_3$. Obviously, with the introduction of Br^-, the diffraction peaks due to NCs glass move towards a larger angle, which is akin to that found in a colloidal NCs solution.[76] In addition, at the same heat-treatment condition, better crystallization is found to accompany the higher ratio of Br^-. The PL spectra measured for BIA, BIB, and BIC are shown in **Figure 5.1c**. The fluorescence peaks show a significant redshift due to the increasing proportion of iodine, further proving that the emission wavelength can be managed by halogen regulation, which is consistent with the results shown in **Figure 5.1a**. In addition, as shown in **Figure 5.1d**, the absorption peaks exhibit a blueshift relative to the emission peaks on account of the Stokes shift. **Figure 5.1e** demonstrates that as the proportion of iodine increases, the band gap is reduced from 2.15 to 1.80 eV. As shown in **Figure 5.1f**, the QE was also

explored, which represents the number ratio between the emitted photons and the absorbed excitation photons. By doping Br ions into BIC samples, the QE for the perovskite can be obviously improved.

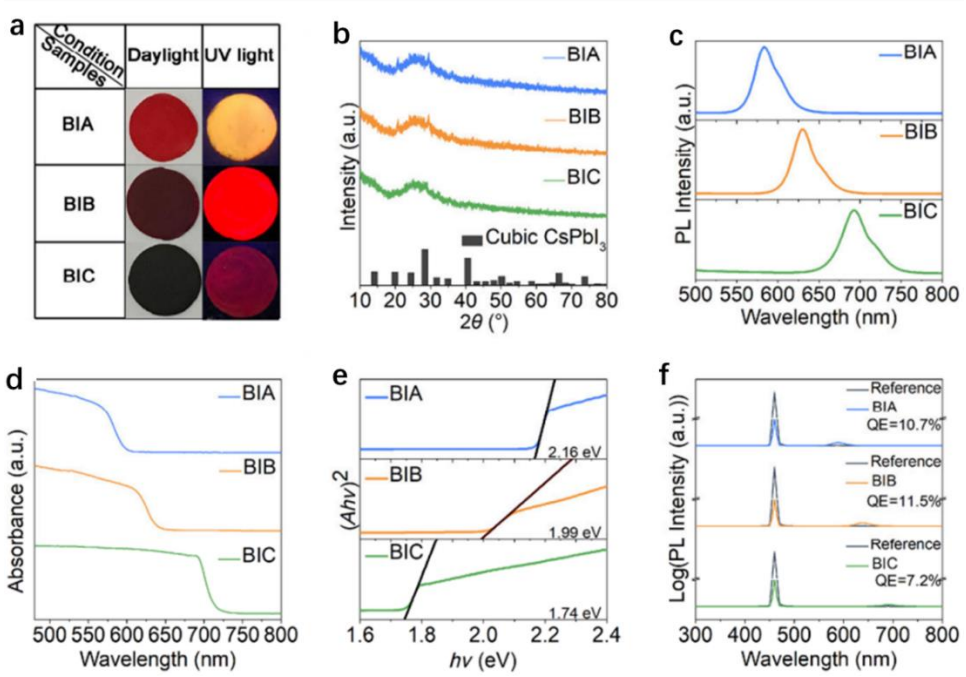

Figure 5.1 Characteristics of perovskite glasses. (a) Photographs of BIA, BIB, and BIC under daylight and an ultraviolet lamp. (b) XRD patterns, (c) PL emission spectra and (d) UV–Vis absorption spectra, and (e) the spectra plotted as $(Ahν)^2$–(hν) for BIA, BIB, and BIC, respectively. (f) Quantitative PL spectra for all the samples and the reference used for the determination of QE. The spectra were recorded by using a spectrofluorometer equipped with an integrating sphere.

TEM images confirm that the spherical BIA, BIB, and BIC NCs are evenly dispersed in the glass matrix, as shown in **Figure 5.2a–5.2c**. The high-resolution TEM (HRTEM)

images are shown in the interior illustrations, which show high crystallinity. A distinct lattice spacing for the (002) plane in BIC is observed (3.02 Å), and this lattice spacing decreases to 2.89 Å with the introduction of the smaller-size bromide ion. The corresponding histograms for their size distribution of them are shown in **Figure 5.2d–5.2f**. With an increasing proportion of iodine, the diameter of the perovskite NCs in the glasses is found to obviously decrease from 24.17 to 14.04 nm. This phenomenon can be attributed to the easy deliquescence of NaI during the preparation process for samples. **Figure 5.2g–5.2i** show energy-dispersive X-ray spectroscopy (EDS) mappings for BIA, BIB, and BIC, respectively, which confirms a uniform elemental spatial distribution. In addition, high-resolution XPS element mappings for the BIA, BIB, BIC NC glasses confirm that the elements of the samples are embedded into the inorganic oxide glass matrix (**Figure 5.3**). As shown in **Figure 5.4**, the element signals of Si, Al, Mg, Zn, O, B, Cs, Pb, Br and I are recorded in the XPS spectrum.

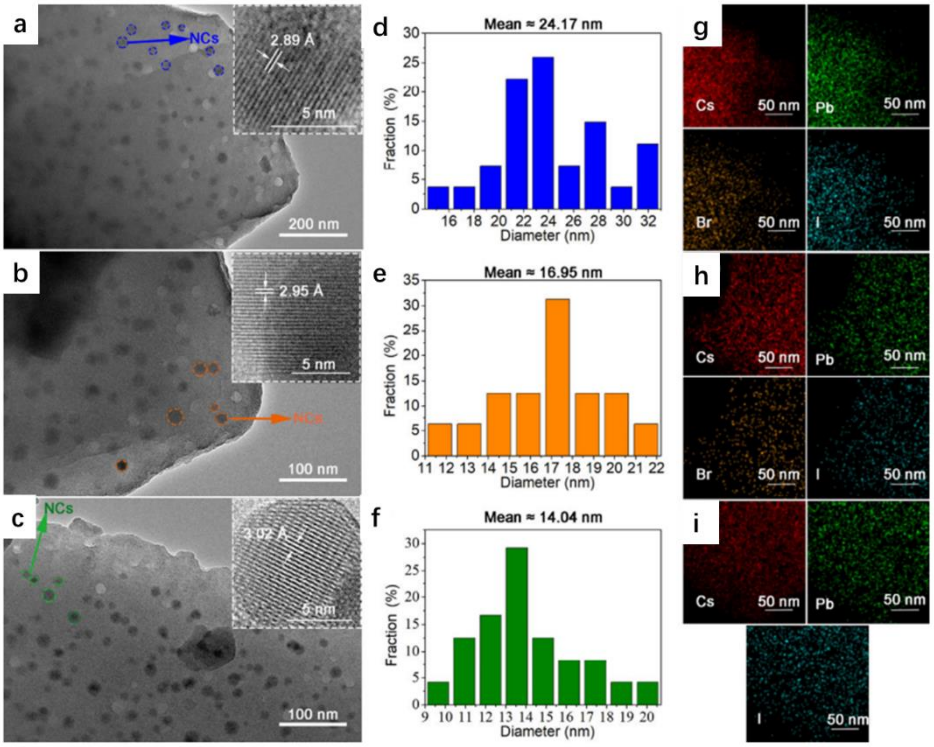

Figure 5.2 TEM images of perovskite glasses. (a)–(c) TEM images of BIA, BIB, and BIC, respectively. The insets show the HRTEM images of them. (d)–(f) Corresponding histograms for the size distribution. (g)–(i) EDS elemental mappings for BIA, BIB and BIC, respectively.

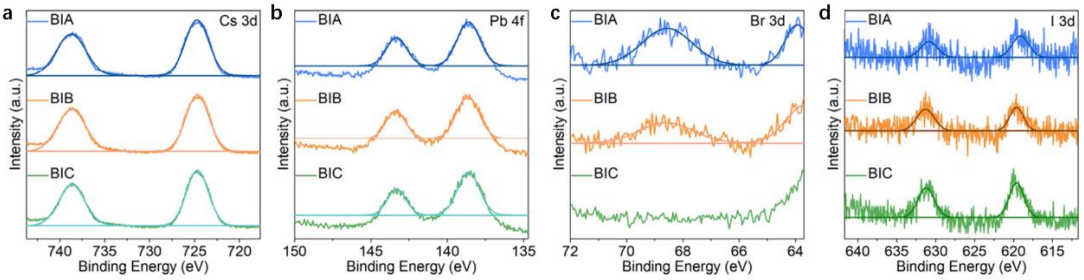

Figure 5.3 The high-resolution XPS spectra corresponding to the (a) Cs 3d, (b) Pb 4f, (c) Br 3d and (d) I 3d levels.

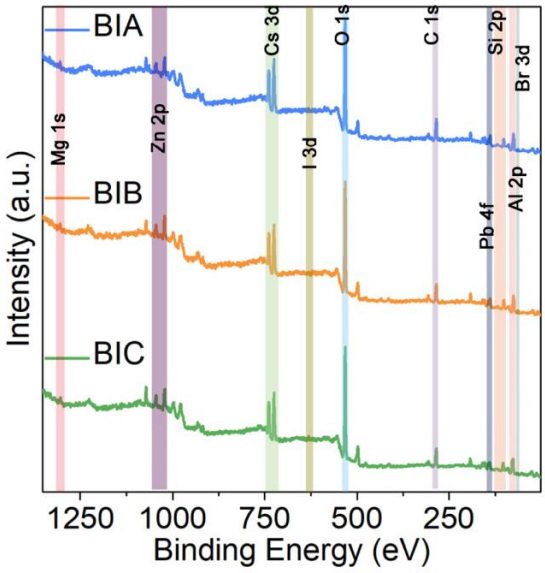

Figure 5.4 Full XPS scan spectra of BIA, BIB and BIC.

5.4 Optical gain

The optical gain coefficient is often used as an important parameter to predict the threshold value for materials.[188] The optical gain, which is like optical absorption, describes the light amplification (or exponential increase of light intensity) as light propagates along an optical waveguide filled with the gain medium. The optical loss refers to the photon scattering and non-radiation recombination, it occurs inevitably when the light is transmitting in the medium. There are many methods to measure optical gain, such as the VSL method and transmission method.[189] To explore which material out of BIA, BIB, and BIC is suitable for use as a gain medium for the red-emitting region, the optical gain coefficients for these NCs glasses were measured by the VSL method. The accurate conception of the optical gain value measured by the

VSL method is the comprehensive performance of optical gain value and optical loss. Only if the optical gain value exceeds the optical loss value, a positive net gain can be got, and then the lasing can be achieved. The values for the optical gain coefficients were calculated by using the equation: $I = A(e^{gL} - 1)/\mathrm{g}$, where I is the emission intensity, L stands for the stripe length, and g stands for the optical gain coefficient. As demonstrated in **Figure 5.5**, with increasing pump density, the optical gain coefficients for BIB and BIC are negative, which means that light loss exceeds light amplification; hence, these materials may not be suitable for use as an optical gain medium. However, the optical gain coefficient for BIA is found to be positive. Namely, the optical amplification far exceeds the optical loss. Moreover, as the pump density continues to increase to reach a value of ~2.36 mJ cm^{-2}, the optical gain coefficient reaches ~5 cm^{-1}. In general, the larger the optical gain, the easier it is to realize lasing and the lower the lasing threshold. Hence, the introduction of bromine ions can significantly improve the optical gain coefficient, with BIA showing up as the most promising optical gain medium among all the samples studied.

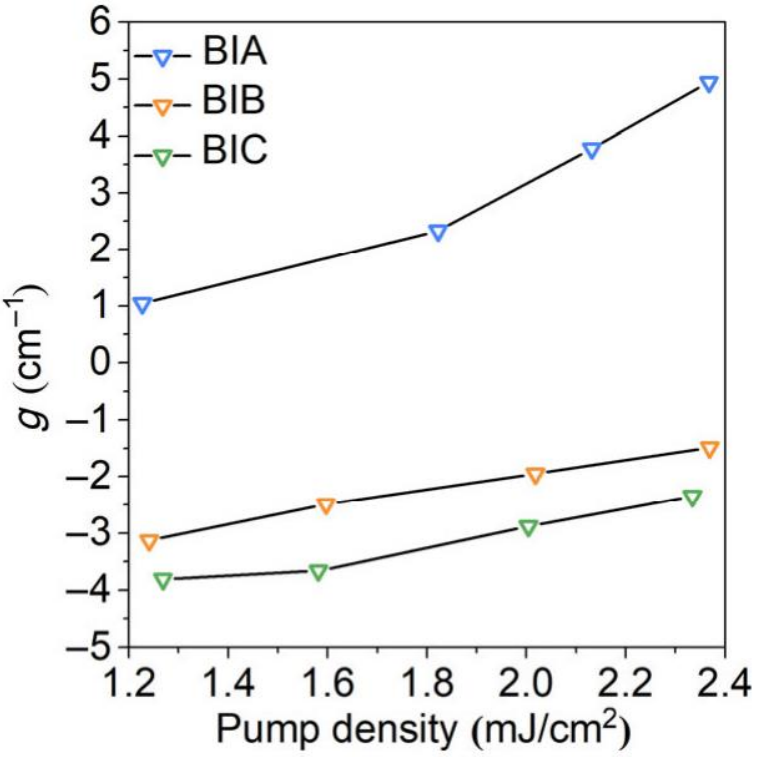

Figure 5.5 The measurement of the optical gain coefficients for BIA, BIB, and BIC with pump intensity, which is measured at room temperature with 800 nm pulse laser excitation.

5.5 Low temperature lasing

To verify the above hypothesis, BIA was pumped by an 800 nm pulse laser at −180 °C. **Figure 5.6b** shows the PL spectrum obtained for BIA at different pump intensities, and it is found that the spontaneous emission (SE) has a wide full width at half maximum (FWHM, ~9 nm) under low pump energy. The SE refers to a ubiquitous process, namely, when the pump intensity is lower than the lasing threshold, the emission spectrum shows a broad emission with large FWHM.[172] As demonstrated in **Figure 5.6c**, when

the pump intensity exceeds ~0.79 mJ cm^{-2}, a sharp increase in the intensity of the emission is accompanied by an obvious decrease in FWHM (~3 nm), indicating the achievement of random lasing from a red-emitting PNG. Compared to lasers that capture light with cavities, random lasing is achieved by the randomly optical feedback pathway between the inhomogeneity of NCs and the glassy medium (**Figure 5.6a**), which has lower coherence and less strict requirements on the optical cavity. Here, perovskite NCs act as the optical materials, and glassy matrix acts as the optical transmission medium. Besides, the random optical feedback pathway between the inhomogeneity of NCs and the glassy medium was widely reported in the field of random lasing.[190] The inset of **Figure 5.6b** shows the unique feature of random lasing in that it can be observed in different directions; random lasing can be widely used in biological imaging and speckle-free imaging.[125]

Besides, to prove that the lasing emission in this work stems from random cavities mode, here we study the relationship of $A_{th}^{2/3}$ and as a function of the inverse of P_{th}. As shown in **Figure 5.7** in the ESM, the linear relationship of $A_{th}^{2/3}$ and inverse of P_{th} manifests that the lasing characteristics of BIA are following the random laser theory [43]. Moreover, the random lasing observed for BIA was characterized by tuning the test temperature from 30 °C to −180 °C with ~0.79 mJ cm^{-2}. As shown in **Figure 5.6d**, at −60 °C, the phenomenon of random lasing begins to appear, with the SE gradually becoming weaker below −60 °C. With increasing test temperature, we find that the

fluorescence intensity is attenuated and the FWHM is broadened, which can be attributed to the increased probability of non-radiative composite relaxation and exciton phonon elastic scattering. The bi-exciton binding energy (Eb) of BIA was calculated according to temperature-dependent PL (213–283 K) with the equation:$A = I(T) = I_0/(1 + Ae^{-E_b/k_BT})$, where I(T) and I0 represent the UC emission intensity at T K and 0 K, respectively. kB is the Boltzmann constant, and A is a constant. **Figure 5.8** in the ESM shows the fitted curves for BIA with the goodness of fitted data with R2 = 0.9996. The calculated value of Eb for BIA is ~25 meV, which is considerably higher than the $CsPb(Br/I)_3$ NCs glasses reported in the past (5.164 meV). High Eb means the existence and stability of excitons, which is more advantageous to light-emitting devices because valid radiative recombination can be achieved through the excitons at relatively lower carrier densities.[191] As shown in **Figure 5.9** in the ESM, BIB, and BIC were also explored at diverse pump intensities, which confirmed the speculation that these NCs glasses cannot show random lasing action due to propagation losses. We note that the QE for BIB is higher than that for BIA, but the optical gain coefficient is lower than that for BIA. Based on the above results, we speculate that the optical gain coefficient is a more accurate parameter for predicting the lasing threshold in a PNG, and that a low QE does not necessarily lead to low gain mediators. This phenomenon has been widely emphasized in previous reports, for example, single-photon excited CdS/ZnS nanoplatelets can achieve lasing despite having a PLQY of less than 2%.[192]

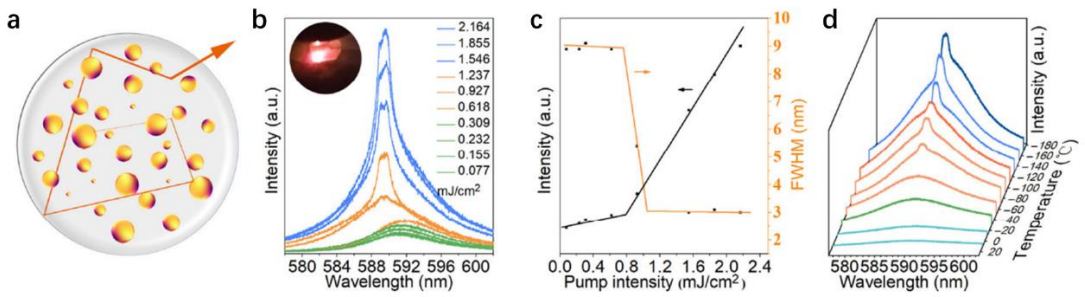

Figure 5.6 Low-temperature lasing performance of BIA. (a) The schematic diagram for random lasing realized by PNG. The spheres represent NCs evenly distributed in the glass matrix. (b) Pump intensity-dependent PL spectra for BIA. The inner illustration shows BIA excited by an 800 nm pulse laser at −180 °C. (c) A plot of the integrated lasing intensity as a function of pump intensity. (d) Temperature-dependent PL spectra for BIA.

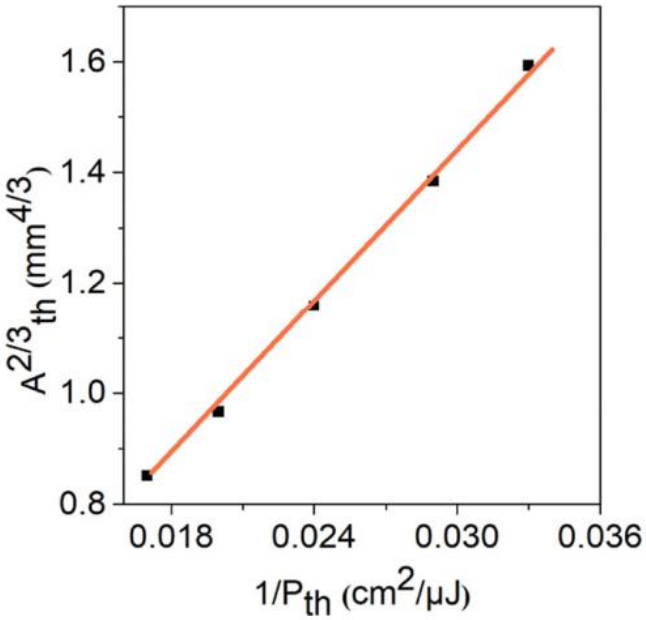

Figure 5.7 Random lasing threshold of BIA for different excitation areas (A_{th}). A_{th}: the threshold of the excitation area. P_{th}: the lasing threshold. The measurement was performed at –180°C.

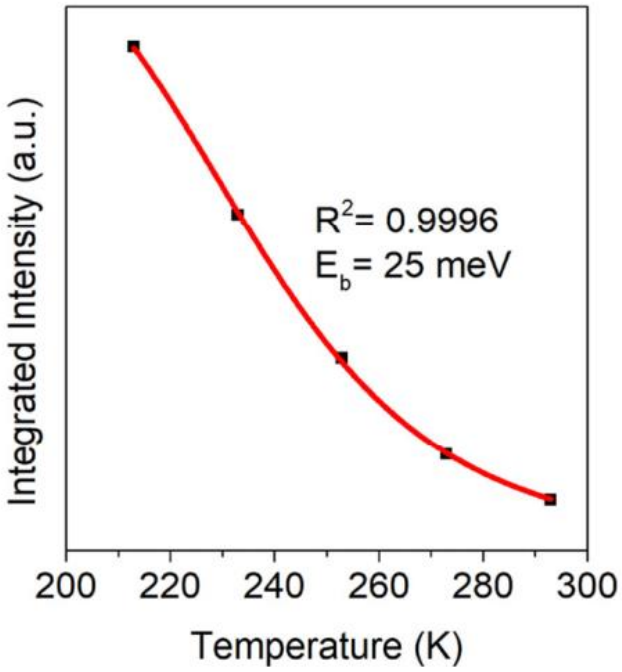

Figure 5.8 The integrated emission intensity versus temperature.

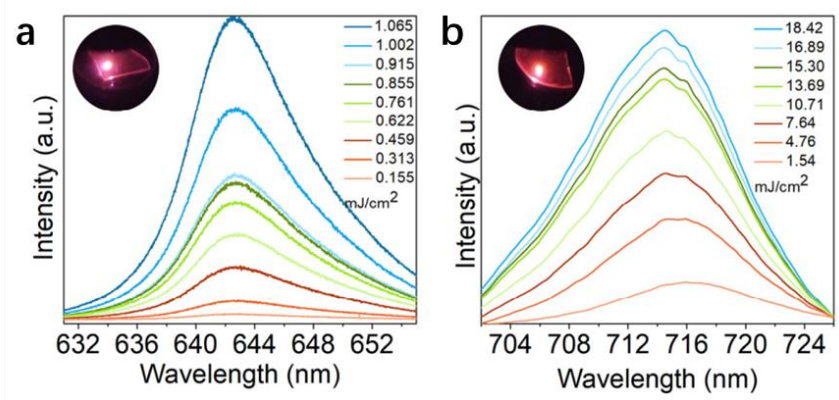

Figure 5.9 Pump intensity-dependent PL spectra of BIB (a) and BIC (b). The inner illustrations show BIB and BIC under the excitation of an 800 nm pulse laser, respectively.

5.6 Water stability

Water stability is an unavoidable difficulty in the practical application of perovskite NCs. In previous literature, SiO2 packing is often used to realize water stability.[184] To evaluate the waterproof capability of PNG, BIA was immersed in deionized water for seven days. As shown in **Figure 5.10a**, the fluorescence intensity for BIA was found to remain above 95% after soaking in water for seven days. In addition, the lasing behavior for the sample was tested again under the same conditions, which showed that BIA could still achieve random lasing after being immersed in water. As shown in **Figure 5.10b**, the corresponding lasing threshold value increased to ~0.95 mJ cm^{-2} after immersing in water for one day, followed by only a slight increase over seven days. This may be attributed to the decomposition of a small amount of perovskite NCs present on the glass surface in water. As shown in **Figure 5.11** in the ESM, BIC also showed extremely strong stability in water. After seven days of immersion, the relative PL intensity was found to be maintained at 85%.

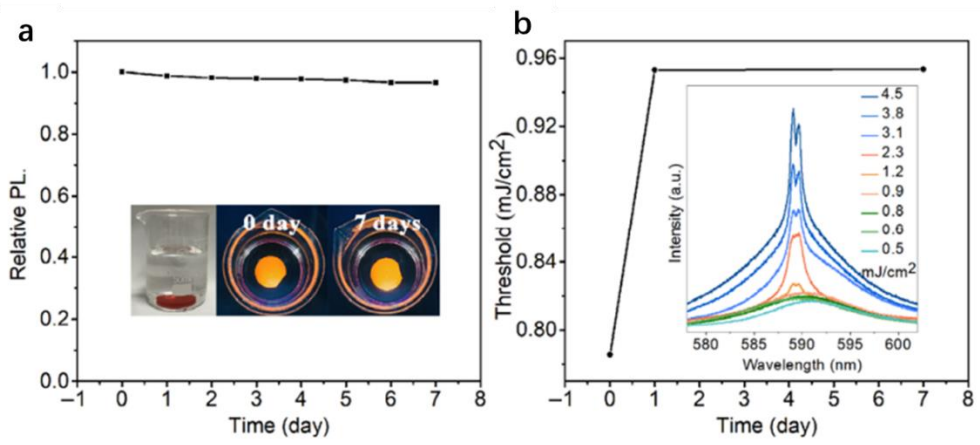

Figure 5.10 Water stability analysis of BIA. (a) Relative PL intensities for BIA immersed in water for seven days were measured with an excitation wavelength of 460 nm. The insets show BIA in water under daylight and an ultraviolet lamp. (b) Lasing threshold-dependent immersion time spectra for BIA.

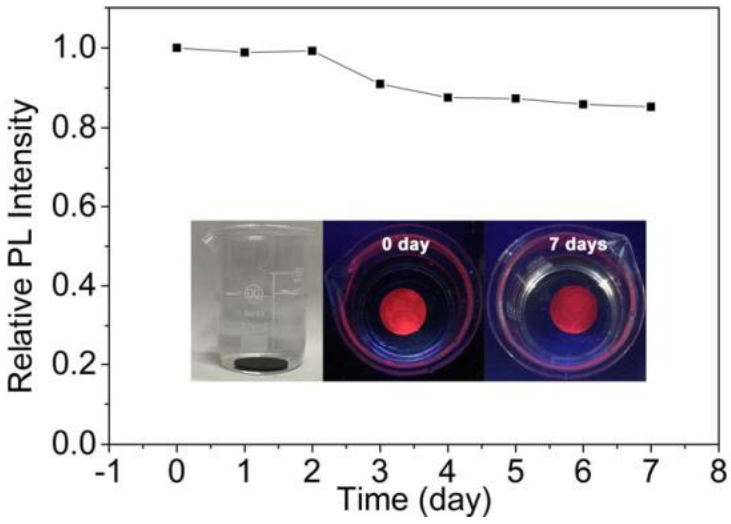

Figure 5.11 Relative PL intensities of BIC immersed in water. The insets show BIC in water under daylight and an ultraviolet lamp.

5.7 Conclusions

In summary, a series of perovskite NCs glasses (BIA, BIB, and BIC) with red-emission were successfully prepared by managing the halogen ratio. The optical gain and upconversion efficiency for the $CsPbI_3$ NCs was found to be improved by Br doping. Here, under the excitation of an 800 nm pulse laser, random lasing at 590 nm was achieved for BIA with the demonstration of a lasing threshold of ~0.79 mJ cm^{-2} at −180°C. In addition, BIA showed random lasing after immersion in water for one week, with only a slight increase in the lasing threshold observed. This work reveals the feasibility of water-resistant $CsPb(Br/I)_3$ NCs glasses to bridge the “red gap” for meeting the demand for HD displays and infrared detection in extreme climates.

Chapter 6 Conclusions and Outlook

6.1 Conclusions

In this thesis, we systematically investigated the lasing performance of MHPs with a variety of dimensions as optical gain media, from low dimensional to 3D structures, and the mechanisms behind their lasing behaviors are also discussed. We also synthesized a series of MHP materials from quantum dots, 2D layered structures to micro crystals. To deeply understand their lasing performance, we studied their optical properties as well as their PL spectra, absorption, and nonlinear properties. Some unique techniques are developed in our lab to analyze the specific sample, such as the micro Z-scan. Comparing the properties among them, the 2D structure has higher stability in the ambient conditions, while the quantum dots and micro crystals have higher PLQY and a low lasing threshold.

We firstly synthesized the so-called 0D MHPs quantum dots as a gain medium to apply to flexible microlasers, they have uniform size distribution of 8 nm and their PLQY is as high as 96%. The previous flexible laser used organic polymers as the substrate, but they have many disadvantages, such as easier damage by the thermal effect generated from the external injected carriers. We overcome this issue by using flexible metal as the substrate. The advantage of using the flexible metallic structure as the substrate of

flexible lasers over plastic materials is its well-controlled shape and strong mechanical strength. Then we proposed to deposit $CsPbBr_3$ perovskite quantum dots onto Ni porous foam for the realization of flexible lasers. Under two-photon 800 nm excitation at room temperature, we observe incoherent random lasing emission at ~537 nm, and the lasing threshold is about 190 μJ cm^{-2}. By external deformation of the Ni porous foam, incoherent random lasing can be tuned to amplified spontaneous emission as well as the corresponding lasing threshold can be controlled. More importantly, we have demonstrated that the laser is robust to intensive bending (>1000 bending cycles) with minimum effect on the lasing intensity. This flexible laser is also shown to be an ideal light source to produce a 'speckle' free micro-image, which can be used in laser imaging.

Then the 2D RPP crystals were fabricated due to their QW-like structures with strong exciton confinement and high stability in air. We firstly demonstrate the low-threshold upconversion lasing from the homologous RPP $(PEA)_2(MA)_{n-1}Pb_nI_{3n+1}$ ($n = 2, 3$) micro-flakes with the emission wavelength varies from 598 to 637 nm under 800 nm laser excitation at low temperature (≤ 153 K). To investigate their nonlinear effect, a micro Z-scan technique used to test the transmission of micro-size samples was developed in our lab. Using the micro Z-scan technique, we discovered that the RPP flakes have a giant two-photon absorption coefficient β as high as 3.6×10^3 cm GW^{-1}, resulting in the effective upconversion transition under two-photon excitation, which is essential for upconversion lasing. Furthermore, the self-formation of Fabry–Pérot microcavities

can reduce the optical loss, which provides the support for lasing emission from the $n \geq 2$ RPP flakes and the threshold is 1.2 GW cm^{-2} and 0.7 GW cm^{-2}, for $n = 2$ and 3, respectively. We also used the laser and gain models to calculate the optical gain and loss. Furthermore, microscopic transient absorption measurements are used to reveal that low-threshold lasing is due to the high differential gain coefficient and the suppressed non-radiative Auger recombination rate inside the quantum confinement structures. These properties distinguish RPPs as promising gain media favorable for developing efficient upconversion microcavity lasers.

Finally, 3D $CsPbX_3$ (X = Br, I) crystals were fabricated with the protection of a glassy matrix due to the poor stability of MHPs, especially for the mixed halogen as the ions migrate. Perovskite materials have received extensive attention as optical gain media. By doping Br^- ions into the $CsPbI_3$ crystals to partially replace I^- ions, the optical efficiency was found to be significantly improved. As the optical gain is a key factor of the optical gain medium, we used the VSL method to determine the optical gain of our samples. Only the optical gain of the Br^- doped sample is positive, others are negative. Here, under 800 nm pulse laser excitation, red random lasing with the threshold of 1.1 mJ cm^{-2} was realized with the assistance of such anion modulation. But unfortunately, this is just achieved at low temperatures. Moreover, we demonstrate that the perovskite glasses (PNG) show strong water stability after immersion in water for one week,

indicating a promise for application in high-definition (HD) displays and photonic devices.

6.2 Outlook

All these results indicate that MHPs are favorable laser gain media for application in micro and visible lasers, even in electrically pumped lasers. However, it is still a challenge to fabricate electrically pumped perovskite lasers due to the insufficient electrical-to-optical conversion efficiency. Therefore, there are some issues to be dissolved in the future.

To find low threshold MHPs

Due to the special QW-like structures demonstrated in Chapter 4, the 2D RPPs have many advantages as laser gain media, such as strong exciton confinement, tunable thickness, and shape. QW structures are promising structures for developing laser diodes because this structure enables the effective carrier combination at high temperatures. Our previous study has confirmed that the QW structures have high differential optical gain, which can overwhelm the optical loss from non-radiative recombination. Hence, 2D RPPs are a good candidate for realizing MHPs laser diode. As their organic spacer and embedded molecules can be changed with different chemical groups, these chemicals will have different lengths, hydrogen bonds, and electronegativities, which maybe have an impact on their lasing performances. We

propose to synthesize a series of 2D RPPs with different compositions, and we will investigate their relationship between structures and lasing characters, such as threshold, optical gain, operation temperature and stability.

To integrate MHPs with a matrix of good thermal conductivity

CW laser pumped population conversion is the essential step before realizing the electrically pumped MHPs lasers. To achieve CW exciting lasers, the materials should have very good thermal conductivity to make sure that materials cannot be damaged during the long-time joule heating from illumination. Unfortunately, the MHPs themselves are unstable in such conditions. In our previous study in Chapters 3 and 5, the MHPs nano crystal protected by glass, have a significant improvement in their thermal stability. Therefore, the effective way to solve this problem is to use external materials to protect the MHPs nanoparticles or layered flakes, such as glass or other transparent materials. There are many candidates, such as TiO2, quartz, and diamond. Among them, the diamond has the best thermal conductivity, so we plan to use layer 2D MHPs as an active layer, protected by diamond, to fabricate an MHP laser diode.

To realize polariton lasers

As demonstrated in chapter 2, the exciton-polariton laser can reduce the requirement of the thermal stability of the gain media because they do not need population inversion under high injected carrier density. High binding energy is essential for achieving a

polariton laser with a lower threshold, so the best candidate for this application is 2D RPPs. According to the structure of traditional semiconductor polariton lasers, we propose to combine the 2D RPPs in VCSEL and LEDs architectures. Also, 2D RPPs can integrate with other cavities, such as DFB and FP, which are helpful to reduce the optical loss, leading to threshold decrease. With a deep understanding of the lasing mechanism of MHPs lasers, it is believed that the MHPs laser diode will be realized soon.

References

1. *Lasing Transitions and Gain*, in *Fundamentals of Light Sources and Lasers*. 2004. p. 117-158.
2. *Lasing Processes*, in *Fundamentals of Light Sources and Lasers*. 2004. p. 83-115.
3. Fu, Y., et al., *Metal halide perovskite nanostructures for optoelectronic applications and the study of physical properties.* Nature Reviews Materials, 2019. **4**(3): p. 169-188.
4. Brenner, T.M., et al., *Hybrid organic—inorganic perovskites: low-cost semiconductors with intriguing charge-transport properties.* Nature Reviews Materials, 2016. **1**(1): p. 15007.
5. Sutherland, B.R., et al., *Perovskite Thin Films via Atomic Layer Deposition.* Advanced Materials, 2015. **27**(1): p. 53-58.
6. Kondo, T., et al., *Biexciton lasing in the layered perovskite-type material (C6H13NH3)2PbI4.* Solid State Communications, 1998. **105**(4): p. 253-255.
7. Xing, G., et al., *Low-temperature solution-processed wavelength-tunable perovskites for lasing.* Nat Mater, 2014. **13**(5): p. 476-80.
8. Zhang, Q., et al., *Room-Temperature Near-Infrared High-Q Perovskite Whispering-Gallery Planar Nanolasers.* Nano Letters, 2014. **14**(10): p. 5995-6001.

9. Deschler, F., et al., *High Photoluminescence Efficiency and Optically Pumped Lasing in Solution-Processed Mixed Halide Perovskite Semiconductors.* The Journal of Physical Chemistry Letters, 2014. **5**(8): p. 1421-1426.

10. Qin, C., et al., *Stable room-temperature continuous-wave lasing in quasi-2D perovskite films.* Nature, 2020. **585**(7823): p. 53-57.

11. Zhou, Y., et al., *Nonlinear optical properties of halide perovskites and their applications.* Applied Physics Reviews, 2020. **7**(4).

12. Wells, H.L., *ART. XVI.--On the Coesium-and the Potassium-Lead Halides.* American Journal of Science (1880-1910), 1893. **45**(266): p. 121.

13. Ishihara, T., J. Takahashi, and T. Goto, *Optical properties due to electronic transitions in two-dimensional semiconductors (CnH2n+1NH3)2PbI4.* Phys Rev B Condens Matter, 1990. **42**(17): p. 11099-11107.

14. Hong, X., T. Ishihara, and A.V. Nurmikko, *Dielectric confinement effect on excitons in PbI4-based layered semiconductors.* Phys Rev B Condens Matter, 1992. **45**(12): p. 6961-6964.

15. Mitzi, D.B., et al., *Conducting tin halides with a layered organic-based perovskite structure.* Nature, 1994. **369**(6480): p. 467-469.

16. Mitzi, D.B., et al., *Conducting Layered Organic-inorganic Halides Containing <110>-Oriented Perovskite Sheets.* Science, 1995. **267**(5203): p. 1473-6.

17. Ambrosio, F., et al., *Origin of low electron–hole recombination rate in metal halide perovskites.* Energy & Environmental Science, 2018. **11**(1): p. 101-105.

18. Dong, H., et al., *Materials chemistry and engineering in metal halide perovskite lasers.* Chem Soc Rev, 2020. **49**(3): p. 951-982.

19. de Quilettes, D.W., et al., *Impact of microstructure on local carrier lifetime in perovskite solar cells.* Science, 2015. **348**(6235): p. 683.

20. Shi, D., et al., *Solar cells. Low trap-state density and long carrier diffusion in organolead trihalide perovskite single crystals.* Science, 2015. **347**(6221): p. 519-22.

21. Stranks, S.D., et al., *Electron-hole diffusion lengths exceeding 1 micrometer in an organometal trihalide perovskite absorber.* Science, 2013. **342**(6156): p. 341-344.

22. Cao, Y., et al., *Perovskite light-emitting diodes based on spontaneously formed submicrometre-scale structures.* Nature, 2018. **562**(7726): p. 249-253.

23. Lin, K., et al., *Perovskite light-emitting diodes with external quantum efficiency exceeding 20 per cent.* Nature, 2018. **562**(7726): p. 245-248.

24. Kojima, A., et al., *Organometal Halide Perovskites as Visible-Light Sensitizers for Photovoltaic Cells.* Journal of the American Chemical Society, 2009. **131**(17): p. 6050-6051.

25. Noh, J.H., et al., *Chemical Management for Colorful, Efficient, and Stable Inorganic–Organic Hybrid Nanostructured Solar Cells.* Nano Letters, 2013. **13**(4): p. 1764-1769.

26. Dong, Q., et al., *Solar cells. Electron-hole diffusion lengths > 175 mum in solution-grown CH3NH3PbI3 single crystals.* Science, 2015. **347**(6225): p. 967-70.

27. Kim, M., et al., *Methylammonium Chloride Induces Intermediate Phase Stabilization for Efficient Perovskite Solar Cells.* Joule, 2019. **3**(9): p. 2179-2192.

28. Xiong, Z., et al., *Simultaneous Interfacial Modification and Crystallization Control by Biguanide Hydrochloride for Stable Perovskite Solar Cells with PCE of 24.4%.* Advanced Materials, 2022. **34**(8): p. 2106118.

29. Chen, S., et al., *High-Q, Low-Threshold Monolithic Perovskite Thin-Film Vertical-Cavity Lasers.* Adv Mater, 2017. **29**(16): p. 1604781.

30. Jia, Y., et al., *Diode-pumped organo-lead halide perovskite lasing in a metal-clad distributed feedback resonator.* Nano letters, 2016. **16**(7): p. 4624-4629.

31. Zhizhchenko, A., et al., *Single-Mode Lasing from Imprinted Halide-Perovskite Microdisks.* ACS Nano, 2019. **13**(4): p. 4140-4147.

32. Jia, Y., et al., *Continuous-wave lasing in an organic–inorganic lead halide perovskite semiconductor.* Nature Photonics, 2017. **11**(12): p. 784-788.

33. Wei, H., et al., *Sensitive X-ray detectors made of methylammonium lead tribromide perovskite single crystals.* Nature Photonics, 2016. **10**(5): p. 333-339.

34. Im, J.-H., et al., *Nanowire Perovskite Solar Cell.* Nano Letters, 2015. **15**(3): p. 2120-2126.

35. Zhang, D., et al., *Solution-phase synthesis of cesium lead halide perovskite nanowires.* Journal of the American Chemical Society, 2015. **137**(29): p. 9230-9233.

36. Schmidt, L.C., et al., *Nontemplate synthesis of CH3NH3PbBr3 perovskite nanoparticles.* Journal of the American Chemical Society, 2014. **136**(3): p. 850-853.

37. Huang, H., et al., *Control of Emission Color of High Quantum Yield CH3NH3PbBr3 Perovskite Quantum Dots by Precipitation Temperature.* Advanced Science, 2015. **2**(9): p. 1500194.

38. Saliba, M., et al., *Incorporation of rubidium cations into perovskite solar cells improves photovoltaic performance.* Science, 2016. **354**(6309): p. 206-209.

39. Xu, W.-J., et al., *Hybrid organic-inorganic perovskites: Polar properties and applications.* Coordination Chemistry Reviews, 2019. **387**: p. 398-414.

40. Quan, L.N., et al., *Perovskites for Next-Generation Optical Sources.* Chemical Reviews, 2019. **119**(12): p. 7444-7477.

41. Ptak, M., et al., *Experimental and theoretical studies of structural phase transition in a novel polar perovskite-like [C2H5NH3][Na0.5Fe0.5(HCOO)3] formate.* Dalton Transactions, 2016. **45**(6): p. 2574-2583.

42. Li, B., et al., *Polar rotor scattering as atomic-level origin of low mobility and thermal conductivity of perovskite CH3NH3PbI3.* Nature Communications, 2017. **8**(1): p. 16086.

43. Anusca, I., et al., *Dielectric response: Answer to many questions in the methylammonium lead halide solar cell absorbers.* Advanced Energy Materials, 2017. **7**(19): p. 1700600.

44. Tan, H., et al., *Dipolar cations confer defect tolerance in wide-bandgap metal halide perovskites.* Nature communications, 2018. **9**(1): p. 1-10.

45. De Wolf, S., et al., *Organometallic halide perovskites: sharp optical absorption edge and its relation to photovoltaic performance.* The journal of physical chemistry letters, 2014. **5**(6): p. 1035-1039.

46. Jung, M., et al., *Perovskite precursor solution chemistry: from fundamentals to photovoltaic applications.* Chemical Society Reviews, 2019. **48**(7): p. 2011-2038.

47. Jeon, N.J., et al., *Solvent engineering for high-performance inorganic–organic hybrid perovskite solar cells.* Nature Materials, 2014. **13**(9): p. 897-903.

48. Liao, Q., et al., *Perovskite Microdisk Microlasers Self-Assembled from Solution.* Advanced Materials, 2015. **27**(22): p. 3405-3410.

49. Xing, J., et al., *Vapor Phase Synthesis of Organometal Halide Perovskite Nanowires for Tunable Room-Temperature Nanolasers.* Nano Letters, 2015. **15**(7): p. 4571-4577.

50. He, X., et al., *Patterning Multicolored Microdisk Laser Arrays of Cesium Lead Halide Perovskite.* Advanced Materials, 2017. **29**(12): p. 1604510.

51. Zhang, N., et al., *Highly Reproducible Organometallic Halide Perovskite Microdevices based on Top-Down Lithography.* Advanced Materials, 2017. **29**(15): p. 1606205.

52. Umebayashi, T., et al., *Electronic structures of lead iodide based low-dimensional crystals.* Physical Review B, 2003. **67**(15): p. 155405.

53. Brivio, F., et al., *Relativistic quasiparticle self-consistent electronic structure of hybrid halide perovskite photovoltaic absorbers.* Physical Review B, 2014. **89**(15): p. 155204.

54. Du, M.H., *Efficient carrier transport in halide perovskites: theoretical perspectives.* Journal of Materials Chemistry A, 2014. **2**(24): p. 9091-9098.

55. Xing, G., et al., *Solution-Processed Tin-Based Perovskite for Near-Infrared Lasing.* Advanced Materials, 2016. **28**(37): p. 8191-8196.

56. Zhu, H., et al., *Organic Cations Might Not Be Essential to the Remarkable Properties of Band Edge Carriers in Lead Halide Perovskites.* Advanced Materials, 2017. **29**(1): p. 1603072.

57. Mitzi, D.B., et al., *Conducting tin halides with a layered organic-based perovskite structure.* Nature, 1994. **369**(6480): p. 467-469.

58. Johnston, M.B. and L.M. Herz, *Hybrid Perovskites for Photovoltaics: Charge-Carrier Recombination, Diffusion, and Radiative Efficiencies.* Accounts of Chemical Research, 2016. **49**(1): p. 146-154.

59. Gélvez-Rueda, M.C., et al., *Interconversion between free charges and bound excitons in 2D hybrid lead halide perovskites.* The Journal of Physical Chemistry C, 2017. **121**(47): p. 26566-26574.

60. Miyata, A., et al., *Direct measurement of the exciton binding energy and effective masses for charge carriers in organic–inorganic tri-halide perovskites.* Nature Physics, 2015. **11**(7): p. 582-587.

61. Wehrenfennig, C., et al., *High charge carrier mobilities and lifetimes in organolead trihalide perovskites.* Advanced materials, 2014. **26**(10): p. 1584-1589.

62. Bretschneider, S.A., et al., *Quantifying Polaron Formation and Charge Carrier Cooling in Lead-Iodide Perovskites.* Advanced Materials, 2018. **30**(29): p. 1707312.

63. Zhu, X.Y. and V. Podzorov, *Charge Carriers in Hybrid Organic–Inorganic Lead Halide Perovskites Might Be Protected as Large Polarons.* The Journal of Physical Chemistry Letters, 2015. **6**(23): p. 4758-4761.

64. Wehrenfennig, C., et al., *Charge-carrier dynamics in vapour-deposited films of the organolead halide perovskite CH 3 NH 3 PbI 3− x Cl x.* Energy & Environmental Science, 2014. **7**(7): p. 2269-2275.

65. Rehman, W., et al., *Charge-carrier dynamics and mobilities in formamidinium lead mixed-halide perovskites.* Advanced Materials, 2015. **27**(48): p. 7938-7944.

66. Sheik-Bahae, M. and R.I. Epstein, *Can laser light cool semiconductors?* Physical review letters, 2004. **92**(24): p. 247403.

67. Chen, Q., et al., *Under the spotlight: The organic–inorganic hybrid halide perovskite for optoelectronic applications.* Nano Today, 2015. **10**(3): p. 355-396.

68. Dong, Q., et al., *Electron-hole diffusion lengths > 175 μm in solution-grown CH₃NH₃PbI₃ single crystals.* Science, 2015. **347**(6225): p. 967-970.

69. Deschler, F., et al., *High photoluminescence efficiency and optically pumped lasing in solution-processed mixed halide perovskite semiconductors.* The journal of physical chemistry letters, 2014. **5**(8): p. 1421-1426.

70. Cho, H., et al., *Overcoming the electroluminescence efficiency limitations of perovskite light-emitting diodes.* Science, 2015. **350**(6265): p. 1222-1225.

71. Chondroudis, K. and D.B. Mitzi, *Electroluminescence from an organic− inorganic perovskite incorporating a quaterthiophene dye within lead halide perovskite layers.* Chemistry of materials, 1999. **11**(11): p. 3028-3030.

72. Yuan, M., et al., *Perovskite energy funnels for efficient light-emitting diodes.* Nature Nanotechnology, 2016. **11**(10): p. 872-877.

73. Pan, J., et al., *Highly efficient perovskite-quantum-dot light-emitting diodes by surface engineering.* Advanced materials, 2016. **28**(39): p. 8718-8725.

74. Chen, S., et al., *A photonic crystal laser from solution based organo-lead iodide perovskite thin films.* Acs Nano, 2016. **10**(4): p. 3959-3967.

75. Zhang, Q., et al., *Halide Perovskite Semiconductor Lasers: Materials, Cavity Design, and Low Threshold.* Nano Lett, 2021. **21**(5): p. 1903-1914.

76. Protesescu, L., et al., *Nanocrystals of cesium lead halide perovskites (CsPbX3, X= Cl, Br, and I): novel optoelectronic materials showing bright emission with wide color gamut.* Nano letters, 2015. **15**(6): p. 3692-3696.

77. Zhang, Q., et al., *High-quality whispering-gallery-mode lasing from cesium lead halide perovskite nanoplatelets.* Advanced Functional Materials, 2016. **26**(34): p. 6238-6245.

78. Do, T.T.H., et al., *Bright exciton fine-structure in two-dimensional lead halide perovskites.* Nano Letters, 2020. **20**(7): p. 5141-5148.

79. Kondo, S., et al., *Photoluminescence and stimulated emission from microcrystalline $\mathrm{Cs}\mathrm{Pb}{\mathrm{Cl}}_{3}$ films prepared by amorphous-to-crystalline transformation.* Physical Review B, 2004. **70**(20): p. 205322.

80. Arora, N., et al., *Photovoltaic and amplified spontaneous emission studies of high-quality formamidinium lead bromide perovskite films.* Advanced Functional Materials, 2016. **26**(17): p. 2846-2854.

81. Saliba, M., et al., *Structured organic–inorganic perovskite toward a distributed feedback laser.* Advanced Materials, 2016. **28**(5): p. 923-929.

82. Pourdavoud, N., et al., *Room-temperature stimulated emission and lasing in recrystallized cesium lead bromide perovskite thin films.* Advanced Materials, 2019. **31**(39): p. 1903717.

83. Qin, C., et al., *Stable room-temperature continuous-wave lasing in quasi-2D perovskite films.* Nature, 2020. **585**(7823): p. 53-57.

84. Chen, S., et al., *High-Q, low-threshold monolithic perovskite thin-film vertical-cavity lasers.* Advanced Materials, 2017. **29**(16): p. 1604781.

85. Yakunin, S., et al., *Low-threshold amplified spontaneous emission and lasing from colloidal nanocrystals of caesium lead halide perovskites.* Nature communications, 2015. **6**(1): p. 1-9.

86. Wang, Y., et al., *Nonlinear Absorption and Low-Threshold Multiphoton Pumped Stimulated Emission from All-Inorganic Perovskite Nanocrystals.* Nano Letters, 2016. **16**(1): p. 448-453.

87. Hu, Z., et al., *Enhanced Two-Photon-Pumped Emission from In Situ Synthesized Nonblinking CsPbBr3/SiO2 Nanocrystals with Excellent Stability.* Advanced Optical Materials, 2018. **6**(3): p. 1700997.

88. Wang, Y., et al., *Solution-processed low threshold vertical cavity surface emitting lasers from all-inorganic perovskite nanocrystals.* Advanced Functional Materials, 2017. **27**(13): p. 1605088.

89. Wang, L., et al., *Ultralow-threshold and color-tunable continuous-wave lasing at room-temperature from in situ fabricated perovskite quantum dots.* The Journal of Physical Chemistry Letters, 2019. **10**(12): p. 3248-3253.

90. Imamog, A., et al., *Nonequilibrium condensates and lasers without inversion: Exciton-polariton lasers.* Physical Review A, 1996. **53**(6): p. 4250.

91. Deng, H., et al., *Polariton lasing vs. photon lasing in a semiconductor microcavity.* Proceedings of the National Academy of Sciences, 2003. **100**(26): p. 15318-15323.

92. Su, R., et al., *Room-temperature polariton lasing in all-inorganic perovskite nanoplatelets.* Nano letters, 2017. **17**(6): p. 3982-3988.

93. Li, C., et al., *Highly compact CsPbBr3 perovskite thin films decorated by ZnO nanoparticles for enhanced random lasing.* Nano Energy, 2017. **40**: p. 195-202.

94. Park, K., et al., *Light–Matter Interactions in Cesium Lead Halide Perovskite Nanowire Lasers.* The Journal of Physical Chemistry Letters, 2016. **7**(18): p. 3703-3710.

95. Pourdavoud, N., et al., *Distributed Feedback Lasers Based on MAPbBr3.* Advanced Materials Technologies, 2018. **3**(4): p. 1700253.

96. Zhu, H., et al., *Lead halide perovskite nanowire lasers with low lasing thresholds and high quality factors.* Nat Mater, 2015. **14**(6): p. 636-42.

97. Tian, C., et al., *Low-threshold room-temperature continuous-wave optical lasing of single-crystalline perovskite in a distributed reflector microcavity.* RSC Advances, 2019. **9**(62): p. 35984-35989.

98. Wang, Y., et al., *All-Inorganic Colloidal Perovskite Quantum Dots: A New Class of Lasing Materials with Favorable Characteristics.* Adv Mater, 2015. **27**(44): p. 7101-8.

99. Fu, Y., et al., *Broad Wavelength Tunable Robust Lasing from Single-Crystal Nanowires of Cesium Lead Halide Perovskites (CsPbX3, X = Cl, Br, I).* ACS Nano, 2016. **10**(8): p. 7963-7972.

100. Gharajeh, A., et al., *Continuous-wave operation in directly patterned perovskite distributed feedback light source at room temperature.* Optics Letters, 2018. **43**(3): p. 611-614.

101. Jiang, L., et al., *Continuous wave pumped single-mode nanolasers in inorganic perovskites with robust stability and high quantum yield.* Nanoscale, 2018. **10**(28): p. 13565-13571.

102. Evans, T.J.S., et al., *Continuous-Wave Lasing in Cesium Lead Bromide Perovskite Nanowires.* Advanced Optical Materials, 2018. **6**(2).

103. Li, Z., et al., *Room-Temperature Continuous-Wave Operation of Organometal Halide Perovskite Lasers.* ACS Nano, 2018. **12**(11): p. 10968-10976.

104. Wang, L., et al., *Ultralow-Threshold and Color-Tunable Continuous-Wave Lasing at Room-Temperature from In Situ Fabricated Perovskite Quantum Dots.* J Phys Chem Lett, 2019. **10**(12): p. 3248-3253.

105. Jia, Y., et al., *Factors that Limit Continuous-Wave Lasing in Hybrid Perovskite Semiconductors.* Advanced Optical Materials, 2019. **8**(2).

106. Bhattacharya, P., et al., *Room Temperature Electrically Injected Polariton Laser.* Physical Review Letters, 2014. **112**(23): p. 236802.

107. Savvidis, P.G., *A practical polariton laser.* Nature Photonics, 2014. **8**(8): p. 588-589.

108. Hu, J., et al., *Flexible integrated photonics: where materials, mechanics and optics meet* Optical Materials Express, 2013. **3**(9): p. 1313-1331.

109. Lee, Y.-J., et al., *Flexible random lasers with tunable lasing emissions.* Nanoscale, 2018. **10**(22): p. 10403-10411.

110. Ali, T., et al., *A Thin-Film Flexible Defect-Mode Laser.* Advanced Optical Materials, 2020. **8**(8): p. 1901891.

111. Li, X., et al., *Lotus-Leaf-Inspired Flexible and Tunable Random Laser.* ACS Applied Materials & Interfaces, 2020. **12**(8): p. 10050-10057.

112. Wang, Z., et al., *Air Stable Organic–Inorganic Perovskite Nanocrystals@Polymer Nanofibers and Waveguide Lasing.* Small, 2020. **16**(43): p. 2004409.

113. Lau, S.P., et al., *Flexible ultraviolet random lasers based on nanoparticles.* Small, 2005. **1**(10): p. 956-9.

114. Kim, J.-H., et al., *Tunable and flexible solvent-free liquid organic distributed feedback lasers.* Applied Physics Letters, 2015. **106**(5): p. 053302.

115. Karl, M., et al., *Flexible and ultra-lightweight polymer membrane lasers.* Nature Communications, 2018. **9**(1): p. 1525.

116. Wang, Y.C., et al., *Flexible Organometal-Halide Perovskite Lasers for Speckle Reduction in Imaging Projection.* ACS Nano, 2019. **13**(5): p. 5421-5429.

117. da Silva-Neto, M.L., et al., *UV random laser emission from flexible ZnO-Ag-enriched electrospun cellulose acetate fiber matrix.* Scientific Reports, 2019. **9**(1): p. 11765.

118. Liang, J., et al., *Recent Progress and Development in Inorganic Halide Perovskite Quantum Dots for Photoelectrochemical Applications.* Small, 2020. **16**(15): p. 1903398.

119. Liu, X., et al., *Metal Halide Perovskites: Synthesis, Ion Migration, and Application in Field-Effect Transistors.* Small, 2018. **14**(36): p. 1801460.

120. Gao, W. and S.F. Yu, *Reality or fantasy—Perovskite semiconductor laser diodes.* EcoMat, 2021. **3**(1).

121. Jin, M.F.F., et al., *The achievement of red upconversion lasing for highly stable perovskite nanocrystal glasses with the assistance of anion modulation.* Nano Research, 2021.

122. Zhao, Y., et al., *Synthesis of Colloidal Halide Perovskite Quantum Dots/Nanocrystals: Progresses and Advances.* Israel Journal of Chemistry, 2019. **59**(8): p. 649-660.

123. Chen, D. and X. Chen, *Luminescent perovskite quantum dots: synthesis, microstructures, optical properties and applications.* Journal of Materials Chemistry C, 2019. **7**(6): p. 1413-1446.

124. Xiao, M., et al., *Surface Ligands Stabilized Lead Halide Perovskite Quantum Dot Photocatalyst for Visible Light-Driven Hydrogen Generation.* Advanced Functional Materials, 2019. **29**(48): p. 1905683.

125. Li, S., et al., *Water-resistant perovskite nanodots enable robust two-photon lasing in aqueous environment.* Nat Commun, 2020. **11**(1): p. 1192.

126. Li, X., et al., *All Inorganic Halide Perovskites Nanosystem: Synthesis, Structural Features, Optical Properties and Optoelectronic Applications.* Small, 2017. **13**(9): p. 1603996.

127. Protesescu, L., et al., *Nanocrystals of Cesium Lead Halide Perovskites (CsPbX3, X = Cl, Br, and I): Novel Optoelectronic Materials Showing Bright Emission with Wide Color Gamut.* Nano Letters, 2015. **15**(6): p. 3692-3696.

128. Cao, X., et al., *A Review of the Role of Solvents in Formation of High-Quality Solution-Processed Perovskite Films.* ACS Applied Materials & Interfaces, 2019. **11**(8): p. 7639-7654.

129. Yang, Z., et al., *Research progress on large-area perovskite thin films and solar modules.* Journal of Materiomics, 2017. **3**(4): p. 231-244.

130. Zheng, K., et al., *Review of Incoherent Broadband Cavity-Enhanced Absorption Spectroscopy (IBBCEAS) for Gas Sensing.* Sensors (Basel, Switzerland), 2018. **18**(11): p. 3646.

131. Cao, H., *Lasing in random media.* Waves in Random Media, 2003. **13**(3): p. R1-R39.

132. Burin, A.L., H. Cao, and M.A. Ratner, *Understanding and control of random lasing.* Physica B: Condensed Matter, 2003. **338**(1): p. 212-214.

133. Redding, B., M.A. Choma, and H. Cao, *Speckle-free laser imaging using random laser illumination.* Nat Photonics, 2012. **6**: p. 355-359.

134. Chen, H., et al., *Quantum-size-tuned heterostructures enable efficient and stable inverted perovskite solar cells.* Nature Photonics, 2022. **16**(5): p. 352-358.

135. Zhang, D., et al., *Large-scale planar and spherical light-emitting diodes based on arrays of perovskite quantum wires.* Nature Photonics, 2022. **16**(4): p. 284-290.

136. Fang, Y., et al., *Highly narrowband perovskite single-crystal photodetectors enabled by surface-charge recombination.* Nature Photonics, 2015. **9**(10): p. 679-686.

137. Chen, Y., et al., *2D Ruddlesden–Popper Perovskites for Optoelectronics.* Advanced Materials, 2018. **30**(2): p. 1703487.

138. Wang, K., et al., *Two-dimensional halide perovskite quantum-well emitters: A critical review.* EcoMat, 2021. **3**(3).

139. Qin, Y., et al., *Coordination Engineering of Single-Crystal Precursor for Phase Control in Ruddlesden–Popper Perovskite Solar Cells.* Advanced Energy Materials, 2020. **10**(16).

140. Leng, K., et al., *Molecularly thin two-dimensional hybrid perovskites with tunable optoelectronic properties due to reversible surface relaxation.* Nat Mater, 2018. **17**(10): p. 908-914.

141. Stoumpos, C.C., et al., *Ruddlesden–Popper Hybrid Lead Iodide Perovskite 2D Homologous Semiconductors.* Chemistry of Materials, 2016. **28**(8): p. 2852-2867.

142. Abdelwahab, I., et al., *Highly Enhanced Third-Harmonic Generation in 2D Perovskites at Excitonic Resonances.* ACS Nano, 2018. **12**(1): p. 644-650.

143. Xu, C.-q., et al., *Optical third-harmonic generation in layered perovskite-type material (C10H21NH3)2PbI4.* Solid State Communications, 1991. **79**(3): p. 245-248.

144. Shimizu, M., J.-i. Fujisawa, and T. Ishihara, *Photoluminescence of the inorganic-organic layered semiconductor (C 6 H 5 C 2 H 4 N H 3) 2 Pb I 4: Observation of triexciton formation.* Physical Review B, 2006. **74**(15): p. 155206.

145. Kato, Y., et al., *Extremely large binding energy of biexcitons in an organic–inorganic quantum-well material (C4H9NH3)2PbBr4.* Solid State Communications, 2003. **128**(1): p. 15-18.

146. Abdelwahab, I., et al., *Giant and Tunable Optical Nonlinearity in Single-Crystalline 2D Perovskites due to Excitonic and Plasma Effects.* Adv Mater, 2019. **31**(29): p. e1902685.

147. Yu, J.H., et al., *High-resolution three-photon biomedical imaging using doped ZnS nanocrystals.* Nature Materials, 2013. **12**(4): p. 359-366.

148. Gao, W., et al., *Robust and Flexible Random Lasers Using Perovskite Quantum Dots Coated Nickel Foam for Speckle-Free Laser Imaging.* Small, 2021: p. e2103065.

149. Liu, W., et al., *Giant Two-Photon Absorption and Its Saturation in 2D Organic-Inorganic Perovskite.* Advanced Optical Materials, 2017. **5**(7).

150. Li, M., et al., *Enhanced Exciton and Photon Confinement in Ruddlesden-Popper Perovskite Microplatelets for Highly Stable Low-Threshold Polarized Lasing.* Adv Mater, 2018. **30**(23): p. e1707235.

151. Lei, L., et al., *Efficient Energy Funneling in Quasi-2D Perovskites: From Light Emission to Lasing.* Adv Mater, 2020. **32**(16): p. e1906571.

152. Li, M., et al., *Amplified Spontaneous Emission Based on 2D Ruddlesden-Popper Perovskites.* Advanced Functional Materials, 2018. **28**(17).

153. Li, Y., et al., *Exciton versus free carrier emission: Implications for photoluminescence efficiency and amplified spontaneous emission thresholds in quasi-2D and 3D perovskites.* Materials Today, 2021.

154. Wang, C., et al., *Low-Threshold Blue Quasi-2D Perovskite Laser through Domain Distribution Control.* Nano Lett, 2022.

155. Liang, Y., et al., *Lasing from Mechanically Exfoliated 2D Homologous Ruddlesden-Popper Perovskite Engineered by Inorganic Layer Thickness.* Adv Mater, 2019. **31**(39): p. e1903030.

156. Raghavan, C.M., et al., *Low-Threshold Lasing from 2D Homologous Organic-Inorganic Hybrid Ruddlesden-Popper Perovskite Single Crystals.* Nano Lett, 2018. **18**(5): p. 3221-3228.

157. Blood, P., *Quantum Confined Laser Devices: Optical gain and recombination in semiconductors*. 2015.

158. Wang, J., et al., *Room Temperature Coherently Coupled Exciton–Polaritons in Two-Dimensional Organic–Inorganic Perovskite.* ACS Nano, 2018. **12**(8): p. 8382-8389.

159. Blancon, J.C., et al., *Scaling law for excitons in 2D perovskite quantum wells.* Nature Communications, 2018. **9**(1): p. 2254.

160. Paritmongkol, W., et al., *Synthetic Variation and Structural Trends in Layered Two-Dimensional Alkylammonium Lead Halide Perovskites.* Chemistry of Materials, 2019. **31**(15): p. 5592-5607.

161. Smith, I.C., et al., *A layered hybrid perovskite solar-cell absorber with enhanced moisture stability.* Angew Chem Int Ed Engl, 2014. **53**(42): p. 11232-5.

162. Dyksik, M., et al., *Tuning the Excitonic Properties of the 2D (PEA)2(MA)n−1PbnI3n+1 Perovskite Family via Quantum Confinement.* The Journal of Physical Chemistry Letters, 2021. **12**(6): p. 1638-1643.

163. Ishihara, T., *Optical properties of PbI-based perovskite structures.* Journal of Luminescence, 1994. **60-61**: p. 269-274.

164. Cao, D.H., et al., *2D Homologous Perovskites as Light-Absorbing Materials for Solar Cell Applications.* Journal of the American Chemical Society, 2015. **137**(24): p. 7843-7850.

165. Sutherland, R.L., D.G. McLean, and S. Kirkpatrick, *Handbook of nonlinear optics*. 2nd ed. Optical engineering. 2003, New York: Marcel Dekker. xii, 971 p.

166. Yang, D., et al., *Amplified Spontaneous Emission from Organic-Inorganic Hybrid Lead Iodide Perovskite Single Crystals under Direct Multiphoton Excitation.* Advanced Optical Materials, 2016. **4**(7): p. 1053-1059.

167. Xu, Y., et al., *Two-Photon-Pumped Perovskite Semiconductor Nanocrystal Lasers.* J Am Chem Soc, 2016. **138**(11): p. 3761-8.

168. Zhang, S., et al., *Direct Observation of Degenerate Two-Photon Absorption and Its Saturation in WS2 and MoS2 Monolayer and Few-Layer Films.* ACS Nano, 2015. **9**(7): p. 7142-50.

169. Yu, S.F., *Lasing Characteristics of Single and Assembled Nanowires.* Semiconductor Nanostructures for Optoelectronic Devices, 2012: p. 251-278.

170. Chang, S., et al., *Stimulated emission and lasing in whispering-gallery modes of GaN microdisk cavities.* Applied Physics Letters, 1999. **75**(2): p. 166-168.

171. Yu, S.F., *Nonlinear dynamics of vertical-cavity surface-emitting lasers.* IEEE Journal of Quantum Electronics, 1999. **35**(3): p. 332-341.

172. Wei, Q., et al., *Recent Progress in Metal Halide Perovskite Micro- and Nanolasers.* Advanced Optical Materials, 2019. **7**(17): p. 1900080.

173. Benjamin, E., et al., *Temperature dependence of excitonic and biexcitonic decay rates in colloidal nanoplatelets by time-gated photon correlation.* The journal of physical chemistry letters, 2020. **11**(16): p. 6513-6518.

174. Jang, J. and J. Wolfe, *Auger recombination and biexcitons in Cu 2 O: A case for dark excitonic matter.* Physical Review B, 2006. **74**(4): p. 045211.

175. Uenoyama, T., *Excitonic enhancement of optical gain in quantum wells.* Physical Review B, 1995. **51**(15): p. 10228-10231.

176. Gong, X., et al., *Electron–phonon interaction in efficient perovskite blue emitters.* Nature Materials, 2018. **17**(6): p. 550-556.

177. Arakawa, Y. and A. Yariv, *Quantum well lasers--Gain, spectra, dynamics.* IEEE Journal of Quantum Electronics, 1986. **22**(9): p. 1887-1899.

178. Gauthron, K., et al., *Optical spectroscopy of two-dimensional layered (C6H5C2H4-NH3)(2)-PbI4 perovskite.* Optics Express, 2010. **18**(6): p. 5912-5919.

179. Wei, Y., Z. Cheng, and J. Lin, *An overview on enhancing the stability of lead halide perovskite quantum dots and their applications in phosphor-converted LEDs.* Chemical Society Reviews, 2019. **48**(1): p. 310-350.

180. Hu, Y., et al., *Bismuth incorporation stabilized α-CsPbI3 for fully inorganic perovskite solar cells.* ACS Energy letters, 2017. **2**(10): p. 2219-2227.

181. Brenner, P., et al., *Continuous wave amplified spontaneous emission in phase-stable lead halide perovskites.* Nature Communications, 2019. **10**(1): p. 988.

182. Sutton, R.J., et al., *Bandgap-Tunable Cesium Lead Halide Perovskites with High Thermal Stability for Efficient Solar Cells.* Advanced Energy Materials, 2016. **6**(8): p. 1502458.

183. Li, X., et al., *Amino-Mediated Anchoring Perovskite Quantum Dots for Stable and Low-Threshold Random Lasing.* Advanced Materials, 2017. **29**(36): p. 1701185.

184. Hu, Z., et al., *Enhanced Two-Photon-Pumped Emission from In Situ Synthesized Nonblinking CsPbBr3/SiO2 Nanocrystals with Excellent Stability.* Advanced Optical Materials, 2018. **6**(3): p. 1700997.

185. Zhang, H., et al., *Amplified spontaneous emission and random lasing using CsPbBr3 quantum dot glass through controlling crystallization.* Chemical Communications, 2020. **56**(19): p. 2853-2856.

186. Dutta, A., et al., *Phase-Stable CsPbI3 Nanocrystals: The Reaction Temperature Matters.* Angewandte Chemie International Edition, 2018. **57**(29): p. 9083-9087.

187. Mi, Y., et al., *Continuous-Wave Pumped Perovskite Lasers.* Advanced Optical Materials, 2019. **7**(17): p. 1900544.

188. Chen, J., et al., *Perovskite quantum dot lasers.* InfoMat, 2020. **2**(1): p. 170-183.

189. Liao, Q., X. Jin, and H. Fu, *Tunable Halide Perovskites for Miniaturized Solid-State Laser Applications.* Advanced Optical Materials, 2019. **7**(17): p. 1900099.

190. Gaio, M., M. Peruzzo, and R. Sapienza, *Tuning random lasing in photonic glasses.* Optics Letters, 2015. **40**(7): p. 1611-1614.

191. Jiang, Y., X. Wang, and A. Pan, *Properties of excitons and photogenerated charge carriers in metal halide perovskites.* Advanced Materials, 2019. **31**(47): p. 1806671.

192. Diroll, B.T., D.V. Talapin, and R.D. Schaller, *Violet-to-blue gain and lasing from colloidal CdS nanoplatelets: low-threshold stimulated emission despite low photoluminescence quantum yield.* Acs Photonics, 2017. **4**(3): p. 576-583.